

Spring 2005

On the role of high frequency waves in ocean altimetry

Douglas C. Vandemark
University of New Hampshire, Durham

Follow this and additional works at: <https://scholars.unh.edu/dissertation>

Recommended Citation

Vandemark, Douglas C., "On the role of high frequency waves in ocean altimetry" (2005). *Doctoral Dissertations*. 275.
<https://scholars.unh.edu/dissertation/275>

This Dissertation is brought to you for free and open access by the Student Scholarship at University of New Hampshire Scholars' Repository. It has been accepted for inclusion in Doctoral Dissertations by an authorized administrator of University of New Hampshire Scholars' Repository. For more information, please contact nicole.hentz@unh.edu.

**ON THE ROLE OF HIGH FREQUENCY WAVES IN
OCEAN ALTIMETRY**

BY

DOUGLAS C. VANDEMARK

B. Sc., Hope College, Holland, Michigan, 1986

M. Sc., University of Massachusetts, Amherst, 1988

DISSERTATION

Submitted to the University of New Hampshire
in partial fulfillment of
the requirements for the degree of

Doctor of Philosophy

in

Earth Sciences: Oceanography

May 2005

UMI Number: 3169093

INFORMATION TO USERS

The quality of this reproduction is dependent upon the quality of the copy submitted. Broken or indistinct print, colored or poor quality illustrations and photographs, print bleed-through, substandard margins, and improper alignment can adversely affect reproduction.

In the unlikely event that the author did not send a complete manuscript and there are missing pages, these will be noted. Also, if unauthorized copyright material had to be removed, a note will indicate the deletion.

UMI[®]

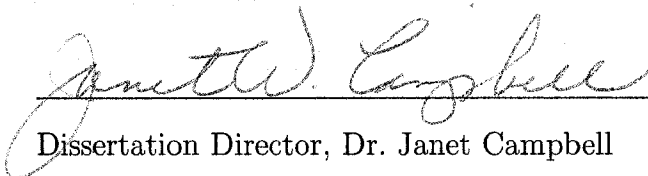
UMI Microform 3169093

Copyright 2005 by ProQuest Information and Learning Company.

All rights reserved. This microform edition is protected against unauthorized copying under Title 17, United States Code.

ProQuest Information and Learning Company
300 North Zeeb Road
P.O. Box 1346
Ann Arbor, MI 48106-1346

This dissertation has been examined and approved.

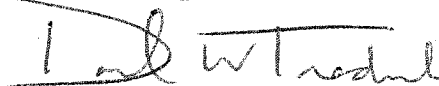


Dissertation Director, Dr. Janet Campbell

Research Professor of Earth Sciences

Institute for the Study of Earth, Oceans, and Space

University of New Hampshire



Dr. David W. Fredriksson

Research Assistant Professor of Ocean Engineering

University of New Hampshire



Dr. Lloyd C. Huff

Research Professor of Ocean Engineering

University of New Hampshire



Dr. Amala Mahadevan

Research Associate Professor

Department of Earth Sciences, Boston University

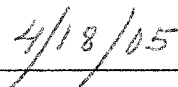


Dr. James B. Edson

Associate Professor

Departments of Marine Science and Physics

University of Connecticut



Date

Dedication

This work is dedicated to Dr. Timothy Crawford, a good friend and mentor, and a great scientist. You are remembered often and most fondly.

Acknowledgments

My thanks go out to many people in many places. First, to each committee member and especially to my advisor Dr. Janet Campbell for their time, efforts, and contributions. And again to Janet for her foresight and enthusiasm in bringing me up to this program.

Colleagues at NASA have been most supportive during my period at UNH and I especially thank John Gerlach, Tony Busalacchi (now at Univ. of Maryland), Franco Einaudi, Peter Hildebrand, and Eric Lindstrom for their advice and encouragement throughout.

The field measurements at the heart of this dissertation are the result of much work by a great team of people that includes but is not limited to: Ed Dumas, Jerry Crescenti, Jeff French, Dean Vickers, Larry Mahrt, Jielun Sun, Don Hines, and Carl Schirtzinger. Thanks as well to Will Drennan, Hans Graber and Mark Donelan who were instrumental in carrying out the SHOWEX program. Support for this research came from the Physical Oceanography program of NASA's Science Directorate, NOAA's Air Research Laboratory, and Office of Naval Research grant N0001497-F-0179.

Thanks as always to my close colleagues and sounding boards, Bertrand Chapron and Tony Elfouhaily, for their unflagging enthusiasm in all things to do with a radar and waves. And to coworkers at UNH including Joe Salisbury, Tim Moore and Hui Feng for their help in all things oceanographic, statistical, and Wildcat. And for keeping things shored up during what has been an interesting roller coaster ride.

Most of all, to my wife for the necessary patience and therapy sessions. Thank you Martha.

Table of Contents

Dedication	iii
Acknowledgments	iv
List of Tables	viii
List of Figures	viii
Abstract	xi
1 Introduction	1
1.1 Background	1
1.2 Statement of the problem	6
1.3 Long-term objectives	6
1.4 Hypotheses	6
1.5 Research approach	7
1.6 Expected significance	11
2 Ocean wave slope observations using radar and laser measurements	17
Abstract	17
2.1 Background	18
2.2 Measurements and processing	21
2.2.1 Micrometeorology	22
2.2.2 Laser altimeter system and surface slope statistics	23
2.2.3 Radar scatterometer	24

2.2.4	Radar-inferred slope estimates	25
2.3	Results	27
2.3.1	Wind dependence of long wave properties	28
2.3.2	Wind dependence of Ka-band σ^o	30
2.3.3	Long wave impacts	32
2.4	Discussion	34
2.5	Summary	41
3	Examining wind stress and wind waves in the presence of swell	54
	Abstract	54
3.1	Background	54
3.2	Methods	55
3.3	Results	56
3.4	Summary	59
4	Impact of high frequency waves in the ocean altimeter range bias	64
	Abstract	64
4.1	Background	65
4.2	Methods	67
4.3	Results	72
4.3.1	Long wave range biases	72
4.3.2	Ka-band EM bias	73
4.3.3	An example of spatial complexity	74
4.4	Discussion and conclusions	75
5	Summary	87

5.1	Significance and future work	92
6	Appendix	96
6.1	Copyright permission for Chapter 2	96
6.2	Listing of symbols and acronyms	97
	Bibliography	99

List of Tables

1.1	Key aircraft measurements used in the study	10
3.1	Average results for the low C_d cases	60
6.1	List of symbols	98

List of Figures

1-1	NOAA LongEZ (N3R) aircraft	13
1-2	Photo of radar	14
1-3	Sketch of laser altimeter surface measurement geometry	15
1-4	Map of the field experiment region	16
2-1	Aircraft and <i>in situ</i> wind intercomparisons	44
2-2	Aircraft calibration data over inland water	45
2-3	Study region	46
2-4	Range of observed wind speeds and wave heights	47
2-5	Surface slope statistics	48
2-6	Ka-band radar cross section measurements versus wind speed	49
2-7	Radar-derived mean square slope estimates	50
2-8	Inland and coastal measurement locations	50
2-9	Spatial dynamics in slope variance estimates	51
2-10	Spatial dynamics in short-scale slope variance estimates	51
2-11	Long wave impact on short-scale wave slopes	52
2-12	Slope spectra and probability densities	53
3-1	Measured drag coefficients versus wind speed	61
3-2	Drag measurements under rough and smooth flow	62
3-3	Drag measurements versus inverse wave age	63

4-1	Bias data for the entire experiment	81
4-2	Long wave biases versus wind speed	82
4-3	Long wave biases versus rms slope	82
4-4	Radar bias versus wind speed	83
4-5	Radar bias versus rms slope	83
4-6	Fetch-limited flight segment	84
4-7	WNL model	85
4-8	Ka-band and Ku-band	85
4-9	Tilt bias at Ka-band	86
4-10	Residual EM bias	86
5-1	Drag coefficient variation versus wave measurements	94
5-2	Ka-band backscatter versus friction velocity	95

ABSTRACT
ON THE ROLE OF HIGH FREQUENCY WAVES IN OCEAN
ALTIMETRY

by

Douglas C. Vandemark
University of New Hampshire, May, 2005

This work mines a coastal and open ocean air-sea interaction field experiment data set where the goals are to refine satellite retrieval of wind, wind stress, and sea level using a microwave radar altimeter. The data were collected from a low-flying aircraft using a sensor suite designed to measure the surface waves, radar backscatter, the atmospheric flow, and turbulent fluxes within the marine boundary layer. This uncommon ensemble provides the means to address several specific altimeter-related topics. First, we examine and document the impact that non wind-driven gravity wave variability, e.g. swell, has upon the commonly-invoked direct relationship between altimeter backscatter and near surface wind speed. The demonstrated impact is larger in magnitude and more direct than previously suggested. The study also isolates the wind-dependence of short-scale slope variance and suggests its magnitude is somewhat lower than shown elsewhere while a second-order dependence on long waves is also evident.

A second study assesses the hypothesis that wind-aligned swell interacts with the atmospheric boundary flow leading to a depressed level of turbulence. Cases of reduced drag coefficient at moderate wind speeds were in evidence within the data set, and buoy observations indicate that swell was present and a likely control during these events. Coincidentally, short-scale wave roughness was also depressed suggesting decreased wind stress. Attempts to confirm the theory failed, however, due to numerous limitations in the quantity and quality of the data in hand. A lesson learned is that decoupling atmospheric stability and wave impacts in field campaigns requires both a very large amount of data as well as vertical resolution of fluxes within the first 10-20 m of the surface.

A final study addresses an altimeter-specific issue where the accurate measurement of sea level at global and regional scale is at stake. The altimeter sea state bias is a required satellite altimeter range correction, $O(\text{cm})$, that changes with sea state dynamics in a manner that is not completely understood nor parameterized. Our high horizontal resolution aircraft data are particularly well-suited to address the processes dictating the bias. Combination of m- and cm-scale wave scattering versus the wave elevation are used to provide new insight into the complementary roles that these wave scales play in the phenomenon. First-ever measurements of the cross-skewness bias term are presented and convincing affirmation of the bias predicted using weakly nonlinear gravity wave theory is demonstrated.

These studies together help to define better the role that m-scale and longer gravity waves play in influencing altimeter backscatter, wind speed, and sea level measurements. As importantly, they provide a new and thorough documentation of slope statistics for intermediate-scale gravity waves that should be useful in a broad range of ocean remote sensing applications.

Chapter 1

Introduction

1.1 Background

Satellite altimetry is now recognized as a vital tool in global climate circulation studies, providing monthly to decadal monitoring of global dynamic topography and sea level, the zonal transport of heat via ocean circulation, and ocean surface wind and waves (Fu and Cazenave, 2001). Mission planning is such that global altimeter coverage extends from the mid 1980s into the foreseeable future. The altimeter remote sensing technique uses time-series analysis of a radar signal reflected off the wave-roughened ocean to estimate the sea surface significant wave height (H_s), near-surface wind speed (U), and sea level. These basic altimeter inversion products are continually being improved upon, the primary goal being to reduce sea level estimate uncertainties below the present-day 3 cm limit. Improving on this limit will increase the confidence in satellite derivation of the rate of sea level rise, currently estimated to be between 2 and 3 mm/year.

It is recognized that remaining measurement uncertainties are due in large part to the unresolved impacts of gravity wave variability upon the radar return signal. Each altimeter measurement is derived from a nadir-viewing ocean footprint of about 2 km diameter. The wavefield dynamics within this footprint, for example the directional wind sea and swell spectra, the amount of small wind-coupled wavelets, the extent of wave breaking, are all largely unresolved but nevertheless do affect the desired geophysical inversions. It is largely through empirical field studies, where wind and waves are directly measured, that such within-footprint effects are detected and understood.

This work uses data from one such field study to address uncertainty in the estimation and interpretation of two specific altimeter geophysical derivatives. First is the microwave

altimeter's normalized radar cross section, σ^o , and its subsequent conversion to wave and near surface wind speed information. σ^o is defined as the surface area-normalized reflectivity of a target, in this case the sea. Typically, σ^o can vary as a function of the viewing angle, radiation frequency, target geometry and dielectric properties. The unresolved questions regarding σ^o and its link to wind speed and waves all center on knowing the relative impacts of different wave scales on the backscatter. More specifically, to what extent do long waves influence σ^o data?

Short cm-scale gravity capillary waves are generated by near-surface winds and subsequently act as diffusers of the vertically-directed radar altimeter signal. The first-order observation is well documented - there exists a close inverse linkage between near-surface ocean winds and the radar backscatter. Empirically, this relationship is developed as $\sigma^o \propto \frac{1}{f(U)}$ (Witter and Chelton, 1991) or some variant (see Chelton et al., 2001). Physically, this relationship was modeled by Barrick (1968) using an intuitive quasi-specular scattering approach

$$\sigma^o(\theta) = \frac{|R(f, \theta)|^2}{mss} \sec^4 \theta e^{-\frac{\tan^2 \theta}{mss}} \quad (1.1)$$

where f is the radiation frequency, the incidence angle θ is 0° for the altimeter and mss is the sea surface slope variance, a parameter typically dominated by steep and numerous gravity capillary wavelets. $|R(\theta, f)|^2$ represents the seawater Fresnel reflectivity, typically a weak function of sea temperature and salinity.

It is second-order wave field information carried within σ^o that we propose to examine. A main goal will be to establish the extent of wave ($\lambda = 1$ to 50 m) control upon σ^o and subsequent wind and wind stress inversions. The concept of integration plays a central role in describing both the waves and their remote sensing. First, the random sea is well-modeled as a continuous spectrum of waves where the wave height directional spectrum is given as $S(k, \phi)$, with k being the wavenumber and ϕ the horizontal propagation direction. It is straightforward to show that the wave slope variance (mss) can be written as $mss = \int \int k^2 S(k, \phi) dk d\phi$. Moreover, invoking linear wave theory and the principle of superposition, one can propose the additive formulation (omnidirectional):

$$mss(U, H_s, \Omega) = \int_0^{k_l} S(k) dk + \int_{k_l}^{k_h} S(k) dk = mss_l(U, H_s, \Omega) + mss_h(U, \Omega) \quad (1.2)$$

Here the surface is partitioned into two wave regimes - one a faster moving low wavenumber gravity wave regime and the other a slow moving high wavenumber gravity-capillary wave regime (Longuet-Higgins and Stewart, 1960). In the present case we will impose k_l to be $\frac{2\pi}{20}(\text{rad m}^{-1})$ and k_h to be $\frac{2\pi}{0.01}(\text{rad m}^{-1})$. Most fundamentally, mss_l provides an integrated measure of steepness for the long, energy-containing gravity wave scales, waves not necessarily strongly coupled to the local wind field. mss_h on the other hand responds quickly to changes in the local wind stress. Wave height H_s , inverse wave age Ω , and wind (U) dependencies are denoted in eq. 1.2 to reflect the characteristic parameterizations.

Integration from the altimeter remote sensing perspective enters when one recognizes that both low and high wavenumber regimes are integrated in σ° as seen in eq. 1.1 and 1.2. In effect, one anticipates that σ° is sensitive to both long and short wave scales. This two-scale construct will be central in this thesis. Do long wave dynamics negatively impact the remote sensing of wind? When and to what extent? Does the altimeter's integrated view of the slope spectrum provide a unique perspective on air-sea momentum flux, one unobtainable from a dedicated short wave sensor such as the microwave scatterometer?

Many theoretical studies have addressed the relationship between σ° , ocean surface winds and the surface wave field (Barrick, 1974; Jackson et al., 1992; Marchand and Brown, 1998; Anderson et al., 2002). Key acknowledged results are that the short cm-scale wave roughness (i.e. mss_h) dictates much of the mss and σ° signatures, but also that the long waves enter as a second-order factor with uncertain and varied parameterization. Predictive modeling requires an electromagnetic scattering model and a wind-dependent sea surface definition. Refinements of scattering models (Jackson et al., 1992; Plant, 2002; Elfouhaily et al., 2001b) and of wave measurements and modeling (Elfouhaily et al., 1997), especially in the high frequency range (Hwang et al., 1996; Hara et al., 1998), are ongoing. Still, even though the altimeter is a relatively simple member of the active remote sensing family, the physical interpretation of satellite altimeter σ° remains an active area of research. Conflicting findings are not unusual (Anderson et al., 2002; Hwang et al., 2002). Most critically, it is well known that the main source of uncertainty amongst these efforts is the inability

to measure and then model the moving sea surface structure in four dimensions (x,y,z,t) at the necessary level of detail. Such detail includes measurement of the overlying turbulent wind field.

This is the entry point for much of the following work. This thesis presents new observations developed around the measurement of eq. 1.2 where we resolve both mss (via σ^o) and $mssl$. Such measurements are well-suited to address a fundamental question within altimetry : To what extent is the σ^o vs. wind speed relationship sensitive to long wave variability associated with a non-wind driven wave field? While recent empirical satellite studies have identified a measurable altimeter wind speed inversion error using other long wave proxies (Glazman and Greysukh, 1993; Gourrion et al., 2002b), we present a study documenting the effect through examination of the most logical physical control, $mssl$. This is the main goal of the first study, presented in Chapter 2, where the wind speed dependence of mss (i.e. σ^o) and $mssl$ are detailed in both coastal and open ocean regimes.

A second separate, but related, study aims to examine the physical partitioning of wave-induced wind stress across the low- and high-wavenumber measurements provided under eq. 1.2. In essence, we wish to study the variability of the surface drag coefficient C_d with changes in the surface roughness:

$$C_d = \frac{u_*^2}{U^2} = F(mssl, mssh) \quad (1.3)$$

Here u_* represents the friction velocity, or turbulent roughness velocity scale for the atmospheric flow. Recall that the wind stress $\tau = \rho u_*^2$, with ρ being the air density. A sea state dependent parameterization for the drag coefficient term has been under study for decades and remains unresolved. The present work is unlikely to reduce the uncertainty. Rather, one proposed approach is to bring the two-scale surface and altimeter perspectives to bear on the remote sensing of air-sea momentum flux. This may differ from that of a satellite scatterometer-derived pseudostress where the wind estimate is thought to be solely a reflection of the short gravity capillary wavelets. One question to address using these aircraft data: What is the response of both short and long wave scales to changes in the measured drag? The interfacial form drag, turbulent flow associated with vertical roughness elements, is predominately carried by long waves (Donelan, 1990). Do the drag coefficient

and long-wave slope observations covary? When does a functional relationship between mss_h and C_d seem more appropriate? High fidelity eddy correlation fluxes (i.e. u^*) from the aircraft are the crucial measurement used, and a variable typically missing in air-sea field investigations.

Another possible direction for this component of the study will be to examine the role that swell plays in controlling the drag coefficient. Several recent studies (Larsen et al., 2004; Smedman et al., 2003b; Rutgersson et al., 2001; Kudryavtsev and Makin, 2004; Drennan et al., 1999) present arguments and data suggesting that fast-running swell fields represent a primary perturbation source in the air-sea coupling equation. Chapters 3 and 5 address results obtained pertaining to drag coefficient variability.

Finally, while the issues above pertain to wind-dependent σ^o measurements, the most critical altimeter derivative is the range measurement used to derive mean sea level. The electromagnetic range bias is another “within-footprint” altimeter phenomenon associated with the variability of surface waves (see Chelton et al., 2001). In this case, the issue is the observed fact that the radar signal return is asymmetric in time as it passes from the wave crest to the trough. The scattering is more diffuse at the crest than the trough. This slight asymmetry is written as

$$\epsilon = \frac{\langle \eta \sigma^o \rangle}{\langle \eta \rangle \langle \sigma^o \rangle} \quad (1.4)$$

with η being the surface wave elevation. The result is a bias of mean sea level towards the wave troughs, and this bias varies with the sea state dynamics in a manner that has yet to be fully resolved. Operationally, the EM bias impact on an altimeter’s range measurement requires an $O(10 \text{ cm})$ correction, and this adjustment carries an $O(1 \% H_s)$ uncertainty (Chelton et al., 2001). The final study in this thesis again uses the two-length-scale concept as the basis for a physical investigation of this “sea-state bias” correction and the remaining sources of uncertainty. To date, no one has quantitatively documented the physically-predicted (Longuet-Higgins, 1963) cross-skewness statistic between long gravity wave elevation and slope, nor done this in concert with the radar scattering observations that enfold this cross-skewness into the total sea state bias model for the nonlinear sea surface. This crucial term is defined as

$$\lambda_{12} = \frac{\langle \eta \eta_x^2 \rangle}{\langle \eta^2 \rangle^{1/2} \langle \eta_x^2 \rangle} \quad (1.5)$$

where η_x is the along-wave surface slope. The m-scale horizontal resolution aircraft data obtained on both long and short wave properties should permit evaluation of λ_{12} , and in the process provide a much stronger observational constraint upon modeling of this phenomenon.

1.2 Statement of the problem

Uncertainties in surface wind wave and electromagnetic scattering theories remain large enough to cloud the geophysical interpretation of satellite radar altimeter measurements. Several fundamental questions linger regarding the physical processes that can be detected, measured, and corrected for using spaceborne altimeter products. Resolution of these questions could lead to improved sea-level estimates in future altimeter missions and to enhanced use of altimeter ocean wind speed data within coupled air-sea climate models.

1.3 Long-term objectives

The overall research goal is to clarify the interpretation and use of satellite altimeter measurements in climate research. This includes both the measurement of sea level used in global ocean circulation research and of the radar backscatter used to provide sea surface wind stress information. To achieve this goal we need to extend what is known about m- to cm-scale ocean wavelets, including their wave-wave interactions, their variation with wind forcing, and how these waves impact altimeter sea echoes.

1.4 Hypotheses

This thesis revolves around field measurements of near-surface wind, wave, and radar properties collected using an aircraft in a manner specifically dedicated to the study of ocean altimeter backscatter. Three separate studies are developed based on the following hypothe-

ses.

- Observed second-order long wave effects upon observed altimeter σ^o data can be directly explained and quantified using long wave slope variance measurements in accord with prediction of quasi-specular microwave scattering theory.
- Sea-state dependence in the air-sea drag coefficient can be seen in the case of wind-aligned swell where substantial turbulence depression depends on both the swell direction versus wind and the swell height with respect to the sea.
- Wave properties controlling the altimeter sea level bias include the cross-skewness between wave elevation and slope (both derived over gravity wave scales much greater than 1 m) as well as the hydrodynamic modulation of short cm-scale gravity-capillary wavelets riding atop these faster moving long waves. The magnitude of both factors is non-negligible under most wind and wave conditions.

These ideas stem from, and in most cases are predicted by, existing theory on wind wave interaction and radar remote sensing. However, their proof in a quantitative or qualitative manner remains incomplete. More detailed motivation and background surrounding and supporting each idea is provided in coming chapters.

1.5 Research approach

The chosen research approach is primarily observational. Hypotheses are addressed using a common experimental data set collected by a recently developed airborne platform for wind and wave measurement. Coincident laser altimeter, microwave (36 GHz) radar, turbulent flux, and wind measurements were made at an altitude of 10-15 m above the ocean using an aircraft traveling over the sea at 50 m/s. The field experiments were conducted over the coastal and open-ocean North Atlantic from 1997-1999 as part of Navy and NASA research programs.

Two features make this data set a powerful and appropriate tool for these studies. First, the measurement sensor suite and its configuration are, by design, well suited for addressing altimetry issues. Second, the data set sampling of varied wind and wave conditions is large

enough to ascribe statistical significance to the derived results at a level that is usually not possible in air-sea interaction studies. This feature was enhanced by the aircraft's spatial sampling versatility. For example, we were able to sample the wave diversity inherent to inland, coastal and open ocean regimes within a period of minutes. Such a capability is obviously absent in a fixed platform data set and increased the dynamic range of geophysical variability within the data set.

Key measurements, common to the thesis as a whole, are listed in Table 1. Detail on the specific data analysis and application of these measurements to the listed hypotheses are developed in the following sections. Several recent papers present much of the relevant measurement description and analysis (Vandemark et al., 2001; Sun et al., 2001; Vandemark et al., 1999; Sun et al., 2003), so only the most salient features are reviewed here.

The platform for data collection was the NOAA LongEZ research aircraft operated by NOAA's Air Research Laboratory. This aircraft was outfitted with an integrated data system that collected and time tagged all aircraft sensor data simultaneously. The complement of instruments aboard the small craft was extensive as seen in Fig. 1-1 (see also French et al., 2000). What is most critical to this work is the wind speed measurement as derived from a multi-port pressure sphere, termed the BAT probe, that was located out front of the fuselage. The rear propeller design and clean airframe were key to high-fidelity wind velocity measurements in horizontal and vertical directions. Another critical component was the distributed four antenna GPS network that was used to provide requisite aircraft motion data at the necessary resolution in pitch, roll, vertical acceleration and time. The aircraft's extraordinary operating envelope was the other defining feature for this study. Flight altitude was typically 12 to 15 m above the ocean, much lower than any air-sea interaction craft has routinely operated in the past. This sampling height provided the opportunity to collect eddy correlation momentum flux measurements within the so-called constant stress boundary layer.

As noted, nadir-view σ^o measurement is central to the key study equations (eqs. 1.1 and 1.2). A Ka-band ($f = 36$ GHz or $\lambda=0.083$ m) radar was custom built and integrated into the aircraft to provide these data. A simple continuous-wave scatterometer design was chosen. A photo of the sensor is shown in Fig. 1-2. This system measures the intensity of reflected power and combines this measurement with the known range to the surface and

known sensor characteristics to derive σ^o at Ka-band at a 50 Hz rate along the aircraft track. Detail is found in Vandemark et al. (2001) and Vandemark et al. (2004c). The choice of 36 GHz was driven primarily by the requisite antenna size for this small aircraft. This frequency is not used in satellites to date, and field data at 36 GHz are somewhat limited. In the end, the choice should permit us to document results at 36 GHz and revisit some past Ka-band observations that are in conflict with physical modeling (Masuko et al., 1986; Walsh et al., 1998). At the same time, our Ka-band results should be sufficiently similar to data at 14 GHz such that findings will translate directly to satellite data interpretation.

Three commercial cm-precision laser altimeters were operated synchronously to provide range, sea surface elevation, and sea surface slope measurements. The configuration is seen in Fig. 1-3. Much work has gone into the analysis of these data to provide a final product that is most simply considered as a translating three-element wave staff. Both the sea surface elevation and slope statistics enter critically into all aspects of this study. Most central is the computation of the slope variance, mss_l , seen in eq. 1.2. Several recent studies document these measurements (Vandemark et al., 2001; Sun et al., 2001, 2003; Hall et al., 2000; Vandemark et al., 1999).

The field experiments providing the data for this study come from the Office of Naval Research's SHOaling Wave Experiment (SHOWEX) (French et al., 2000; Crescenti et al., 1999) and NASA's Wave Profile Experiment (WAPLEX). In total, the aircraft flew on 36 separate days to collect the data used here. The map of Fig. 1-4 provides a sense of the spatial sampling, where each point on the map represents the center location of a 5 km along-track segment for measurements collected during low-altitude flight operations. Ancillary data were also collected to support these efforts, often by specialized buoys deployed in the region. The LongEZ itself provides air and sea temperature measurements, along with dew point, all needed to estimate the boundary layer stability as needed in some of the work to follow. Wave buoy data will also be used as ground truth for the laser measurements and as supporting data that provide a measurement of the directional wave spectrum. Much of the data in 1998 was gathered directly over NDBC directional wave buoy number 44014 as shown on Fig. 1-4. In 1999, there are numerous flights over the wave and meteorological ASIS buoys operated by the University of Miami.

The next three chapters address the hypotheses proposed above. Each study draws

Table 1.1: Key aircraft measurements used in the study

PARAMETER	SYMBOL	ALONG- TRACK SAMPLING RATE	DATA SOURCE	ANALYSIS SOURCE	HORIZ. MEASURE. RESOL.
Wind velocity	u, v, w	1 /m	BAT probe+GPS	NOAA	0.1 x 1 m
Friction velocity	u^*	1-5 /km	u, v, w	this study	0.1 m x 1-5 km
Ka-band radar cross section	σ^o	1 /m	NASA Ka-band scatt.	this study	0.8 m ²
Sea surface height	ssh or (η)	1 /m	Riegl laser altim.+GPS	this study	0.03 x 1 m
Wave slope vector	$S = (s, \theta)$	1 /m	$\eta(x)$	this study	1 m ²

out different salient features from the data set where the coincident radar, laser altimeter and wind measurements provide a combination of observations sufficient for examining the noted hypotheses in a novel way. Several common threads tie these efforts together. Firstly, all work is directed toward improved understanding of the reflection of vertically-directed microwave radiation from the sea surface. Specifically, the goal is to provide new quantitative evidence that helps to clarify the physical interpretation of this type of backscatter. Secondly, a large part of the design for the aircraft sensors and field experiments is explicitly aimed at addressing pertinent satellite altimeter geophysical inversion issues such as those to be discussed in the following chapters. Thirdly, the key observational theme shared by all efforts is the insight gained by measuring the nadir view radar backscatter in concert with the long wave slope variance.

1.6 Expected significance

The following results were anticipated when developing this research plan.

Study 1 - Measurement and analysis following eq. 1.2 should provide the quantitative documentation needed to more strongly cement the physical model relating altimeter backscatter to both local wind and long wave impacts. The new Ka-band radar data also suggest an apparent calibration-based error exists in the literature; the present data provide a more physically consistent result within the context of wind and wave remote sensing.

Study 2 - One of few studies to look at the drag coefficient variability associated with the long wave slope variance and with the radar-derived σ^o . Results may impact how the drag coefficient is parameterized and used in models for wave generation and ocean circulation. Results should also help clarify the role that the satellite altimeter can play in refining how the suite of ocean wind remote sensors (i.e. scatterometer, radiometer, altimeter) are used to infer wind stress information.

Study 3 - Observations should improve the physical model for the altimeter sea state bias and help to motivate a revision of the operational sea level correction algorithm.

The final chapter in this effort provides discussion summarizing what was actually accomplished and how the results of chapters 2-4 serve to move research forward in the arena

of ocean remote sensing using radar altimeters.

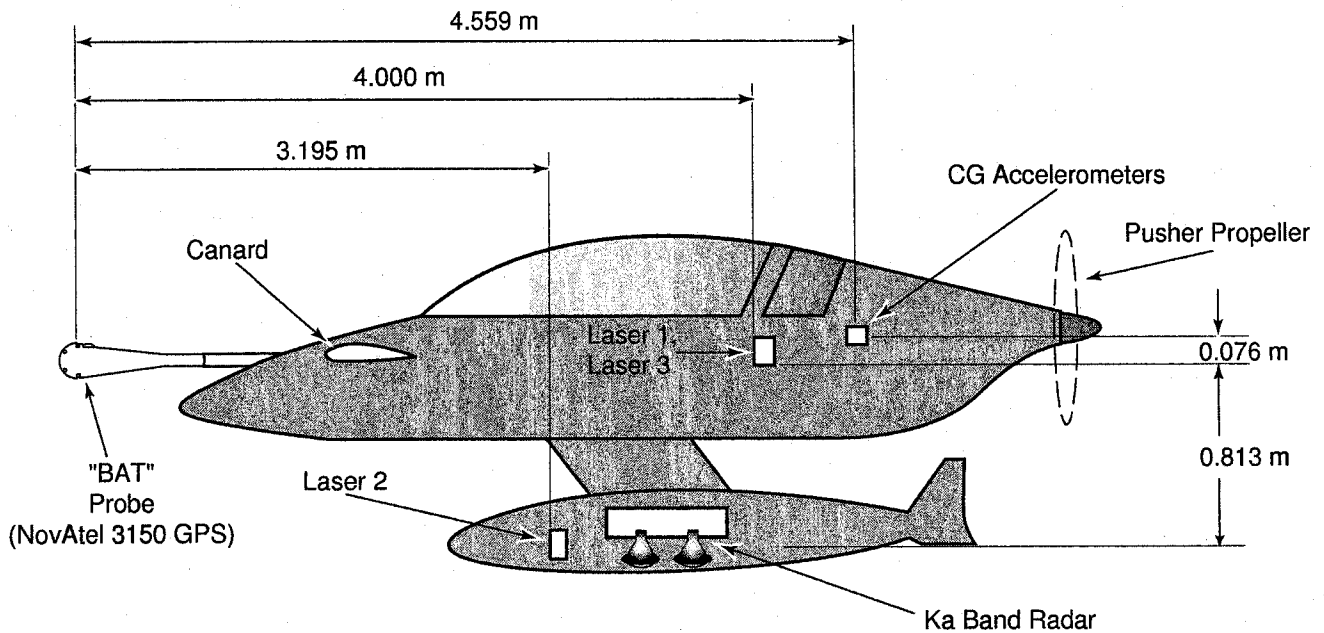


Figure 1-1: NOAA Long-EZ (N3R) aircraft including turbulence probe on the nose and measurement pod below the airframe. Note the rear-mounted propellor.



Figure 1-2: Custom built nadir viewing Ka-band scatterometer used in N3R data collection.

(a) Side view of NOAA LongEZ



(b) Plan view of three laser altimeters

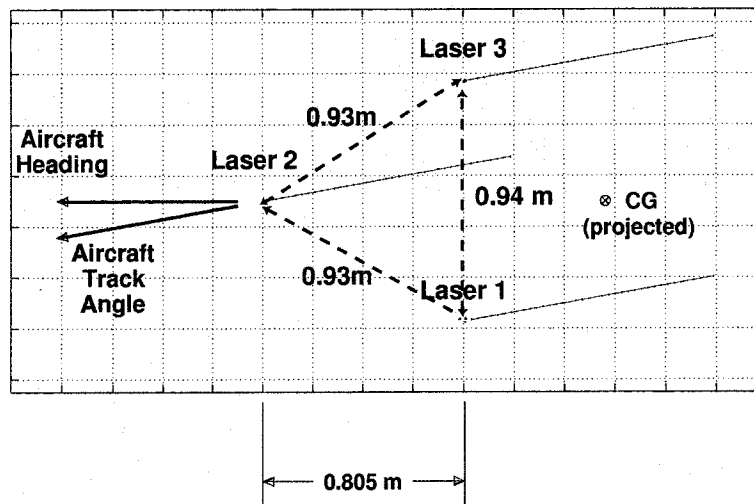


Figure 1-3: Sketch of laser altimeter surface measurement geometry

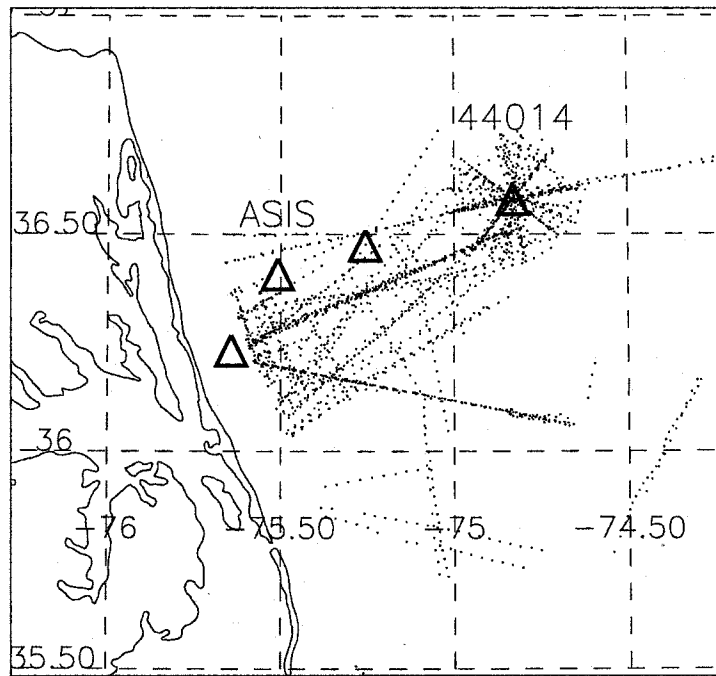


Figure 1-4: Map of LongEZ measurement points off of the coast of North Carolina as collected from 1997-99. The location of directional wave measurement buoys present during some portion of the data collection are also shown.

Chapter 2

Ocean wave slope observations using radar and laser measurements

The following chapter has been published in the Journal of Physical Oceanography, see Vandemark et al. (2004). © Copyright 2004 American Meteorological Society (AMS). Permission to use figures, tables, and brief excerpts from this work in scientific and educational works is hereby granted provided that the source is acknowledged. Any use of material in this work that is determined to be "fair use" under Section 107 or that satisfies the conditions specified in Section 108 of the U.S. Copyright Law (17 USC, as revised by P.L. 94-553) does not require the Society's permission. Republication, systematic reproduction, posting in electronic form on servers, or other uses of this material, except as exempted by the above statements, requires written permission or license from the AMS. Additional details are provided in the AMS Copyright Policies, available from the AMS at 617-227-2425 or amspubs@ametsoc.org.

Abstract: Combination of laser and radar aboard an aircraft is used to directly measure long wave surface tilting simultaneous with nadir-viewing microwave backscatter from the sea surface. The presented data set is extensive, encompassing varied wind conditions over coastal and open ocean wave regimes. Laser-derived slope statistics and Ka-band (36 GHz) radar backscatter are detailed separately to document their respective variations versus near-surface wind speed. The slope statistics, measured for $\lambda > 1-2$ m, show good agreement with Cox and Munk's oil-slickened sea measurements. A notable exception is elevated distribution peakedness and an observed wind dependence in this likely proxy

for nonlinear wave-wave interactions. Aircraft Ka-band radar data nearly mimic Ku-band satellite altimeter observations in their mean wind dependence. The present calibrated radar data, along with relevant observational and theoretical studies, suggest a large (-5 dB) bias in previous Ka-band results. Next, wave-diverse inland, coastal, and open ocean observations are contrasted to show wind-independent long wave slope variance changes of a factor 2-3, always increasing as one heads to sea. Combined long wave and radar data demonstrate that this long wave tilt field variability is largely responsible for radar backscatter variations observed at a given wind speed, particularly at wind speeds below $5\text{-}7\text{ ms}^{-1}$. Results are consistent with, and provide quantitative support for recent satellite altimeter studies eliciting signatures of long wave impacts resident in the radar backscatter. Under a quasi-optical scattering assumption, the results illustrate of long-wave control on the variance of the total mean square slope parameter due to changes in the directional long wave spectrum, with high wavenumbers being relatively unaffected in a mean sense. However, further analysis suggests that for winds above 7 ms^{-1} the high wavenumber subrange also varies with change in the longer wave field slope and/or energy; the short wave roughness being measurably greater for smoother seas.

2.1 Background

The mean relationship between sea wave slope statistics and near-surface ocean wind speed has long been established (Cox and Munk, 1956), as has the tie between these optically-derived wave slope variance measurements and the ocean radar backscatter measured by a microwave altimeter (Barrick, 1968a; Jackson et al., 1992). But it has also been supposed for decades that factors such as wind gustiness, currents, fetch, and long wave dynamics will serve to significantly vary any such mean wind-wave correlation and its inversion using radio probing techniques (Barrick, 1974). Understanding, detecting, and monitoring these dynamics using today's complement of spaceborne ocean remote sensors is a challenge requiring a blend of field measurements, modeling, and satellite data interpretation. Opportunities presented include the goal to improve wind stress estimation from space by enfolding the noted second order effects in air-sea coupling formulations at global to local scales.

Short waves with $\lambda < 10\text{-}20$ cm are considered critical to microwave remote sensing of ocean winds. This is because these wavelets respond quickly and dynamically to increases in the local wind, and because the transmit wavelength of such sensors makes the radio probing of these waves possible. But long wave tilting of the short waves is also fundamental perturbation carried in the increasingly common two- or three-scale models for surface wave interaction and ocean wave remote sensing alike (e.g. Bass et al., 1968; Barrick, 1968b; Valenzuela, 1978; Longuet-Higgins, 1982; Gotwols and Thompson, 1994; Liu et al., 1997; Chapron et al., 2000; Plant, 2002). Such models impose a separation between long and short waves, permitting separate characterization of their wind-dependent statistics, forcing and dissipation as well as subsequent recombination to address possible interactions between the scales. Separation is also imposed because a substantial fraction of the long wave field is often due to swell and sea generated by distant or turning winds, waves that are uncoupled and misaligned as far as the local wind is concerned. Such dynamics can impact how well a remote sensor inverts wind stress and short wave information.

The following work provides new field measurements related to long and short wave slopes on the sea - both their covariance with respect to local wind forcing and with longer wave dynamics divorced from the local wind. Specific goals are to document the long wave field using directly-measured slope statistics, and to then to illustrate and quantify the effect that this tilting field has upon an altimeter's nadir-view normalized radar backscatter cross section, $\sigma^o(\theta = 0^\circ)$, and its subsequent interpretation.

When ocean altimetry is considered, aside from wind dependency, at least three factors arise in the interpretation of σ^o : absolute radar calibration, long wave impacts, and short-wave diffraction. These factors are central to σ^o use in wind speed and wave spectral estimations, and in attempts to gain new geophysical insight using altimeter observations at differing transmit frequencies (Jackson et al., 1992; Elfouhaily et al., 1998). This paper concentrates mainly on the first two issues and A first-order specular point scattering theory (Barrick, 1968a) is considered adequate for the examination of the first two factors:

$$mss' = \frac{|R(0^\circ)|^2}{\sigma^o(0^\circ)} \quad (2.1)$$

where the numerator holds the frequency-dependent surface Fresnel reflectivity factor and mss' is a radar-derived estimate of the surface wave slope variance, mss . One implicit assumption is that there is no *a priori* need to invoke an effective Fresnel coefficient in

the derivation (cf. Chapron et al., 2000). This and further assumptions behind eq. 2.1 are discussed in section 2.2.4. This paper concentrates mainly on the first two issues above while the issues of diffraction and precise inference of high wavenumber spectral information can be reviewed elsewhere (e.g. Jackson et al., 1992; Chapron et al., 1996; Plant, 2002).

Absolute σ^o levels at the nadir view angle are addressed using a Ka-band (36 GHz) radar, in part to revisit past nadir-view Ka-band data (Masuko et al., 1986). Those data represent the only such data available at Ka-band and indicate an unexpectedly large 5-6 dB difference with respect to nadir-view X- and Ku-band observations. Recent results using an indirect absolute radar cross section determination method (Walsh et al., 1998) suggest there may be a calibration error and this possibility will be assessed. Present results should also resemble that obtained using a satellite radar altimeter operating at 36 GHz. As such, they provide preliminary design data for proposed Ka-band altimeters such as AltiKa, a new mission being considered by the European Space Agency.

Regarding long wave impacts, typically this gravity wave ($\lambda > 30$ cm,) contribution to mss is assumed to be small $O(20-30\%)$ and highly correlated with wind speed, thus deviation from a nominal wind-dependent mss due to a long waves is often considered unlikely or negligible. Some recent work has shown the effect should not be neglected (e.g. Hwang and Shemdin, 1988; Hesany et al., 2000). Other recent satellite altimeter work (Glazman and Greysukh, 1993; Hwang et al., 1998; Gommenginger et al., 2002; Gourrion et al., 2002a,b) use proxies such as significant wave height, H_s , to demonstrate measureable long wave variability impacts upon σ^o . Still, observed ambiguities indicate that physical explanation and quantification remains somewhat uncertain (Gourrion et al., 2002a). For example, is σ^o variation strictly geometrically-controlled, i.e. due to long wave tilt field changes, or is it due to perturbation of the cm-scale waves by long-wave hydrodynamics? This study looks at such questions by considering radar σ^o data collected in concert with direct measurement of slope statistics for long-to-intermediate scale gravity waves $O(100-1$ m). These longer wave observations are derived using a three laser slope measurement system, providing a quantitative check of the oft-cited oil slickened surface slope estimates reported by Cox and Munk (1956). As such, the laser results also serve the more general purpose of documenting long-wave slope statistics relevant to satellite sensors working in frequencies from L-band to the visible.

The platform used to acquire the coincident wave and wind measurements for this study was NOAA's LongEZ research aircraft. Data were collected over a two year period as part of the Office of Naval Research SHOaling Waves EXperiment (SHOWEX) and NASA's Wave Profile Experiment (WAPEX). Following is an overview of the data collection, measurement techniques, and their validation. Laser-derived slope and Ka-band radar backscatter data are then presented and discussed in context of past observations. Analysis combining these tools helps to clarify, in quantitative terms, the impact of long waves on the detection of short waves, and hence wind, using remote sensors in regions such as the coastal zone.

2.2 Measurements and processing

Measurements to be discussed were collected over either the western Atlantic or the inland waters of the Currituck Sound, always within 120 km of Duck NC. All flights occurred between 1997 and 1999, with most data collected in the month of November. Data come from 36 separate flights of the NOAA LongEZ covering a variety of wind and wave conditions. Aircraft flight patterns over the region varied to accomodate several complementary investigations (Sun et al., 2001; Vandemark et al., 2001; Mahrt et al., 2001; French et al., 2000). The composite coverage provides a data set containing extensive sampling over open-ocean, coastal and inland water. For all data presented herein the aircraft flew at an average altitude of 15 m above the surface. This is a unique vantage point that permits high resolution and high fidelity sensing of the sea surface and air above, much as for a fixed experimental platform. Efforts mentioned above describe the aircraft measurement systems and data processing used in this study, thus only details critical to this work are discussed below. All data have undergone extensive quality checks noted in the studies above. One focus here is on the wind-dependence of wave slope statistics and radar backscatter. Typical time and spatial averaging windows for ocean wind measurement are 8-10 min. and 5-15 km, respectively. A 5 km along track aircraft extent is chosen for the averaging length scale in this study to retain spatial wind and wave dynamics inherent to the region (Sun et al., 2001).

2.2.1 Micrometeorology

Five-km wind velocity and friction velocity (u_*) estimates are produced using the processed LongEZ (French et al., 2000) wind data and eddy covariance flux estimations (Sun et al., 2001). The main atmospheric derivative for this study is neutral-stability wind speed at 10 m above the surface, U_{10N} . Values are obtained from measured winds, U_m , at altitude z using:

$$U_n(z) = U_m(z) + \frac{u_*\psi(z/L)}{\kappa} \quad (2.2)$$

and:

$$U_{10n} = U_n(z) + \frac{u_*\log(\frac{10}{z})}{\kappa} \quad (2.3)$$

where κ is von Karman's constant; L, the Monin-Obuhkov stability length, is computed using a bulk formulation based on the Richardson's number, Ri (Donelan, 1974); and the stratification correction, ψ , follows Paulson (1970) and Dyer (1974) for unstable and stable cases respectively. The LongEZ also measures the humidity, sea and air temperature scalars needed to derive Ri . Formulation of L in terms of a bulk Ri estimate is done to avoid noise frequently introduced by the cubic u_* term needed when using direct eddy correlation estimates to derive L. While U_{10n} estimates obtained here may differ slightly from alternate methods, intercomparisons show variance to be less than 0.3 m s^{-1} , a level of accuracy that is adequate for this study.

Several *in situ* meteorological platforms were overflown by the aircraft during these experiments. Direct comparison of aircraft winds to those from the National Data Buoy Center (NDBC) buoy 44014, located 80 km off shore, are shown in Fig. 2-1. Data shown represent measurements collected within 10 km and 30 minutes of each other. Aircraft samples are derived from 5 km segments along the flight track, while the buoy wind is the average over an eight minute time window. U_{10n} values shown for both the aircraft and NDBC buoy are derived using the scalar quantities, including $U_m(z)$, measured by each platform. This bulk estimation facilitates comparison for this case where the buoy does not directly measure the fluxes. The TOGA-COARE bulk flux algorithm (Fairall et al., 1996) was applied to both buoy and aircraft data to derive U_{10n} . The rms difference between measures is 1.1 m s^{-1} and close overall agreement is apparent over the available dynamic range.

A separate comparison is made using flights over the University of Miami's Air-Sea Interaction Sensor (ASIS) (Graber et al., 2000) during SHOWEX in November of 1999. The maximum time and distance between surface and air measurements is 15 minutes and 10 km, respectively. ASIS data are derived from three separate platforms operating during SHOWEX and all ASIS estimates, including eddy correlation fluxes, represent a 20 minute averaging period. The middle panel of Fig. 2-1 provides intercomparison of U_{10m} , computed using eddy correlation u_* and scalar estimates from both sensors, and following Eqs. 2.2 and 2.3. The bottom panel displays ASIS vs. aircraft friction velocity estimates. The linear regression correlation coefficient for both of these ASIS intercomparisons exceeds 0.94. The rms difference between U_{10m} measures is 1.0 m s^{-1} . Overall agreement between both the flux and wind estimates in Fig. 2-1 indicates the aircraft wind data are well calibrated.

2.2.2 Laser altimeter system and surface slope statistics

The aircraft houses three down-looking laser altimeters, mounted to form an equilateral triangle in the horizontal plane with leg spacing of 0.96 m. This provides three simultaneous wave elevation measurements as the aircraft traverses over the surface. The sensor geometry and processing, including aircraft motion compensation, are discussed elsewhere (Sun et al., 2001; Vandemark et al., 2001). The synchronized sea elevation estimates are used to compute a surface wave slope vector at roughly 1 m spaced horizontal intervals along the aircraft ground track. The 1 m horizontal spacing of the mounted lasers limits the wavelengths resolved to $\lambda > 2m$. For a 5 km flight segment nominally 5000 individual slope measurements are made. The slope vector is given as $\mathbf{s} = s \cos(\alpha)\hat{i} + s \sin(\alpha)\hat{j}$, where α is the azimuthal angle with respect to North, the slope magnitude is $s = \tan(\beta)$ and β is the angle up from horizontal. The slope probability density function (*pdf*) for these intermediate to long-scale gravity waves is thus obtained (Vandemark et al., 1999) and the variance, skewness, and kurtosis directly computed for each data segment. Triply-redundant wave elevation statistics, including H_s (defined as 4 times elevation rms), are obtained as well. Finally, a transect wavenumber spectrum can also be computed from data along a given flight track. But note that this is an encounter spectrum and, given the aircraft's nominal speed of 50 m s^{-1} , a swell or sea's true wavenumber will suffer significant Doppler shifts. While not the focus of this study, transect spectra have been utilized for the case of flight

legs oriented along the wind and wave direction (Melville and Matusov, 2002; Sun et al., 2001). Our preliminary inspection of the high wavenumber portion of Doppler-corrected transect spectra for varied wind conditions supports the form $k^{-3.0\pm 0.1}$ down to the 2.5 radm^{-1} cut-off in the equilibrium subrange (e.g. Banner et al., 1989). Future analysis intends to assess the level of variability for this high wavenumber subrange.

The fidelity of the laser-measured wave height and slope statistics depends upon precise compensation for the continual laser pointing angle changes due to aircraft motions. Fig. 2-2 illustrates the quality of these corrections for the case where the aircraft performed large roll maneuvers over nearly smooth inland water. Aircraft-estimated wind speed over the Currituck sound was 2.5 ms^{-1} for this data segment. After correction, results should indicate a nearly flat sea surface. Raw 50 Hz aircraft roll and laser-derived aircraft altitude, sea surface elevation and slopes are displayed for a 2.5 km ground segment (~ 2500 data points). A running estimate of mss_l is provided via a 200 m along track sliding average for $\langle s_i^2 \rangle$. The computed elevation standard deviation is below 3 cm and the variance for mss_l falls below $3.e-4$. Estimated H_s is 0.10 m and mss_l is $1.2e-03$, both indicative of a surface that is 10-30 times smoother than typical open-ocean conditions. Results from repeated inland water legs under such maneuvers are used to estimate that open-ocean rms wave height and slope uncertainties typically fall below 3 %. As critically, even for these uncharacteristically large aircraft motions, wave data exhibit little correlation with that variation.

Comparison of buoy and aircraft-derived H_s measurements provides further validation. Intercomparison data are extracted from the same ASIS and NDBC data subsets discussed in the wind comparisons above. Results indicate that the standard deviation between buoy and aircraft H_s estimates falls below 0.15 m and the linear regression coefficient exceeds 0.92 over the 60 samples in the intercomparison.

2.2.3 Radar scatterometer

A Ka-band (36 GHz, $\lambda_0 = 8.3 \text{ mm}$) scatterometer, pointed directly normal to the surface, is used to collect reflected power measurements from the roughened sea surface as detailed in Vandemark et al. (2001). Measured receiver voltages are converted to normalized radar

cross section using the radar equation:

$$\sigma^o(0^\circ) = \frac{P_r(4\pi)^3 r^4}{P_t G^2 \lambda_0^2 A} \quad (2.4)$$

where P_t and P_r represent the receive and transmit power levels, G the antenna gain, λ the radar wavelength, r is the laser-derived distance from the sea to the antenna, and A the effective observed surface area. All parameters are accurately determined and cross-checked through rigorous calibrations. Absolute calibration of the microwave system is carried out by measurement of P_r off a series of calibrated point targets before and after each measurement campaign. The radar is also equipped with an internal calibration loop, continual transmit power monitoring, and internal temperature control to better than 2 °C. External calibration results indicate an uncertainty of ± 0.4 dB in the absolute level. Precision for a given estimate approaches ± 0.2 dB for a given 5 km segment average in this study. This precision holds between successive campaign measurements as well as from point-to-point on a given day. This is a system with high horizontal resolution, having a 1 m surface footprint when flown at 10 m altitude. Data processing to provide the averaged σ^o over a given 5 km flight leg is discussed in the noted reference. The appendix describes a small σ^o correction required to adjust the wider beam antenna data collected here to that measured by a narrow beam system such as a satellite altimeter.

2.2.4 Radar-inferred slope estimates

A common use for near vertical-incidence radar data is the inference of the surface mean squared slope, mss . Under a Geometric Optics radar scattering assumption and assuming that the slope *pdf* conforms to a directionally-uniform Gaussian form, the omnidirectional slope variance can be inverted via the inverse relationship (Barrick, 1968a):

$$\sigma_{K_a}^o(\theta) = \frac{|R(\theta)^2|}{mss'_{K_a}} \sec^4 \theta \exp\left(-\frac{\tan^2 \theta}{mss'_{K_a}}\right) \quad (2.5)$$

where θ is the incidence angle from vertical. In this study the view angle is $\theta=0^\circ$, the nominal configuration for the satellite altimeter and for the present aircraft data. Thus θ dependence on the right-hand side vanishes to leave the leading fractional term, i.e. eq. 2.1. σ^o in this study refers to $\sigma_{K_a}^o(0^\circ)$. The Fresnel reflectivity factor ($|R(0^\circ)^2|$) at Ka-band is estimated to fall between 0.52 and 0.55 for the salinity and water temperatures

encountered during our measurements (Stogryn, 1997). This factor's 1-3 % variation is accounted for in presented mss'_{Ka} estimates based on this Stogryn model and aircraft-measured sea surface temperatures. Note that no effective Fresnel coefficient is imposed in the development. It has been traditional to invoke such a term in lieu of the true Fresnel factor to account for unexplained disagreements between observations in both the overall bias between observed σ^o and mss and in the wind dependence for these two variables (e.g. Valenzuela, 1978). Chapron et al. (2000) argues that this tuning term is not necessary if one reexamines the radar and optical measurements to include the effects of slope *pdf* peakedness and present understanding of the absolute calibrations for Ku-band satellite data sets.

A prime notation is attached to all radar-derived mss estimates to explicitly tie these measurements to the approximations of Eq. 2.5. While mss' may correlate well with an optically-derived mss estimate, numerous uncertainties remain in quantitative comparisons that fall outside of this study's main objectives. These include the issues (see Jackson et al., 1992; Chapron et al., 2000; Plant, 2002) of slope *pdf* nonGaussianity, cm-scale wave steepness and diffraction of incident radiation, and wave directionality and spectral content at all scales. That said, it is asserted that Eq. 2.5 is adequate for the objectives at hand.

The optical scattering assumption implies the incident radiation wavelength is much shorter than all roughness lengths on the surface. For microwave probing of the ocean surface this is typically violated due to the presence of steep gravity-capillary and capillary waves (Jackson et al., 1992). Thus, to first-order, the slope variance estimate of eq. 2.5 is considered as a partial integration, encompassing waves greater than $3\lambda_0$ ($k_f = k_0/3 = 250 \text{ radm}^{-1}$). This means wavelets longer than 2 cm for a Ka-band sensor.

Most important to this study is the coincident and direct measurement of the omnidirectional slope variance acquired by the lasers. This integration over the directional slope spectrum is obtained up to the laser geometry-dictated cutoff wavenumber of $k_l \approx 3 \text{ radm}^{-1}$:

$$mss_l = \int_0^{|\mathbf{k}|=k_l} |\mathbf{k}|^2 S(\mathbf{k}) d\mathbf{k} = \langle s_i^2 \rangle \quad (2.6)$$

This is the omnidirectional value, representing slope integration over wavenumber and azimuth angle α . The wavenumber vector is $\mathbf{k} = k \cos(\alpha)\hat{i} + k \sin(\alpha)\hat{j}$. The integrand represents the slope spectral density function where $S(\mathbf{k})$ is the directional wave height spectrum.

As discussed, each mss_l estimate is directly obtained over ~ 5000 measured s_i realizations.

Therefore, the radar and laser systems provide complementary surface information over each 5 km flight interval. It is a direct step to combine measurements and infer that short wave portion of slope variance derived from k_l to k_f as:

$$mss'_h = mss'_{Ka} - mss_l \approx \int_{k_l}^{k_f} |\mathbf{k}|^2 S(\mathbf{k}) d\mathbf{k} \quad (2.7)$$

The subscripts l and h are chosen to reflect the integration limits over low and high wavenumber portions of the spectrum respectively. Therefore mss_h represents information on the short gravity and gravity-capillary wave contributions ($\lambda = 200$ to 2 cm). Forthcoming data interpretation makes use of mss_h in attempts to examine the wave scales controlling observed radar backscatter.

2.3 Results

The mean wind dependence of surface estimates under presupposed open ocean wind and wave conditions are detailed first. Measurement locations are shown in Fig. 2-3. The water depth exceeds 20 m for all cases. Samples within 15 km of the coastline are excluded as suggested by recent work on this coastline (Sun et al., 2001; Vickers et al., 2001) showing that the atmospheric boundary layer often contains strong land-advected turbulence within the first 10-15 km from shore. The map also shows the location of the buoys mentioned in section 2.2.

This subset of aircraft data holds more than 2300 5-km samples gathered on 36 separate days over a two year period. Fig. 2-4 depicts the range and frequency of wind speeds observed along with the mean relation between H_s and the wind. The U_{10} distribution highlights that this set is weighted towards moderate wind observations, but a substantial number of high and low wind events are also present. Wave height variation with wind indicates the sea state generally falls below 2.0 m and that, on average, H_s levels reside above a fully-developed sea prediction (Sverdup and Munk, 1947) for low winds, and fall below this criterion for moderate to high winds. The observed levels of H_s fall well below globally-observed mean values at any given wind (Gourrion et al., 2002b). This is not unexpected off this east coast region where swell impacts are limited. All references to U_{10}

from this point forward refer to the 10 m neutral stability value computed using Eq. 2.3.

2.3.1 Wind dependence of long wave properties

Laser-derived slope amplitude statistics and their variation with wind are shown in Fig. 2-5. A wind-dependent bin averaging is performed for all panels, showing a parameter's mean value at a given speed $\pm 0.75 \text{ ms}^{-1}$. The error bars represent 95 % confidence intervals assuming a random distribution using $b_{err} = \pm \frac{1.96 \cdot \sigma_b}{\sqrt{N}}$ where σ_b is the bin standard deviation and N is the sample number within a bin. Also shown in all panels are the optically-deduced predictions (Cox and Munk, 1956), hereafter referred to as CM56. These predictions are for the special case where the surface was altered using oil to limit the presence of short waves. This so-called slick surface was considered to contain waves only greater than about 30 cm, a limit that coincides well with the 2 m limit ($k_l = 3$) of the laser geometry used here. But do note that the present observations are derived from an unaltered ocean surface.

Data in Fig. 2-5(a) provide a clear indication of wind dependence for the longer wave slope variance, mss_l , Eq. 2.6. Recalling Fig. 2-4, one notes that error bar magnitude follows the observed wind histogram. There is a linear trend up to $8\text{-}10 \text{ ms}^{-1}$ that falls about 10 % below the CM56 model. At higher winds, the present data fall further below their prediction, but do indicate a continued, but weaker increase with wind. The one standard deviation levels about the mean indicate 20-30 % variability, likely geophysical as discussed later.

Data also agree closely in form and magnitude with the Phillips' (1977) logarithmic reinterpretation of CM56 results with $k_l = 3 \text{ radm}^{-1}$:

$$mss_l = B \cdot \ln\left(\frac{k_l}{k_p}\right) \quad \text{where} \quad k_p = \frac{g}{U_{10}^2} \quad (2.8)$$

The curves shown represent a bounding of the observations using $B = a \cdot [1., 1.25, 1.5]$ and where $a = 4.6 \text{e-}3$ is prescribed by Phillips under the wind-driven asymptotic limit where a k^{-3} saturation subrange for the wave spectrum is established. At low U_{10} the average mss_l lies considerably above zero in agreement with CM56 estimates. This suggests that, on average, the data set carries a background wave field component at light winds that elevates mss_l slightly above a solely wind-dependent level.

Wind-dependent kurtosis estimates, also derived from the two-dimensional slope amplitude measurements, are shown in Fig. 2-5(b). The kurtosis excess coefficient, γ , is defined as

$$\gamma \equiv \frac{\mu_4}{\mu_2^2} - 3 \quad (2.9)$$

where μ_i is i th central moment of the univariate slope distribution. By definition, γ is zero for the normal distribution. The positive-definite omnidirectional slope distribution for normally-distributed slopes is the Rayleigh distribution for which $\gamma = 0.245$. Data in Fig. 2-5(b) show that γ always lies well above the Rayleigh value, indicating excess in steep and shallow slopes. The measured peakedness is largest for lightest wind and there is a clear decrease with increasing wind up to 10 m.s^{-1} . Above this speed the magnitude rises again. CM56 also inferred non-Gaussian γ levels, but their technique's fidelity in resolving steep waves and the resulting observations provided no evidence of wind dependence. The γ level presented for CM56 is derived from their principle component Gram-Charlier slope fit parameters, C_{40} and C_{04} , and our subsequent omnidirectional simulation relating component slope statistics to those computed over the modulus $|s|$. That simulation is based on the *pdf* generating function discussed in the appendix. Results indicate that CM56's $\gamma = 0.70 \pm 0.35$. CM56 also reported that this peakedness magnitude did not change substantially between the slick and clean surface observations.

While their γ estimate is included here, it is important to note that the CM56 technique involved indirect inference of the variance, skewness, and kurtosis under given assumptions and limitations. This included an inability to measure the true slope variance and the steepest waves, and truncation of their Gram-Charlier fit to fourth order. These are points specific to the CM56 study that should be considered in quantitative definition and use of the slope distribution (Tatarskii, 2003; Chapron et al., 2000). In this case, CM56 γ is given as reference but it is suggested the uncertainty and mean level may exceed what is derived from their truncated fit coefficients.

A similar γ adjustment from one to two dimensions is applied to the wind-dependent findings of Shaw and Churnside (1997, their eq. 17). The resulting fit is shown in Fig. 2-5(b). In all cases, the present data and those of Shaw and Churnside (1997) lie above

CM56. Close agreement in magnitude and wind dependence is observed between present data and Shaw and Churnside (1997). The latter results come from an optically-based field study where the slope *pdf* was deduced over all wave scales, thus including wavelengths much shorter than those measured here. That study also involved a technique with angular resolution that far exceeded the CM56 study and permitted a Gram-Charlier expansion truncated at the eighth order.

Fig. 2-5(c) provides the average estimate of the ratio between crosswind and alongwind slope variances obtained for these longer wave scales. Almost no asymmetry is observed for the lowest wind speed, but with much uncertainty. Otherwise, the data lie between 0.8 and 0.9, indicating weak asymmetry that varies little as the wind increases. No clear wind dependence emerges considering the given uncertainties. The CM56 slick surface model shows close agreement with the present results for winds above 5 m s^{-1} .

Finally, computed slope skewness values (not shown) are small for both along and crosswind estimates, never exceeding -0.1, where negative values assign the most likely slope as falling to the downwind side of the pdf. The mean value for both falls at -0.01 ± 0.20 and uncertainty is too high to assign significance to a small observed magnitude increase with wind seen in the alongwind measure. These findings are also consistent with that observed in CM56.

2.3.2 Wind dependence of Ka-band σ^o

Nadir-view radar backscatter versus U_{10} is shown in Fig. 2-6. As above, the data correspond to the open ocean sample locations shown in Fig. 2-3 and are comprised of more than 2000 observations. The upper panel presents the individual measurements as well as the other available data for this frequency and viewing geometry as obtained by Masuko et al. (1986). There is a large difference between these two studies where the present data consistently lie 5 dB above Masuko data set.

Referring solely to the present data set it is pointed out that the data generally fall ± 1 dB about the mean bin-averaged result with a somewhat larger data spread occurring at moderate U_{10} where the more observations and hence diverse weather patterns were sampled. While this study is primarily focused on the ensemble dependencies, one group of

outlying data are noted. The samples having $\sigma^o = 10\text{-}11$ dB and winds from $6\text{-}10 \text{ m s}^{-1}$ were examined and found to represent data from three days where the swell was opposed to the wind direction and/or a cold air outbreak was in progress over the coast. Such distinctions are being addressed in a paper to follow and are mentioned primarily to highlight the point that data variability observed in Fig. 2-6(a) is foremost physically-driven rather than measurement noise.

The bin-averaged σ_{Ka}^o result shown in Fig. 2-6(a) is repeated in Fig. 2-6(b) with the addition of b_{err} to delimit the estimate confidence interval. This result is then adjusted slightly downward at each wind bin based on the antenna pattern correction model of Appendix A. The adjusted result provides an improved estimate of $\sigma_{Ka}^o(0^\circ)$ for direct comparison to results using narrow beam antennas. One such result is provided on Fig. 2-6(b) as $\sigma_{Ku}^o(0^\circ)$ vs. U_{10} derived from an extensively-validated TOPEX satellite altimeter-derived model at Ku band (Gourrion et al., 2002b), eqns. 3-7) given as :

$$\sigma_{Ku}^o(0^\circ) = f(U_{10}, H_s) \quad (2.10)$$

Here, all aircraft measures of H_s for a given wind bin are fed into eq. 2.10 and averaged to produce the given Ku-band geophysical model function (GMF) curve. Model-predicted $\sigma_{Ku}^o(0^\circ)$ depends foremost upon U_{10} but the added influence of H_s data gained thru eq. 2.10 should serve to adjust globally-derived $\sigma_{Ku}^o(0^\circ)$ results towards the specific H_s wave climate carried in the present aircraft data set (see Fig. 2-4).

Comparison of the wind-dependence between Ku and Ka-band observations in Fig. 2-6(b) indicates close agreement. Below winds of 5 m s^{-1} the Ku-band results fall below those at Ka-band by 1 dB at most, otherwise the data agree to within ± 0.2 dB for winds of $5\text{-}15 \text{ m s}^{-1}$. According to eq. 2.1, holding ms' constant, Ka and Ku-band (14 GHz) results should differ by the ratio of their Fresnel coefficients (~ 0.6 dB) where the Ka-band should fall below the Ku-band data. While the predicted -0.6 dB offset for Ka-band is not consistently observed, absolute calibration of either system to a level better than ± 0.5 dB is understood to be unlikely. This suggests that Ka-band σ^o levels are consistent with prediction based upon a quasi-optical assumption and sensor calibration limitations. Thus results to consider here are that the Ka-band data agree closely with the Ku-band results in their magnitude and mean wind-dependent characteristics, and that the magnitude of $\sigma_{Ka}^o(0^\circ)$ data cited in Masuko et al. (1986) should be regarded with caution.

Next, $\sigma_{Ka}^o(0^\circ)$ data are converted to a slope variance parameter, mss'_{Ka} , as discussed in section 2.2 with results shown in Fig. 2-7. To give a sense of the overall supposedly geophysical scatter, the standard deviation for a given wind bin is also depicted. As is common, mss'_{Ka} is compared here to the optically-derived clean surface model of CM56 and one sees the radar-derived results follow that model at light winds and tend towards a 70-80 % fraction of that prediction at moderate to high U_{10} . The present data follow a logarithmic fit quite well from 1-15 ms^{-1} , having the form $mss'_{Ka} = 0.019 * \ln(U_{10})$.

Jackson et al. (1992), among others, provide extensive comparison between radar and optically-derived mss estimates. The close agreement observed between present Ka-band and TOPEX altimeter Ku-band results suggests these new mss'_{Ka} estimates will follow that work, at least as far as mean wind dependence is concerned. One notable point in that regard is that the present data are derived directly from absolute nadir-view σ^o as for the satellite altimeter, whereas much of the recent aircraft work uses an alternate approach (e.g Jackson et al., 1992; Walsh et al., 1998; Vandemark et al., 1997; Hesany et al., 2000) where the σ^o variation with θ is measured. One then estimates mss' via eq. 2.5.

2.3.3 Long wave impacts

A point to recall is that this data set, while regionally limited, is extensive in its sampling at wind speeds below 12 ms^{-1} . Flight data were acquired under differing synoptic conditions and in this section the observed variability in aircraft wave estimates at fixed wind speeds is examined. A main objective here is to quantify the extent of wind-independent long wave variations and their impacts upon σ^o , and equivalently on mss'_{Ka} . As a first illustration, consider a spatial partitioning of the data set into inland, coastal and open ocean observation subsets. Fig. 2-8 depicts sample locations for the former two cases while Fig. 2-3 provides the latter. Both mss_l and mss'_{Ka} estimates are averaged versus U_{10} for each of these zones and the results given in Fig. 2-9. No wind bin holds fewer than 5 estimates. Note that the inland water was sampled less often than for the other cases. The unique perspective provided by the aircraft shows that for a fixed wind there is a clear overall increase in the roughness measured by both the radar and laser systems as one progresses from the sheltered to open waters. Results hold for $U_{10} = 3 - 12 ms^{-1}$ in a fairly consistent quantitative manner where a factor of two to three increase in mss_l is observed from inland to open waters. Note that

this average result represents the ensemble over varied on-, off-, and along-shore wind and wave situations, yet the general smooth-to-rough picture always holds across the inland-to-open sea transition. Changes in mss'_{Ka} follow the same trends but are smaller, of $O(20-50\%)$.

The observed magnitudes in mss variation indicate that $\int k^2 S(k) dk$ varies significantly from shore-to-sea. The partitioning chosen here is perhaps less physically attractive than data division by other wave field descriptors such as wave age, fetch, or sea vs. swell content. But a depiction of the long wave control on the overall slope variance (mss'_{Ka}) does emerge. Using eq. 2.7, mss_h results of Fig. 2-10 show the retrieved high wavenumber information for these disparate wave zones. It is evident that the data collapse onto a single wind-dependent curve closely approximated as

$$mss'_h(U_{10}) = 0.004 + 0.0093 * \ln(U_{10}) \quad (2.11)$$

and that all estimates agree to within 5 % over the range of $3-12 \text{ ms}^{-1}$. As with mss'_{Ka} , a logarithmic form in U_{10} holds for mss_h , indicating a change in sensitivity at a speed of $\sim 7 \text{ ms}^{-1}$. The wind-generated short waves appear to adhere to the same form over the diverse range of longer gravity wave tilting conditions. The overall convergence of the data suggests that, in an average sense, most sea-to-shore mss'_{Ka} variability observed in Fig. 2-9 is due to long wave scales, i.e. those with λ exceeding the laser system's 2 m cut off.

Results of Fig. 2-10 raise the question of whether the observed high wavenumber signature is indeed solely dependent on U_{10} . One means to assess this question is to stratify $mss_h(U_{10})$ against the long wave slope variance. Results for two disparate mss_l levels are provided in Fig. 2-11. Here data from both coastal ocean and open ocean sampling were included in the averages to improve the statistical confidence. Estimated means do not differ substantially from those obtained using only the open ocean data.

Recall that the mss_l estimator represents an azimuthally- and spectrally-integrated parameter and therefore serves as an average for the overall gravity wave steepness, albeit weighted towards shorter gravity waves. Referral to Fig. 2-9 indicates that the low and high mss_l values chosen for Fig. 2-11 represent nominal levels for light-to-moderate and high winds, respectively. Fig. 2-11 mss_h estimates for these mss_l levels indicate close agreement at winds of $5-7 \text{ ms}^{-1}$ but a systematic difference above this velocity. The short-

wave roughness is higher for the smoother long wave level, $mss_l = 0.012$. The difference holds for U_{10} of 7-13 ms^{-1} . Above this point, sampling at the low mss_l level is not available. At the higher winds, these observations can be considered to contrast mss_h for the case of smooth seas, where the wave field is underdeveloped (the low mss_l level), with the case of fully-developed and/or a mix of sea and swell (the high mss_l level). Under this rendering one sees as much as a 60 % mss_h roughness increase for the smooth seas relative to the rough. Results clearly indicate that for winds above 7 ms^{-1} this short-wave signal can vary systematically with the wave field independent of the mean wind speed. An additional check of this behavior is obtained by replacing mss_l with H_s in reproduction of Fig. 2-11. Results are not shown but they provide the same qualitative picture, lower H_s correlates with increased mss_h .

2.4 Discussion

The laser-derived slope data of section 2.3 provide field measurements having several key features. First, the fidelity of direct slope measurements is likely to be superior to optical glint deduction, and to the ill-suited approach of inferring higher-order wave slope statistics via temporal buoy-based acceleration data under a quasi-linear dispersion model. Moreover, these measurements do not require oil dampening to artificially impose k_l . Finally, the extensive data set provides a robust new source for intercomparison with the nine independent slick surface realizations of CM56 that have long served as a baseline for numerous wind-wave, air-sea interaction and remote sensing modeling efforts.

In an overall sense, the accord with CM56 results seen in Fig. 2-5 is impressive. As one expects, the present mss_l data fall slightly below CM56, in line with the estimation that k_l was 20 for that study compared to 3 here. Qualitatively, the data above $U_{10} = 3 ms^{-1}$ provide further support for a logarithmic, rather than linear, mss_l dependence upon wind. For a quantitative fit to the data we use the saturation subrange form of Phillips' (1977) where the model is scaled solely by the wind-independent coefficient in eq. 2.8. Fig. 2-5(a) shows that $B = 5.7e - 3 \pm 25\%$ spans the $\pm\sigma$ for the observations. Note that the upper bound nearly matches the CM56 result where k_l is 6 times higher. This point suggests the uncertainty resident in estimating mss_l wind dependence based on limited field

observations. As a further point, the present mean results are derived over an ensemble that includes few, if any, classical fully-developed sea cases. It is more typical to find in this data a mix of over and under-developed vantage points with the seas either decaying or building. Phillips' form estimates mss_l assuming that the total is derived only from wave scales having $k < k_p$; the peak wavenumber for a fully-developed sea. Thus, at least at moderate winds, one might suppose that the central value for B represents the fully-developed sea while the upper limit tends to a mixture of sea and swell and the lower limit towards that of young or dying seas. The supposition is more tenuous at winds above 10 m s^{-1} where H_s levels in the present data set indicate that observations were generally for young seas. Thus a fully-developed estimate likely tends towards the upper bound. These issues are addressed further in Fig. 2-12 to be discussed shortly. Note that use of an equilibrium model (e.g. Banner, 1990) in lieu of the saturation subrange assumption leads to similar qualitative interpretation.

Regarding other gravity-wave slope statistics, data here agree with the findings of CM56 regarding minimal slope skewness and an observed cross-to-alongwind slope variance ratio of about 0.85, both parameters varying little with change in the wind. Distribution peakedness levels in Fig. 2-5(b) also affirm the long wave slope *pdf* nonlinearity deduced by CM56. Present observed levels are measurably higher than for CM56 and depict a wind dependence not seen in that data. These differences are likely a result of the higher fidelity in the present direct slope measurement approach. What do the differences tell us? Firstly, that gravity wave nonlinearity is a fundamental feature in the long-wave slope *pdf* and is perhaps greater than supposed. Theoretically, under a narrow-band dominant wave framework, kurtosis excess in the wave slope *pdf* is indicative of third order nonlinear wave-wave interactions (Longuet-Higgins, 1963) whereby a correlation between the dominant long wave and short-scale gravity waves exists. This non-zero correlation is evidenced by the increased occurrence of steep wavelets near the long wave crests and flattened areas within the troughs. These interactions also act to drive directional uniformity at the short scale, consistent with the low observed difference between the along and crosswind mss_l . While no generalized theoretical model exists for depicting these nonlinearities over all of $S(k)$, recent study of the nonGaussian slope *pdf* (e.g. Liu et al., 1997; Chapron et al., 2000) suggests that γ may be empirically related to the wave spectral bandwidth parameter

and to the inherent compounding of nearly Gaussian processes at multiple gravity wave scales. The wind dependence observed in Fig. 2-5(b) is consistent with a dependence on wave-wave interactions. These interactions can become predominant in the low wind, low mean slope environment where wave groupiness and multi-model wave fields can force local peakedness in the absence of wind. As wind levels increases, the data indicate γ tends toward a local minimum suggesting the most linearized situation comes at moderate winds, while as the wind increases past 10 ms^{-1} it may be that the weight towards young seas within this data set provides enough active wave breaking to increase the level of wave steepening once again. Strong directionality of the intermediate-scale gravity waves may also play a role in explaining observed γ values, especially at light winds. In this case even weakly nonGaussian slope distributions in the along and cross wind directions can lead to a strongly peaked 2-D distribution. While not shown, a picture similar to that of Fig. 2-5(b) emerges if one replaces U_{10} with mss_l .

Section 2.3.3 provides a view of diverse wave climates and slope *pdf* dynamics for various fixed wind speeds. Fig. 2-9 illustrates the mss_l variability encountered as one spans inland, coastal and open water. The obvious extreme of inland water, obtained over the shallow (depth $< 5 \text{ m}$) Currituck sound, provides data with no swell and limited seas, along with requisite wave dissipation. In this case, one sees mss_l tends to very low levels at light wind and a factor of 3 below the open ocean at the moderate speed of 7 ms^{-1} . While not shown, the levels of slope peakedness are also reduced consistent with the expected reduction in nonlinear wave-wave interactions. A more in depth look at mss_l variations within the coastal zone can be found in Sun et al. (2001).

Overall, mss_l variability for a fixed U_{10} is not small and likely warrants consideration in modeling and inversion studies related to remote sensing of waves and wind near the coast. This is particularly true for sensors most sensitive to the lower wavenumbers such as the low-incidence angle radar scatterometers, altimeters, and envisioned L-band systems for sensing ocean salinity and wind.

The ad hoc wave zone partitioning used to generate Fig. 2-9 is one means to elicit tilt field variability. To further illustrate this variability at a fixed wind speed, results from two open ocean aircraft data collection segments are contrasted in Fig. 2-12. The flight transects were 5 km long and flown in the alongwind direction in both cases. Transect

wavenumber spectra (1-D) and slope *pdf* (2-D) data are provided. The *pdf* results for the slope magnitude are derived from the individual facet slopes as discussed in section 2.2. Each transect (one-dimensional) slope spectrum comes from an encounter wave height-wavenumber spectrum ($S(k_x)$) computed using the alongtrack wave elevation spatial series data ($\eta(x)$) collected using one of the aircraft's laser altimeters. The cumulants displayed represent the alongwind variances $\langle s_x^2 \rangle$.

The low slope ($mss_l = 0.014$) case represents a young sea plus old swell case while the higher slope ($mss_l = 0.024$) example is one of a developed sea and swell. H_s is 0.8 m for the former and 2.1 for the latter. Clearly, for these 8 m s^{-1} wind speed cases the overall surface tilt fields differ substantially. The 2-D *pdf* results show the substantial discrepancy between surface steepness for the two cases. Recall that these are slope measurements derived across a 1 m facet scale. The spectrally-resolved data for along wind flight legs, including cumulative alongwind mss_l estimates, provide a sense of the wave scales dictating mss_l . For example, there is measurable swell energy present for the low slope case at $k=0.05 \text{ rad}\cdot\text{m}^{-1}$, but its magnitude in the slope spectrum and upon the mss_l estimate is negligible. What drives the large difference between these two realizations are wave scales from $k=0.2$ to $1 \text{ rad}\cdot\text{m}^{-1}$. Within the equilibrium subrange from $k=1-3 \text{ rad}\cdot\text{m}^{-1}$ the differences are smaller and the contributions to mss_l similar.

The control of mss_l variability by relatively low wavenumbers suggests that operational wave buoy data may serve to examine and bound the extent of wind-independent mss_l variation. The nominal cutoff wavenumber for NDBC wave buoy directional wave measurements is provided on Fig. 2-12. This implies that a substantial fraction ($\approx 30 - 50\%$) of the example mss_l , could be inferred via the measured buoy acceleration variance. Indeed, multiyear climatologies of buoy-derived mean squared acceleration for regions such as the Great Lakes, Hawaii, and the U.S. West coast (Gourrion et al., 2002a) suggest a dynamic range in this longer wave slope variance of $\pm 60-80\%$, not unlike that observed in the mss_l results of Fig. 2-9.

Discussion of the presented radar backscatter data can be couched in terms of (a) examining multi-frequency σ^o observations, (b) long-wave effects on altimeter backscatter, and (c) the radar-inference of surface wave information.

(a) First, regarding multi-frequency observations of σ^o , the present radar measurements were undertaken in part to reproduce past nadir-view Ka-band data (Masuko et al., 1986). While only a small sampling, those past results indicate a large difference between reported X- and Ka-band σ^o estimates that lies far outside that predicted solely based upon the 0.6 dB difference between the respective Fresnel reflection coefficients. Several studies (e.g. Jackson et al., 1992; Walsh et al., 1998) suggest those Ka-band data are much too low in an absolute sense, and inconsistent with what is known from other radar observations (e.g. Jackson et al., 1992; Chapron et al., 2000) and from optically-derived slope spectral density data at high wavenumbers, while others (e.g. Apel, 1994) make use of the Masuko data to infer an accordingly increased slope spectral density at these wave scales. The new data of Fig. 2-6(a) show a large 5 dB discrepancy that supports the former view. Section 2.3 results also show the present data to be consistent with satellite observations at Ku-band to within the error of $O(1 \text{ dB})$ system calibrations. Results are also consistent with the calibrated Ku-band tower data of (Melville et al., 1991). Finally, it is noted that the Masuko et al. (1986) data were obtained by averaging of log amplifier outputs. This would serve to bias both their X and Ka-band estimates by 2-3 dB. But this would not alter their observed 5 dB difference between frequencies. We conclude that the present Ka-band results are a preferred choice for physically-based interpretations and for spaceborne sensor signal-to-noise design considerations.

The wind-dependence of open ocean aircraft Ka-band results are shown to nearly replicate the Ku-band TOPEX altimeter model function (Gourrion et al., 2002b) in Fig. 2-6(b). This agreement between a globally-derived satellite result and data from off U.S. East Coast suggests a robust mean relationship between wind and $\sigma^o(0^\circ)$ consistent with numerous past aircraft studies (e.g. Jackson et al., 1992; Vandemark et al., 1997; Hesany et al., 2000; Chen et al., 2001). Certainly these aircraft data closely emulate Ku-band altimeter backscatter characteristics in a mean sense that suggests their utility for supporting satellite data interpretation.

The close agreement at all U_{10} between the Ka and Ku-band systems is not completely in agreement with that found between C- and Ku-band σ^o using systems aboard the TOPEX satellite (Elfouhaily et al., 1998). In that study a wind dependent C-Ku band σ^o difference is observed for moderate to high U_{10} , increasing with U_{10} from 0.1 to 1.0 dB. This trend is

attributed to increase in short-wave spectral content following optically-derived results on the increase in wave density at high wavenumbers with U_{10} (Hwang et al., 1996; Elfouhaily et al., 1997). This logic predicts the mean difference between Ka and Ku-band σ^o data should exhibit a similar wind-dependence but with a slightly reduced magnitude. This study does not contain the coincident Ku and Ka-band data needed to examine this small difference signal. The aircraft versus satellite model results of Fig. 2-6(b) show no clear wind dependent depression of σ^o at Ka with respect to Ku-band like that seen for C and Ku-band. Given the small expected signal we consider the results inconclusive. At best they suggest wind-dependent change between nadir-view σ^o at radar λ_0 of 2.1 and 0.83 cm is small. One consistency between Elfouhaily et al. (1998) and this study is seen in their Fig. 2c and the present study's Fig. 2-11 where both observations indicate long wave field control on short waves as discussed below. One inconsistency is that we see no large 3 dB frequency-dependent (Ku-to-Ka) offset like that observed between C- and Ku-band for the TOPEX altimeter (Elfohaily et al., 1998). It is our contention that the wind-independent 3 dB TOPEX bias is largely due to calibration error (Chapron et al., 2000). Regardless, absolute calibration for the satellite altimeter C-band systems (TOPEX and Jason-1) is not performed at a level sufficient to achieve scientific certainty beyond the 1-2 dB level. Accurately calibrated data is needed to fully resolve this issue.

(b) Coincident observation of σ_{Ka}^o and mss_l in this data set provides a unique perspective for assessing the impact of tilt field variability upon altimeter backscatter. It is physically-expected that the total integrated slope variance, and hence altimeter backscatter, will be subject to change with U_{10} , but also with a changing directional long wave field that is potentially uncoupled from the wind. The quasi-optical prediction of eq. 2.5 and a two scale surface model where $mss'_{Ka} = mss_l + mss_h$ (see eq. 2.7) provide a simple framework to investigate the issue. But obtaining comprehensive mss_l data sets is uncommon. Several recent satellite altimeter studies attempt to quantify such uncoupled long wave impacts using surrogates for mss_l such as H_s , significant slope, and wave age (Gourrion et al., 2002a; Hwang et al., 1998; Gommenginger et al., 2002; Gourrion et al., 2002b). Present laser-derived slope measurements provide mss_l directly and for every data sample in the set.

Results of Fig. 2-9 show mss_l and mss'_{Ka} increasing together at any fixed U_{10} . Knowing

that mss_l variation is carried within the mss'_{Ka} integral, this is direct evidence for long-wave slope control upon the radar backscatter, and a clear rendering of a two scale surface response (eq. 2.7) where it is primarily the overall steepness of long-wave tilting facets that increases as one heads to sea. This, rather than changes at high wavenumber, explains first-order change in mss'_{Ka} (or σ^o) in Fig. 2-9. The mss_h estimates of Fig. 2-10 provide additional support. In a mean sense, there is invariance in this short-scale slope term between inland, coastal and open ocean waters.

The impact of mss_l variability upon altimeter σ^o is not always small. Taking for example a linear dependence between wind and mss , observed 30-40 % changes in mss'_{Ka} will lead to equivalently large altimeter-derived wind errors. Errors of this scale were inferred for the open ocean (Gourrion et al., 2002b) and elsewhere and are directly affirmed here. Similarly, the results imply that optically-based field estimation of wind-dependent total mss should consider mss_l variability following work such as Hwang and Shemdin (1988).

(c) Radar-derived slope variance estimates are explicitly linked to the model of Eq. 2.5 to emphasize that mss'_{Ka} and mss_h estimates make use of σ^o data under specific approximations discussed in section 2.2. Quantitative comparison of results in Figs. 2-7 and 2-10 to optically-derived mss data remains subject to uncertainties and varied interpretation - due in part to absolute calibration issues and to the unresolved surface wave description at all scales and conditions as mentioned in section 2.2. There are, however, several points to be made when considering Figs. 2-7, 2-10, and 2-11.

First, no effective Fresnel term is invoked in deriving mss'_{Ka} , in contrast to recent radar studies (e.g. Masuko et al., 1986; Jackson et al., 1992; Vandemark et al., 1997; Walsh et al., 1998; Hesany et al., 2000). This point reinforces studies such as Chapron et al. (2000) and Plant (2002) suggesting that such a nonphysical 'effective' term is unnecessary when one considers *pdf* peakedness and diffraction in near-nadir radar studies alongside sensor calibration limitations. As one example, Chapron et al. (2000) provides a review of recent near-nadir radar observations (Jackson et al., 1992; Walsh et al., 1998) where mss is derived via the σ^o fall off with incidence angle shown in Eq. 2.5 to show that these efforts are likely underestimating the true mss due to neglect of slope *pdf* peakedness. This underestimation in turn leads to use or modification of the effective Fresnel adjustor. If one adjusts the Ku-band mss results of Jackson et al. (1992) or the nearly equivalent Ka-band results

of Walsh et al. (1998, see their Fig. 11) by the proposed blanket factor of 1.2 then one finds their results agree very well with our mss'_{Ka} data shown in Fig. 2-7.

Second, the variation of mss_h with sea state seen in Fig. 2-11 provides a qualitative picture of likely long-wave short-wave interaction of relevance in several respects. Recall that mss_h decreases for increasing long wave roughness and that this dependency only occurs for winds above about 7 ms^{-1} . Such a result is consistent with that inferred from space (see above, Elfouhaily et al., 1998) and in the laboratory (Donelan, 1987). It is also consistent with prediction of short wave suppression by enhanced breaking due to wind drift and wave current effects under increased mechanical wave energy (Chu et al., 1992). The present mss_h estimator does not resolve the high wavenumber subrange carrying this response but numerous efforts would suggest $70 < k < 700 \text{ radm}^{-1}$. One implication is that a multi-frequency altimeter is potentially sensitive to such long-wave short-wave dynamics. Finally, note the nearly opposite behavior for mss'_{Ka} and mss_h with respect to mss_l change at a given moderate wind speed (Figs. 2-9 and 2-11). While the total roughness $mss'_{Ka} = mss_h + mss_l$ appears to be rising with mss_l , the high frequency component is decreasing. Gourrion et al. (2002b) hypothesized this contrast to be a potential source for the ambiguity observed in the satellite altimeter wind inversion process at moderate to high wind speeds. This appears to be supported by the present results.

2.5 Summary

The field measurements provided serve to clarify and validate several ocean wave roughness observations and models commonly invoked in the study of ocean waves and radar remote sensing of ocean winds. Wave slope *pdf* measurements for $\lambda > 2 \text{ m}$ generally affirm the oft-cited results of Cox and Munk where oil was used to eliminate short wave scales. Present results confirm a slope distribution peakedness that greatly exceeds that for a Gaussian and exhibits a wind-dependence. Both features indicate the presence of nonlinear wave-wave interactions at the intermediate gravity wave scales and occurring at all wind speeds, particularly on the open seas.

The mean wind dependence of Ka-band radar σ^o indicate a high level of agreement with Ku-band satellite altimeters - an expected result. Moreover, the calibrated σ^o data

also indicate that past nadir view results of at Ka-band are biased low by 5 dB. The radar σ° data are then used to infer slope variance at higher wavenumbers, $2cm < \lambda < 2m$, as defined in Eq. 2.7 via combination of laser and Ka-band nadir-view scatterometer data. A key observation is that of long-wave tilt effects upon the observed radar backscatter (and mss'_{Ka}) at any given wind speed. One means used to illustrate this control is partitioning of observations into inland, coastal and open ocean classes. A simple Geometric Optics scattering model, combined with a long and short scale surface separation appears to be adequate to identify and quantify this phenomena. While such results are not unexpected based on many studies, the clarity gained by direct measurement of mss_l over all long wave scales, including any swell, affirms that the primary concern when addressing long wave impacts upon σ° or mss is divining variability within a spectrally-integrated parameter, e.g. mss_l or the mean-square acceleration, that is associated with intermediate gravity wave scales. The present study suggests this variability can be quite large, particularly near the coast, and therefore of some concern in exacting mss measurements and models. Use of terms derived from low order wave spectral moments such as H_s or k_p are unlikely to provide equivalent sensitivity to the effect.

Finally, initial open ocean results of Fig. 2-10 suggest that the radar-deduced slope variance for the high wavenumber subrange is relatively insensitive to the long waves, increasing solely with the logarithm of the wind. A closer look reveals that this is true only for light-to-moderate winds below U_{10} of 7 m s^{-1} . At speeds above this range, a depression in mss_h is observed as the long wave roughness increases. While quantitative spectral isolation of the short wave scales dictating this observation is beyond what the present data can provide, the results are consistent with several past studies.

It is hoped that the present study serves to motivate the consideration of intermediate and long wave scale slope measurements, and their nonlinearity, in future ocean remote sensing work. In particular, the multi-frequency altimeters aboard JASON-1 and ENVISAT, the Ku-band TRMM satellite, and developments involving GPS bistatic scattering and ocean salinity measurements. In all cases, the sensors are sensitive to these wave scales at some level. Satellite extraction of such information may prove useful to the enhanced understanding of the role that slope variance plays in gas and momentum transfer processes. Future work with this LongEZ aircraft data intends to address covariance between momentum flux

variability and the wave scales resolved here.

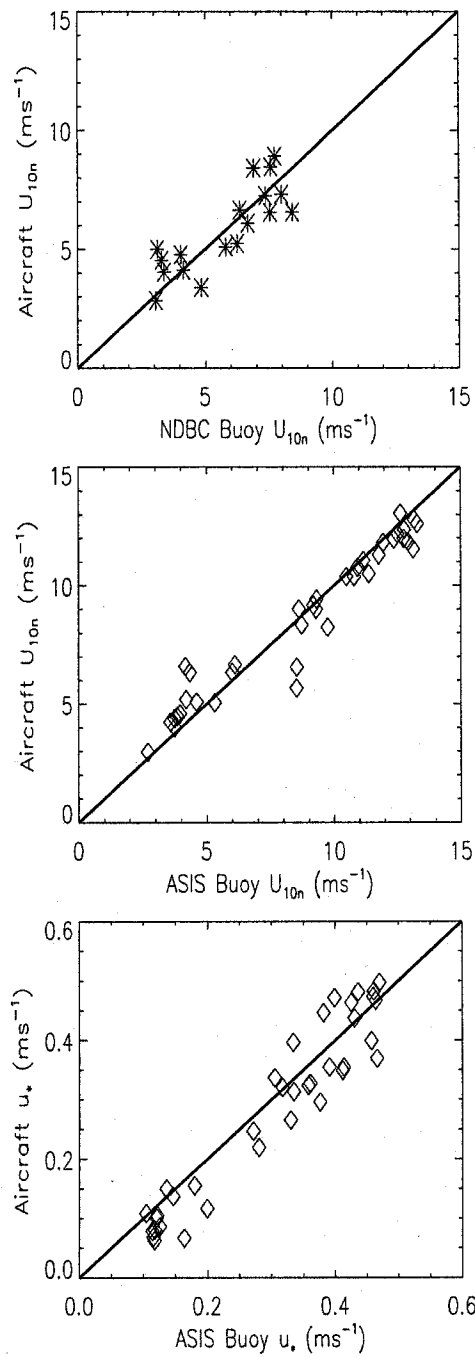


Figure 2-1: Coincident near surface wind estimates. (a) Aircraft vs. NDBC bulk-derived U_{10N} , and (b) aircraft vs. ASIS eddy-correlation derived U_{10N} . Bottom panel presents buoy and aircraft friction velocity estimates for the same ASIS samples shown in (b).

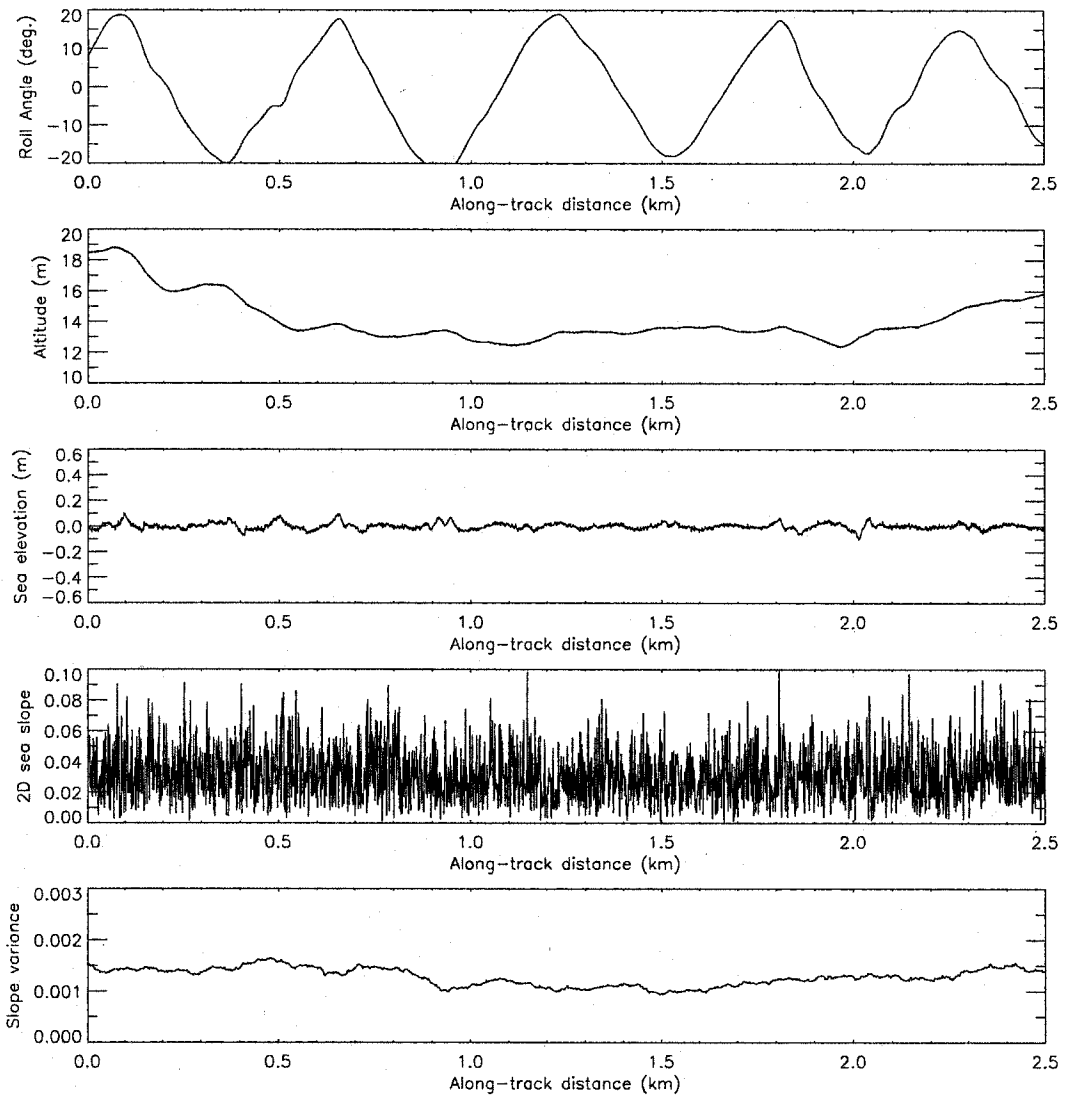


Figure 2-2: Typical calibration flight leg data over nearly smooth inland water. Uppermost panels provide aircraft roll and altitude data. The middle panel shows the laser-derived estimate of the sea surface elevation. Lower panels provide the measured slope magnitudes s_i and variance $\langle s_i^2 \rangle$, respectively, as discussed in the text.

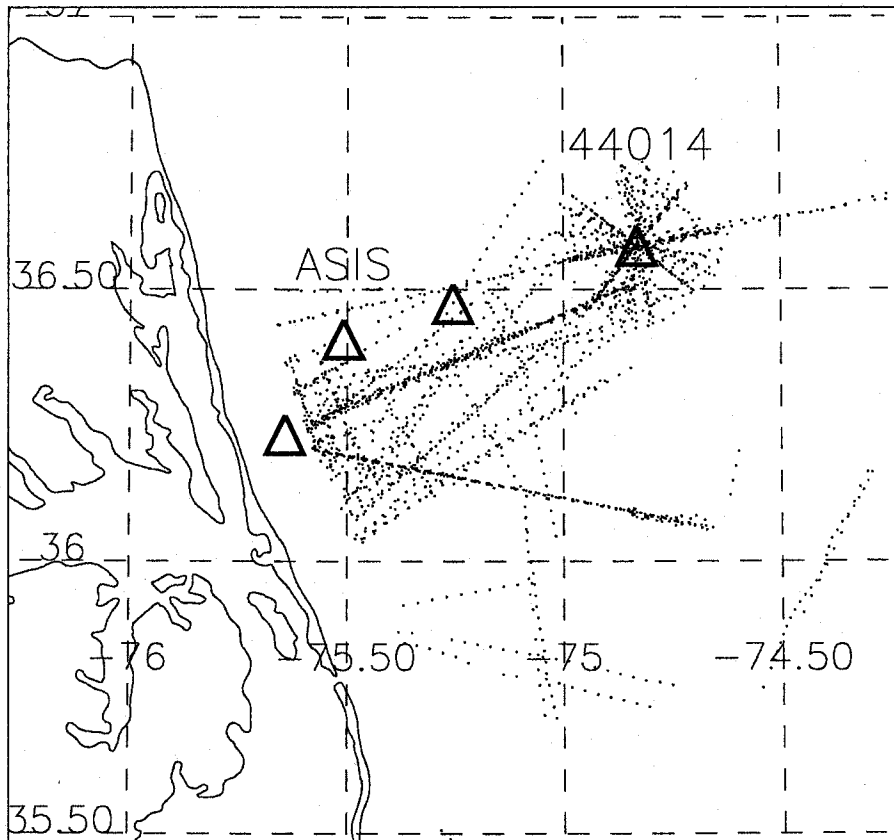


Figure 2-3: The study region including a center location for all 5 km average "open-ocean" aircraft data samples presented. Locations of the three ASIS buoys and NDBC 44014 are noted. Map extent is roughly 100 x 100 km.

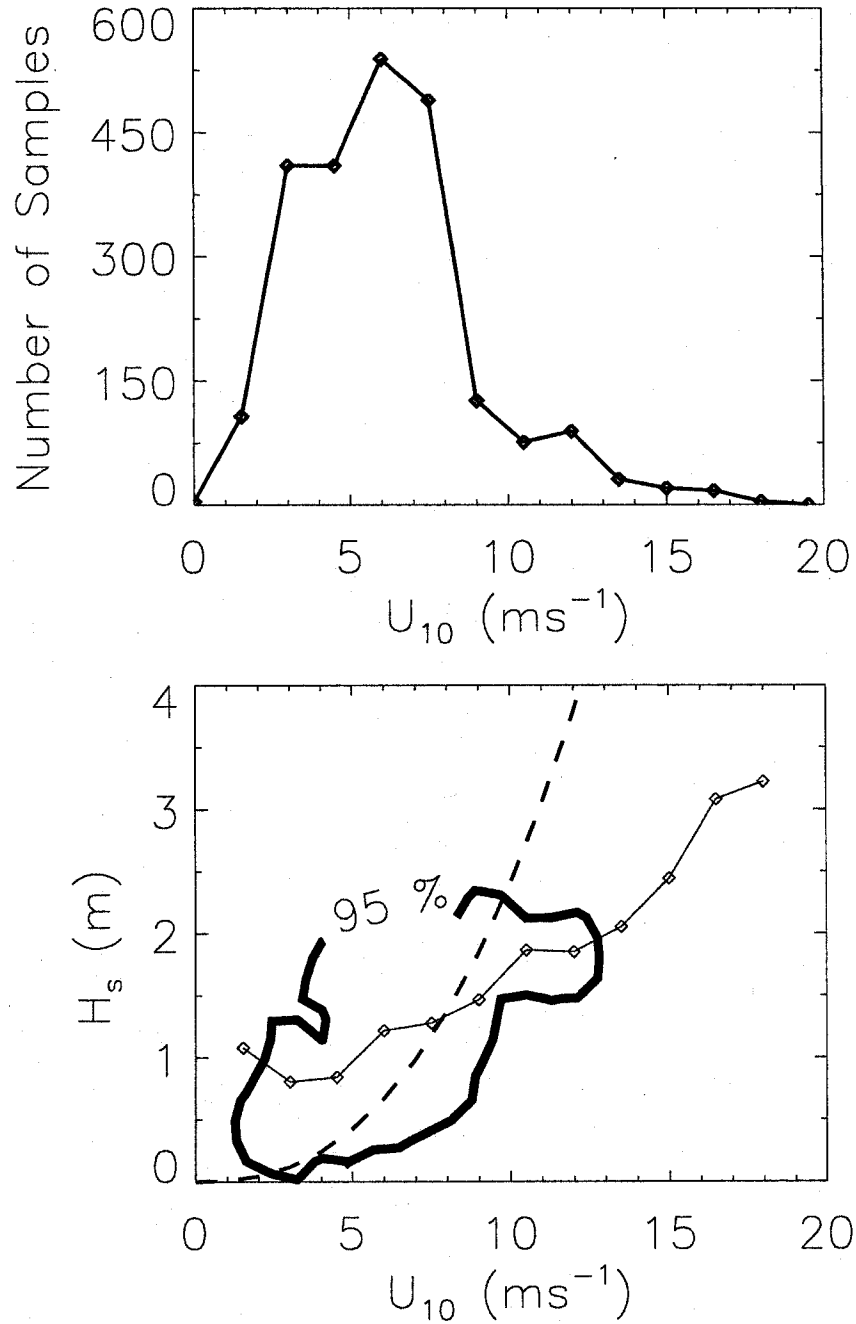


Figure 2-4: (a) Histogram of wind speeds observed within the 2324 sample open ocean data set. (b) Data shows the average of observed H_s vs. wind speed, while the model curve represents the Sverdup-Munk fully-developed sea prediction. Contour provides the 95 % occurrence range for H_s over the range of observed winds.

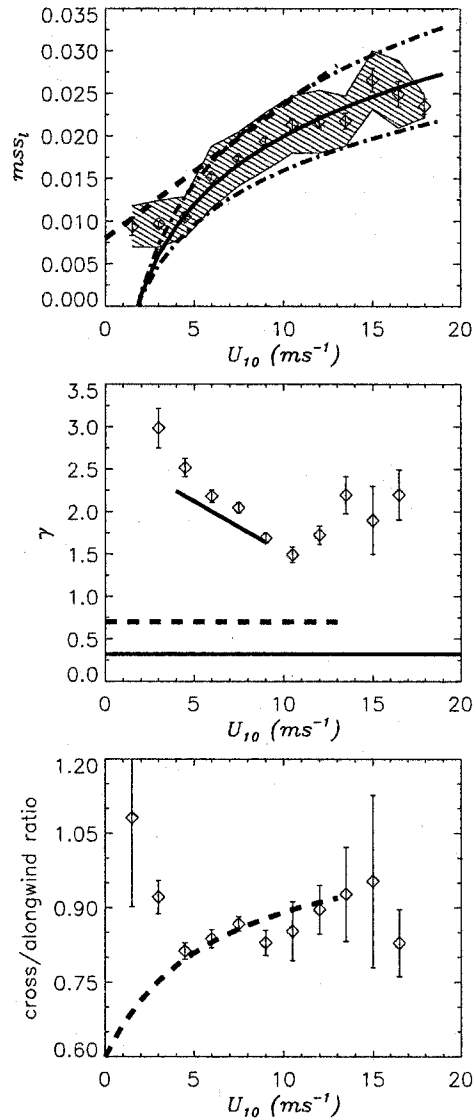


Figure 2-5: Laser-derived wave slope statistics versus U_{10} where (a) is the average of slope variance mss_l in successive $\pm 0.75 m s^{-1}$ wind speed bins. Error bars depict the mean estimate 95 % confidence interval as defined in text. The shaded region indicates \pm one standard deviation for each bin. The solid ($B = a * 1.25$) and dash-dotted curves are for Phillips' logarithmic model as discussed in the text. Also shown is (b) the kurtosis excess coefficient γ , where the uppermost curve is derived from Shaw and Churnside (1997) and the lowest line gives γ for the Rayleigh distribution. The ratio of cross to alongwind mss_l is given in (c). The dashed lines in all panels correspond to Cox and Munk (1956) predictions based on oil-slicked surface observations.

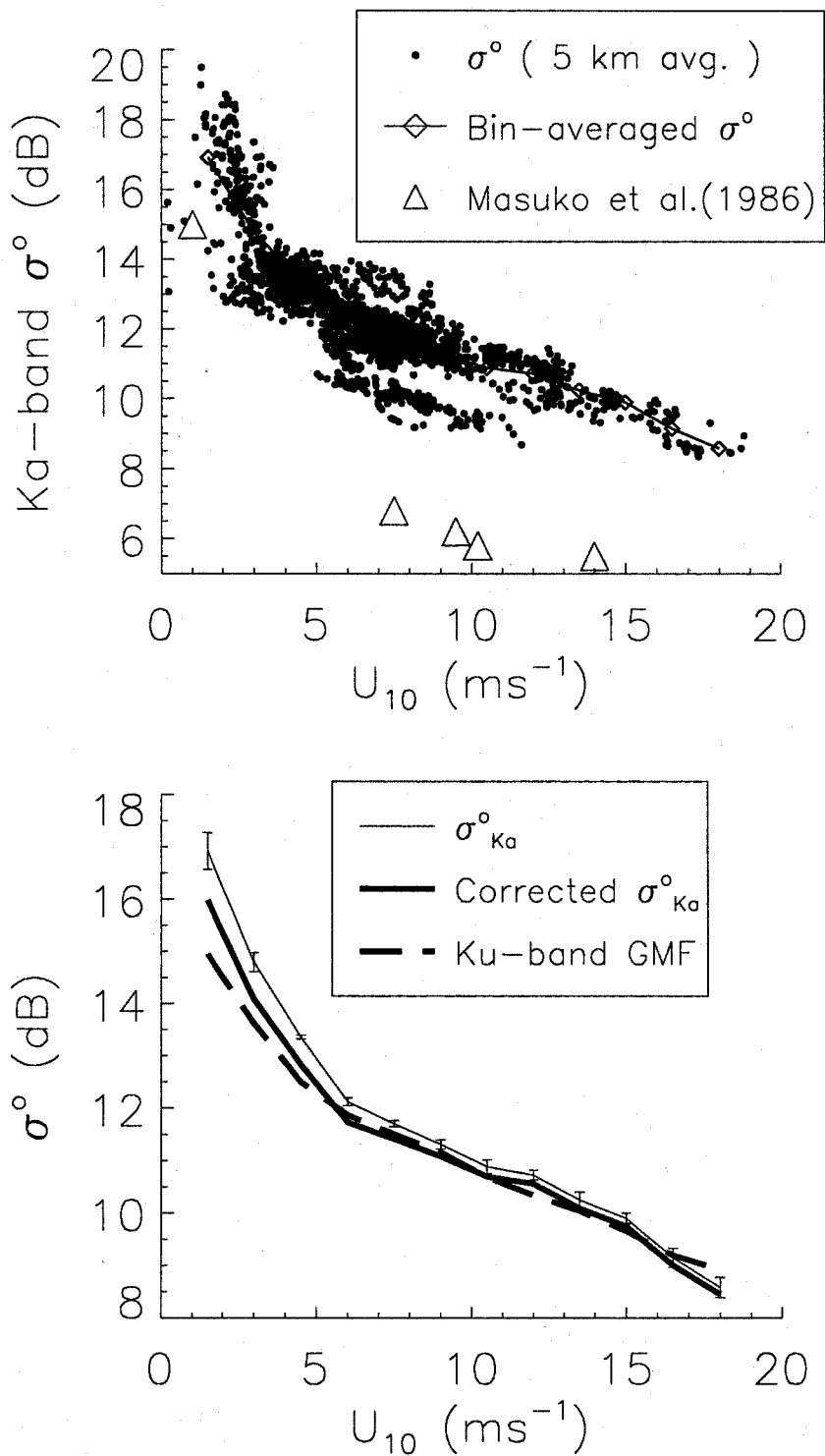


Figure 2-6: Measured nadir-view σ^0_{Ka} versus U_{10} . (a) Individual data are shown along with the bin-averaged results as in Figure 2-5, and Ka-band measurements (\triangle) from Masuko et al. (1986). (b) The aircraft bin-averaged results of (a), results after correction according to appendix A, and a Ku-band prediction based on global TOPEX altimeter observations.

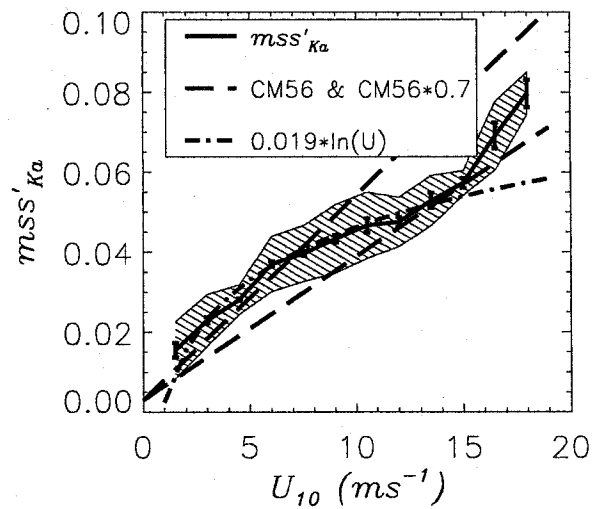


Figure 2-7: Slope variance inferred from σ_{Ka}^2 and bin-averaged versus U_{10} . Error bars and shaded region follow the convention of Fig. 2-5(a). Dashed lines correspond to the CM56 prediction for a clean surface and 70 % of that prediction. The curve is a logarithmic fit to the present data.

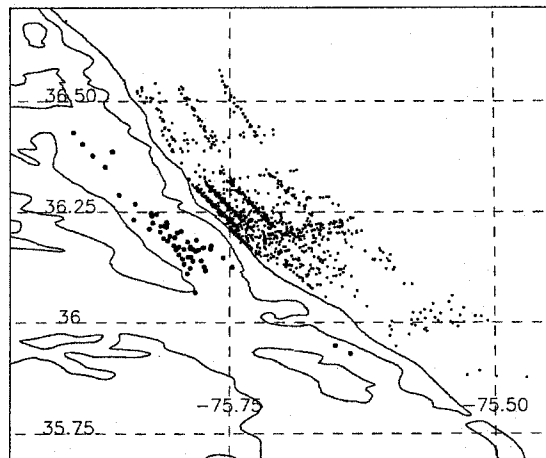


Figure 2-8: Locations of all individual inland (larger symbols) and coastal aircraft measurements. Map extent is roughly 100 x 50 km.

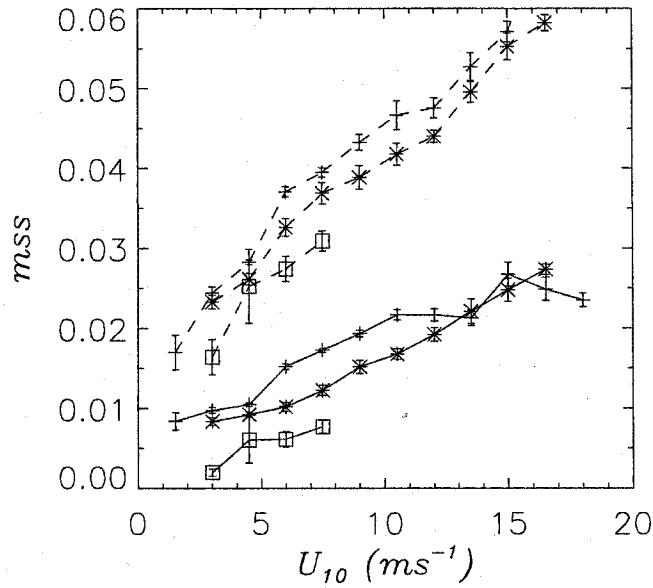


Figure 2-9: Laser- and radar-derived mss versus U_{10} for the prescribed inland (box), coastal (*), and open ocean (+) regions. The lower three curves represent mss_l , the upper curves mss'_{Ka} . Error bars depict b_{err} as defined in text.

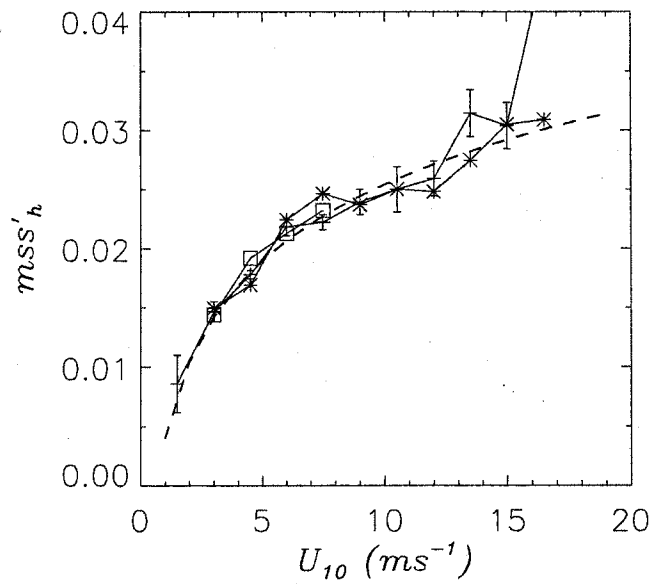


Figure 2-10: Inferred short-wave term mss'_h versus U_{10} for the prescribed inland (box), coastal (*), and open ocean (+) regions. The dashed curve represents eq. 2.11, a fit through these data.

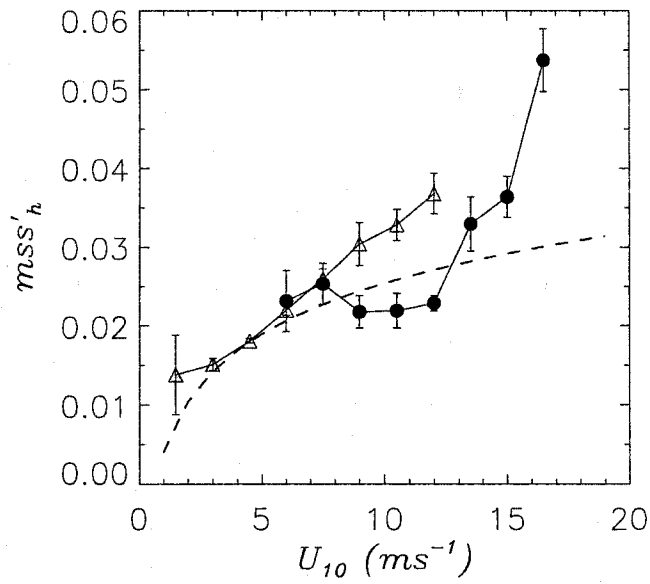


Figure 2-11: Inferred short-wave term mss_h versus U_{10} for the ensemble over estimates having $mss_l = 0.012 \pm 2.e-3$ (Δ) and $mss_l = 0.024 \pm 2.e-3$ (\bullet). The dashed curve represents the fit given by eq. 2.11. Estimates include both open and coastal ocean observations.

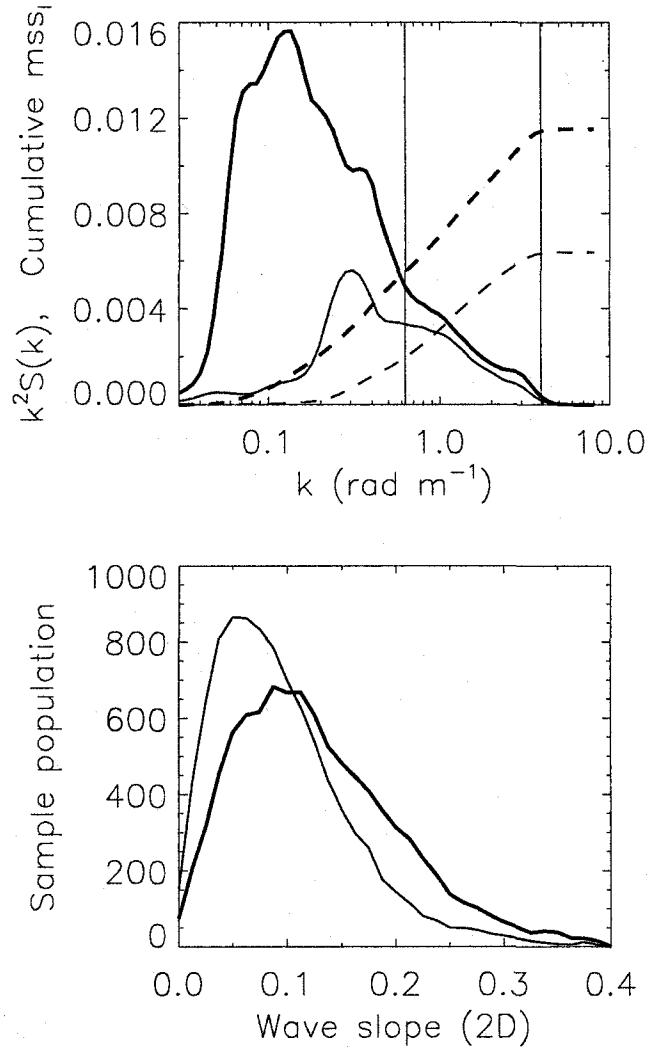


Figure 2-12: Measured wave slope data for two separate cases where $U_{10}=8 \text{ ms}^{-1}$. Thick curves represent the case of $H_s = 2.1 \text{ m}$ and $mss_l = 0.024$. Thin curves are for $H_s = 0.8 \text{ m}$ and $mss_l = 0.014$. Upper panel provides alongwind (x axis) transect slope spectra ($k_x^2 S(k_x)$) and cumulative mss_l estimates (dashed curves) as derived from a single laser's wave elevation estimates along the flight track. Vertical lines are high wavenumber cutoff values for typical buoy or wave model data (to the left) and the present aircraft data (right). The lower panel shows corresponding laser-derived omnidirectional slope probability density functions.

Chapter 3

Examining wind stress and wind waves in the presence of swell

A case study of the air-sea drag coefficient as measured off the coast of North Carolina using a low-flying aircraft suggests that the presence of following wind swell was associated with low drag values. Shorter wave slope variance at the m and cm-scale was also depressed for these moderate wind cases. The results here are not conclusive but are consistent with recent results showing some impact of the swell and that following-wind swell is associated with the lowest drag coefficient levels.

3.1 Background

The questions of how wind and ocean waves interact and how this coupling should be parameterized to optimally derive the surface wind stress remain open and central to estimating air-sea coupling at the global and local scales. While much attention has been given to evaluating the effect of the wind-driven waves upon the surface wind stress and air-sea drag coefficient, less emphasis has been given to the more common and more complex mixed sea case. At any given instant, much of the global oceans wave energy is carried in its swell fields. In fact, the majority of long wave spectra over the seas will exhibit a mixture of locally coupled wind waves and swell that is aligned in some arbitrary fashion with respect to the local wind direction. Recent work (Larsen et al., 2004; Smedman et al., 2003b; Rutgersson et al., 2001; Kudryavtsev and Makin, 2004; Drennan et al., 1999) suggests that the swell can and does act to alter the sea drag at light-to-moderate wind conditions. The swell phase speed and direction with respect to the wind vector, the steepness of the swell,

and the relative energy of the swell versus the sea are all discussed as factors in this influence. Theoretical work (Kudryavtsev and Makin, 2004) suggests that swell exchanges energy through two mechanisms: the correlation of pressure and wave slope (form drag), and the work of surface turbulent stress against the swell orbital velocity. Observation and theory suggest that it is the case of wind-opposed swell that provides the most substantial increase in the 10 m drag coefficient. An additional point of consideration is the possibility that the wave-induced momentum flux can systematically alter the assumed logarithmic form for the wind profile, perhaps calling into question the use or derivation of a 10 m drag coefficient in some cases.

A goal of the present paper is to provide some additional observations for consideration. In particular, the focus will be upon cases where there is a severe drop in the drag coefficient that occurs in conditions of stable boundary conditions and relatively strong swell fields. Data come from Office of Naval Researchs Shoaling Waves Experiment (SHOWEX). The primary measurements to be discussed were obtained using a low-flying aircraft that collected both atmospheric and wave field measurements. Another point of interest is to see when observed variability in the drag and short wave statistics covary. This emphasis is driven by the need to use short-wave remote sensing techniques to derive the wind stress information from satellites.

3.2 Methods

Measurements to be discussed were collected over the western Atlantic within 120 km of Duck NC. All flights occurred between 1997 and 1999, with most data collected in the month of November. Data come from 36 separate flights of the NOAA LongEZ covering a variety of wind and wave conditions. A map of the region, aircraft measurement and buoy locations are shown in Fig. 2-3. For all data presented herein the aircraft flew at an average altitude of 15 m above the surface. This is a unique vantage point that permits high resolution and high fidelity sensing of the sea surface and air above, much as for a fixed experimental platform. Several recent publications discuss the data products, their derivation, and processing (French et al., 2000; Sun et al., 2001; Vandemark et al., 2001). Only limited details are discussed below.

The aircraft data set used here consists of the friction velocity (u_*), bulk Richardson number (Ri), air and sea temperatures, wind velocity scaled to neutral-stability 10 m using the Toga-Coare bulk flux algorithm (U_{10N}), wind direction, significant wave height (H_s), mean square slope (mss), mean square slope of low frequency waves (mssl) and mean square slope of high frequency waves (mssh). The wave data are derived through a combination of laser altimeter and nadir-looking radar scatterometer measurements (Vandemark et al., 2001). Low and high frequency limits pertaining to mss are defined as 0.0 to 1.0 Hz for the low regime and 1 to 8 Hz for the high. Slope variance for this low frequency estimate is derived directly from the laser altimeter wave elevation and slope data. Normalized radar cross section data at Ka-band are used to extract mss . The high frequency mss estimate is obtained as $mssh = mss - mssl$. The friction velocity is derived using the eddy correlation method on the 50 Hz wind velocity component data (u, v, w) collected by the LongEZ. All variables are discussed and validated in the cited works. The processing of the data for the present study involved computing an average value along each successive 15 km ground track in the data set. Only data segments that lie beyond 15 km offshore in cases of offshore flow, or 5 km offshore for onshore flow, are used. This selection is used to provide data that is representative of open ocean conditions in this region.

Buoy data are also used in this study. First is the National Data Buoy Center's directional wave buoy N44014, located about 100 km to the east of Duck NC. This buoy was over flown frequently in 1998. Second are the University of Miami's Air-Sea Interaction System (ASIS) buoys that were located about the SHOWEX site in November of 1999. These buoys were used to validate the wind, wave height and flux data from the LongEZ. For this study we are using them to provide directional long wave information. In particular, we use the observed wave phase speed (c), direction, and rms elevation for both the wind sea and the swell modes.

3.3 Results

Several statements about the general characteristics of the sea drag observed in this open ocean data set can be made. First, the averaged 10 m drag coefficient data, $C_d = \frac{u_*^2}{U_{10N}^2}$, agree quite well with the model of (Oost et al., 2002) developed for the North Sea. This

is shown in Fig. 3-1. The total size of the data here is 665 samples. The model requires the wind speed, wave height and phase speed of the dominant wave mode and these are provided for each of our observations and averaged versus wind speed bins to create the model line presented. The error bars provide a 95 % confidence interval assuming random error in each wind speed bin. As one can see the present observations lie well above the model in the light wind regime but for moderate winds the two results are nearly identical. The model was derived in the North Sea and perhaps similar wave climates and coastal proximity serve to aid this agreement. But the model's incorporation of wave impacts may also be bridging the gap between the two observational data sets to provide a viable model for the drag at moderate winds.

Second, the light wind data in this set should be treated with caution. Knowledge of the vertical structure of the boundary layer can become quite important in this case and most of the data examined here are acquired at only one nominal altitude above the surface, usually 15 m. Profile uncertainties in both deriving the friction velocity and in understanding the actual depths and characteristics of the inner and outer boundary layer regions in this case point our focus towards the moderate wind speed range.

Third, one particularly distinguishing characteristic of the data set is the occurrence of anomalously low C_d values on several of the measurement days where the wind speed at altitude registered a moderate level of 4-7 ms⁻¹. We view these as cases of smooth flow. Upon inspection, these days were typically associated with a relatively stable boundary layer. They are also characterized as cases where the wind and swell directions were within 60 degrees of each other and the swell amplitude exceeds that of the sea by a substantial level.

Another distinguishing feature for these smooth flow cases is seen when one examines the aircraft's wave slope variance and wind data. It is well known that the short waves generally respond well to local wind variations and this fact was well represented in the present data set. In our data set such a relationship was typically evident but a much different observation is observed for the smooth flow cases. A general lack of correspondence between the wind and mss was a common feature for these events.

Fig. 3-2 and Table 3.1 provide some detail for the low drag coefficient events that

constitute smooth flow cases in our data set. In Fig. 3-2(a) we reproduce the sea drag results for the overall experiment (Fig. 3-1) along with the low level drag observations. It is evident that for these cases the level drops 60-70% variance relationships for the experiment (upper curves on each panel) as well as the mss vs. wind speed relationship for the smooth flow events only. It is apparent the surface wave roughness is lower for the low drag events as the wind speed increases. This is seen for total, low, and high frequency mss estimates. The relative depression in roughness is largest for the high frequency waves, mssh, but the relative decrease from the nominal level is not as large as that for C_d .

While it is known that the drag coefficient, and similarly the roughness length, z_o , can depend on numerous factors, the strong depression of the drag coefficient is not found in any usual parameterization that depends for example upon the atmospheric stability, or the sea state (e.g. via inverse wave age ($\frac{u_*}{c}$) and/or wave height). Each of these factors is, in fact, contained within the model of Oost et al. (2002) and others. Upon consideration of the stable flow regimes and the swell we suggest the cases accord most closely with the condition of ultra-smooth flow (Donelan, 1990). The results are akin to that seen in the Baltic (Smedman et al., 2003b; Rutgersson et al., 2001) where investigations of swell in stable, neutral, and unstable boundary layer conditions have been made. The latter paper examines near neutral data and discusses the fact that in mixed seas the sea drag may need to be examined both as a function of the wave age and of the relative wave spectral energy (E) contributions of the sea and the swell. That paper defines the condition of $E_{swell} : E_{sea} > 4$ as being swell dominated. The data for the cases of Table 1 and for (Smedman et al., 2003b) are given in Fig. 3-3. To create these results from Table 1 we adjusted the swell phase velocity by the cosine of the angle with respect to the wind when computing the inverse wave age.

The present results and those of Smedman et al. in Fig. 3-3 all represent cases of very old waves. The direction of the swell was not available from that study but there are two estimates in their Fig. 12 at old seas where the drag exceeded 1.0×10^{-3} in that work and where directionality (e.g. opposing-wind swell) may be an issue.

Regardless, the data sets shown here do follow a similar course. Present results off the North Carolina coast suggest that the swell is coupling with the atmosphere with a resulting decrease in the drag.

3.4 Summary

Field observations are presented that provide some further support for the effects of swell on the 10 m air-sea drag coefficient. The investigation here is preliminary and focused on cases where the drag coefficient dropped to very low levels at moderate wind speeds. Preliminary results indicate the drag depression is occurring when the swell travels nearly in a following-wind direction. The short wave steepness in both the intermediate and cm-scale was reduced for these cases but not with the magnitude seen in the drag.

Some common obstacles to further clarification are being addressed. These include self-correlation, isolation of atmospheric stability effects, and perhaps most importantly understanding the influence of the vertical profile on the observed drag and on the inferences that can be drawn using the single level aircraft data for the limited cases presented. The recent studies cited (e.g. Smedman et al., 2003b; Kudryavtsev and Makin, 2004) indicate that the inner (wave) and outer boundary layer structure may be quite different for the case of swell dominance as opposed to well- couple wind waves. Further examination of the aircraft wind and wave cospectra should aid in this effort.

Table 3.1: Average results for the low C_d cases.

Variable	19981110	19981116	19981122	19991126
Samples	19	17	9	27
u_*	0.12	0.06	0.10	0.12
Direction (deg.)				
Wind	113	113	50	156
Sea	85	65	49	168
Swell	75	122	120	125
Speed (ms^{-1})				
U_{10N}	6.3	4.4	4.7	5.7
Sea	5.5	6.2	4.9	4.6
Swell	13.1	14.1	14.6	11.4
Swell:Sea (energy ratio)	7.8	3.3	37.1	16.8
H_s (m)	0.8	0.8	1.6	1.8
Air-sea(degC)	1.6	-0.98	1.5	5.39
Rich. Number	0.02	-0.03	0.02	0.06

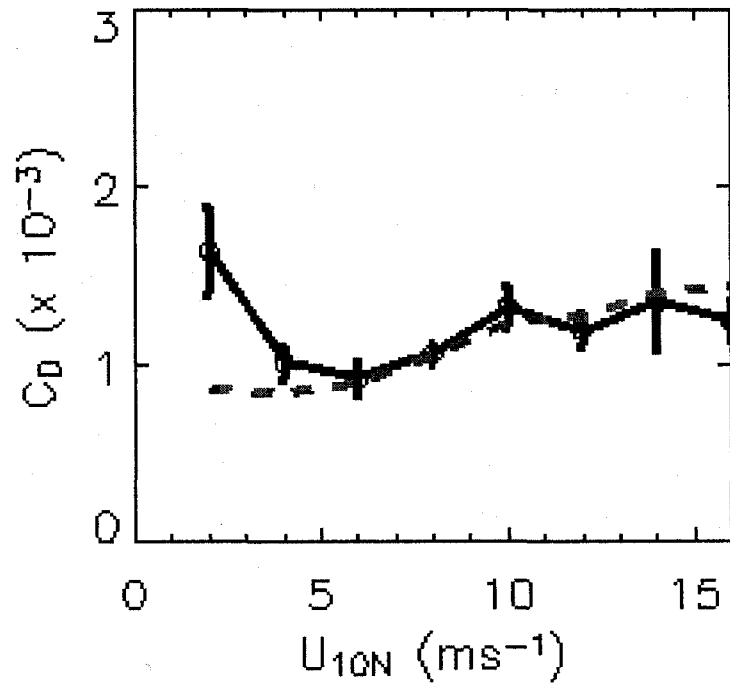


Figure 3-1: Observed air-sea drag coefficient obtained versus wind speed (averaged across 2 ms^{-1} wind speed bins) for this study with 95 confidence intervals. Dashed line is the model of Oost et al. (2002).

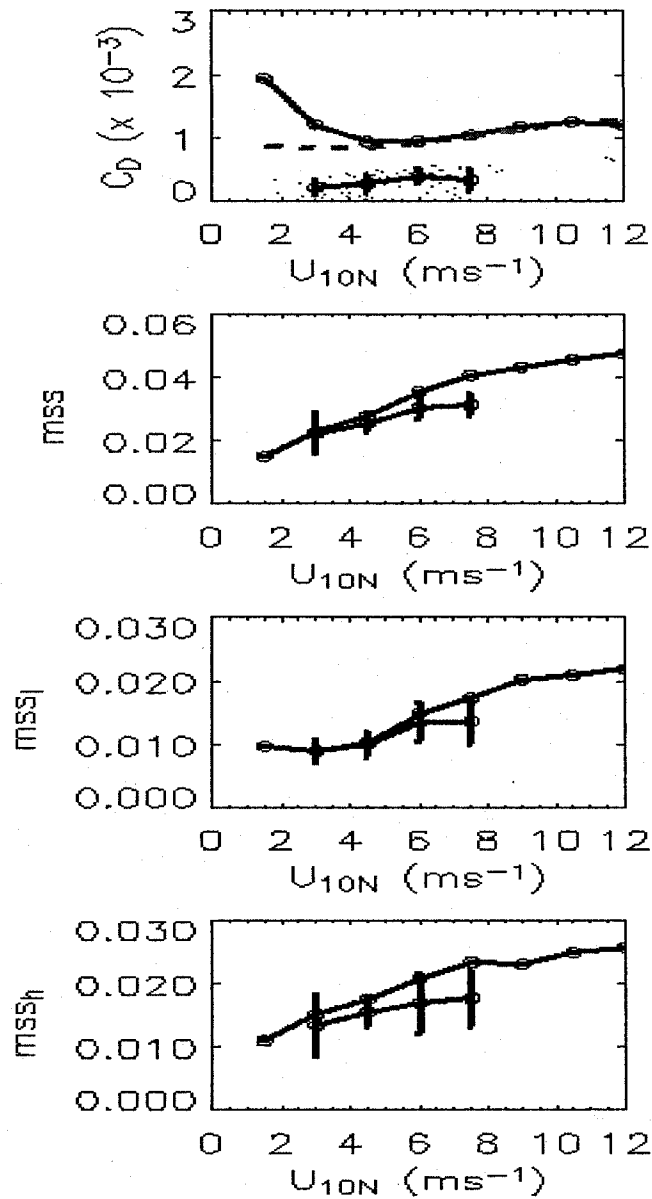


Figure 3-2: Figure 3 is wind dependence for the 10 m drag coefficient and slope variance estimates. In all cases the upper solid trace is for the overall data set and the lower trace (with error bars) is for the smooth flow cases denoted in Table 1. Dashed line is Oost et al. (2002).

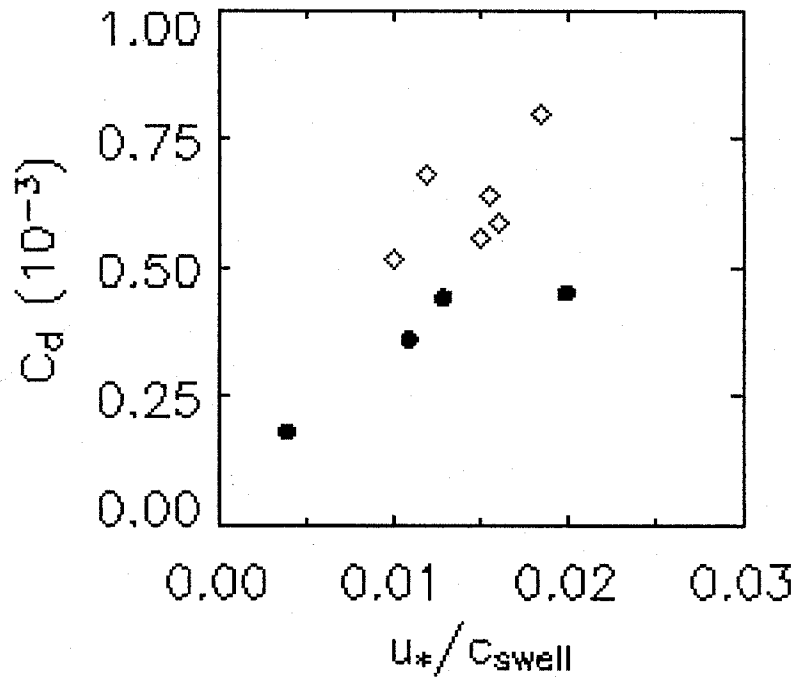


Figure 3-3: Figure 4 is drag levels (*) for aircraft results of Fig. 4 and Tab. 1 as given for each of the four days in the Tab. 1. Diamonds are taken from Fig. 12 of (Smedman et al., 2003b) for swell-dominated cases with C_d less than 0.01.

Chapter 4

Impact of high frequency waves in the ocean altimeter range bias

New aircraft observations are presented related to the range determination error in satellite altimetry associated with ocean waves. For the first time, the measured cross correlation between the gravity wave slope and elevation is reported. This is obtained using a cm-precision laser altimeter array with 1 m horizontal spacing. Observations of this so-called cross skewness or tilt bias term, as well as the elevation skewness, provide direct measurement of statistics central to the weakly nonlinear gravity wave theory invoked in altimeter sea state bias modeling efforts. Coincident Ka-band radar scattering data are used to simultaneously estimate a range bias more aligned with to that from a satellite altimeter. These data, along with ancillary wind and wave slope variance estimates, are used to examine aspects of published theory on controls for this phenomenon. The tilt bias is confirmed to be a significant component of the total electromagnetic (EM) bias. Moreover, to first order, the term is observed to be linearly related to wind speed and with the slope variance associated with gravity waves. The radar-observed range shift associated with interactions between long and short waves is addressed under the assumption that the effect is additive to the long wave tilt bias term. This residual term is also a substantial part of the EM bias and is observed to be linear in wind speed or wave slope up to $7-8 \text{ ms}^{-1}$ where this factor dominates the EM bias. It then shows a decreased magnitude for strong wind or high slope variance. This behavior is consistent with EM bias prediction based in hydrodynamic modulation theory. Observed spatial variation in the range bias under fetch-limited conditions provides just one example of remaining complexity not directly associated with these correlatives.

4.1 Background

The term electromagnetic bias refers to the observed height difference between true mean sea level and that inferred using a radar altimeter. In simplest terms, this EM bias occurs because the reflection of radar signal from wave troughs is greater than that from the crests. Field study observations (Yaplee et al., 1971; Walsh et al., 1984; Arnold et al., 1995) and satellite-based work (cf. Chelton et al., 2001) have shown that the bias exists, has a radar frequency dependence and is, to first-order, related to the sea state. To date, the operational satellite correction uses empirical methods and ancillary satellite measurements of H_s and wind speed to estimate this bias for each spacecraft range estimate along its groundtrack. Still there remains a need to improve this sea level correction as its uncertainty, of $O(1\%$ of H_s), now looms large as other terms in the error budget are reduced. Moreover, there is a need to understand when a systematic temporal or spatial error in this correction is occurring (Kumar et al., 2003; Chelton et al., 2001). In other words, a fundamental need in sea state bias research is to understand when and why the bias varies.

This task has proven difficult to accomplish. The EM bias is associated with nonlinear wave and radar scattering processes that require exacting measurement to resolve and which are seldom recorded. It is also recognized that satellite sensor-specific issues such as the range tracking method, and range corrections as varied as the barotropic, ionospheric, and dual-frequency terms, make direct intercomparison of field, theory, and satellite bias results difficult. Several approaches in theory and field experiments have been used to assess the magnitude and variability of the nondimensional EM bias term, β , where the absolute bias is written as

$$bias(m) = \beta * H_s \quad (4.1)$$

and where H_s is the significant wave height, defined as 4 times the wave elevation standard deviation.

Empirical field studies show a progression from parameterizing β in terms of wind speed and wave height (Walsh et al., 1984, 1991; Melville et al., 1991; Hevizi et al., 1993; Arnold et al., 1995) to the most recent correlative being the rms slope of longer waves (Millet et al.,

2003; Melville et al., 2004). Thus the field observations now suggest that one needs to understand variability in the gravity wave slope variance, a variable not readily retrieved from a satellite.

Theory is divided into several schools. The first shows that a bias can be predicted using weakly nonlinear theory (WNL) (Longuet-Higgins, 1963) where three wave interactions among longer gravity waves lead to β estimates of order 2-8% (e.g. Jackson, 1979; Srokosz, 1986; Glazman et al., 1996; Gommenginger et al., 2003). The predicted bias is primarily due to a so called tilt bias or cross-skewness term that arises due to a nonzero cross-correlation between the long wave wave elevation and slope. An extension of this theory includes the geometric or tilt modulation of small ocean surface patches by the underlying wave field (Rodriguez et al., 1992; Elfouhaily et al., 2000). This model invokes the two-scale hypothesis that short and long waves can be geometrically separated. One result is that the short-scale waves act to attenuate WNL predictions made when neglecting their presence. A separate modeling approach (Rodriguez et al., 1992; Elfouhaily et al., 2001a) addresses the hypothesis that hydrodynamic modulations, modeled using the conservation of wave action, act to strain cm to m scale waves along the phase, and elevation, of the underlying long waves. This modeled interaction between long and short waves is fundamentally linked to the long wave orbital velocity and represents a process quite distinct from WNL theory (cf. Elfouhaily et al., 2001a; Chapron et al., 2001).

These theories have requisite assumptions and ranges of validity and, not surprisingly, enough uncertainty to preclude anything beyond order of magnitude in agreement with observations. This is largely because there is insufficient observational information on the space and time characteristics of the nonlinear sea surface at the wave scales that involve the sea state bias. Moreover, it is likely that both controls are present in the real surface yet little field work has been done to assess how these coexisting processes combine to impact sea state bias variability. To illustrate this point, Gommenginger et al. (2003) exclusively invokes WNL theory to semi-empirically tie the bias to rms slope while Melville et al. (2004) uses a "surrogate" hydrodynamic modulation to do the same. Moreover, the observed radar-frequency dependence of the range bias in past data sets can be predicted using several mechanisms (Rodriguez et al., 1992; Elfouhaily et al., 2000, 2001a).

Some fundamental questions can be distilled pertaining to improved understanding of

the controls on the sea state bias. What is the magnitude of the longer wave cross-skewness bias? Is there evidence to support that both this WNL term and long-wave short-wave interactions are involved in the net observed range bias? Which wind and wave observations correlate with these bias components and under what conditions?

To address these questions we present new aircraft data where long wave statistics and radar measurements were made in concert. This paper provides observations of the EM bias at Ka-band. We also provide a measure of the cross-skewness, or tilt bias term. This is the first time that tilt bias data have been presented. Its quantitative measure permits an opportunity to address the relative importance of the longer wave nonlinear geometry versus hydrodynamic short-wave modulation in sea state bias control.

4.2 Methods

All observations in this study come from an aircraft data collection effort utilizing the National Oceanic and Atmospheric Administration LongEZ research aircraft. The flights took place from 1997-1999, mostly in the month of November. Work in 1997 and 1999 was part of the Office of Naval Research Shoaling Waves Experiment while 1998 data come from NASA's Wave Profile Experiment. All data shown herein were collected off the coast of North Carolina over the mid-Atlantic Bight. The composite data set covers 36 separate flights and more than 2700 individual sea state bias estimates enfolding a spatial ground track of more than 12,000 km. Estimates acquired within 15 km of the coast (depth $\lesssim 20$ m) are omitted to maintain open-ocean conditions. A map of the region and the location of data points can be seen in Fig. 3 of Vandemark et al. (2004c). The conditions encountered included wind speeds up to 20 m/s and wave heights up to 3.5 m. For more detailed information on the measurement platform and overall experiment details the reader is referred to several recent studies (Vandemark et al., 2001; Sun et al., 2001; Vandemark et al., 2004c).

The aircraft measurements that are central to this study are those from a Ka-band scatterometer pointed vertically toward the ocean and three cm-precision laser altimeters spaced 0.95 m apart on the airframe and also directed vertically downward to measure the surface elevation at three points surrounding the 1 m diameter radar footprint (see Fig.3

(Vandemark et al., 2001)). Specifics of this system and its calibration, motion correction, and data filtering have been described elsewhere (Vandemark et al., 2001; Sun et al., 2001; Vandemark et al., 2004c, 1999).

The laser system's three wave elevation estimates are used to infer triply redundant wave elevations (ζ) and wave slopes over 0.95 m spans in orthogonal directions (ζ_x, ζ_y) with respect to the aircraft's heading (along and across the flight track). From these measures it is straightforward to compute parameters relevant to the sea state bias as formulated under weakly nonlinear theory (e.g. Srokosz, 1986):

$$bias_{WNL} = -\frac{1}{8} \left(\frac{1}{3}\lambda_0 + \lambda_1 \right) H_s \quad (4.2)$$

where $\lambda_0 = \frac{\langle \zeta^3 \rangle}{\langle \zeta^2 \rangle^{3/2}}$ is the elevation skewness and $\lambda_1 = \frac{\langle \zeta \zeta_x^2 \rangle}{\langle \zeta^2 \rangle^{1/2} \langle \zeta_x^2 \rangle} + \frac{\langle \zeta \zeta_y^2 \rangle}{\langle \zeta^2 \rangle^{1/2} \langle \zeta_y^2 \rangle}$ is a "cross-skewness" term where here we have neglected the slope-slope terms under the assumption of isotropic wave slope (Vandemark et al., 2004c). The ability to directly measure λ_1 is a primary contribution of this study. This cross correlation between the slope variance and the height is quite easily interpreted as being the electromagnetic range bias (or the specular height (Glazman et al., 1996)) that one would observe for a filtered surface having no waves of length scale less than 1-2 m. The direct determination without recourse to a spectral model or theory provides a valuable means to assess the predictions made by many using the WNL formulation of eq. 4.2. The data processing used in this study computes these terms as $bias_{WNL} = \beta_{WNL} H_s = (\beta_s + \beta_t) H_s$ over each 5 km flight segment using roughly 5000 individual slope and elevation measurements. Our computed cross-skewness term, typically seen in the literature as λ_{12} , will be denoted as the tilt bias (β_t) and it should be noted that this bias is associated with the slope variances for waves of length 1-2 m and longer. The skewness bias is denoted as β_s . This term is not strictly associated with the EM bias. The EM bias is the difference between the mean scattering level seen using a radar and true mean sea level while the elevation skewness bias is the height difference between the mean scattering surface and the median (cf. Chelton et al., 2001). In this paper we will report observed β_s and use it in comparisons with the sea state bias predicted using WNL under eq. 4.2. When EM bias and radar measurements are discussed they exclude β_s .

The analog to the longer wave slope and elevation cross correlation (β_t) defines the radar

electromagnetic bias where the normalized radar cross section (σ^o) takes the place of the slope variance and the relative bias is then:

$$\beta_{Ka} = \frac{\langle \zeta \sigma^o \rangle}{\langle \sigma^o \rangle} H_s^{-1} \quad (4.3)$$

A Ka-band radar with radiation wavelength of 0.83 cm was used in this experiment primarily because of the aircraft's small size and low flight altitude. This frequency resides above the typical Ku-band (2.14 cm) satellite altimeter wavelength, but present observations should have value for several reasons. First, the difference in wavelength is quite small, and though the surface slope and curvature spectra are known to have potentially strong differences at these cm scales, one should be able to relate the results at these two frequencies with some confidence. Second, previous results at Ka-band (e.g. Walsh et al., 1984, 1991) suggest the Ka-band bias is significantly lower than that at Ku- or C-band. This result can be assessed here. Finally, future micro-altimeter concepts are in the works using Ka-band designs. EM bias data at Ka-band are thus of great interest in these developments. As with the tilt bias, each β_{Ka} estimate is obtained over a 5 km flight segment.

To make further use of the combined radar, tilt, and skewness bias measurements we can take the additional step of extracting a residual bias under the assumption of a two-scale surface model where the concept divides the surface between nearly linear fast-traveling long waves and short waves, roughly waves with k greater than 10 times the peak spectral wavenumber. This conceptual model serves several purposes (see Rodriguez et al., 1992; Elfouhaily et al., 2000, 2001a; Chapron et al., 2001). First, it is a prerequisite under hydrodynamic and aerodynamic modulation theories where the shorter waves are modulated along the phase of the longer of the longer waves. Second, the scale break is also useful in addressing the typical EM bias field measurements (Walsh et al., 1991; Arnold et al., 1995; Melville et al., 2004) where the radar footprint is of the order of 1 m. In this case, one can independently address the effects of roughness elements within this 1 m facet and the radar scattering from that roughened patch as it tilts due to linear and nonlinear long wave effects. Third, Elfouhaily et al. (2000) pointed out that weakly nonlinear theory should not be extended down to the short cm-scale waves that dominate a radar's σ^o measurement. A break in the spectrum near 1-10 m is one suggestion to avoid violation of the theory's assumptions. The scale break for each of the issues mentioned above are discussed in the noted studies, but the 1-2 m separation scale inherent in the present paper's laser and radar

observations is reasonably consistent with that suggested for each of these issues.

Two factors discussed in these modeling efforts will be used in the evaluation of our combined sea state bias data. Both Rodriguez et al. (1992) and Elfouhaily et al. (2000) address the fact that under geometric optics assumption the effective radar, or filtered-surface electromagnetic bias, will be measurably lower than that predicted under geometrically-dictated WNL theory range bias. This arises because the short wave roughness atop these tilted 1 m facets acts to diffuse the radar scattering which effectively attenuates the nonlinearity in elevation-radar cross correlation estimate. This is also known as the effect one ignores if one invokes the 'horizontal or specular-facet assumption' (e.g. Jackson et al., 1992). An analytical formulation for this attenuated tilt bias (β_{ta}) is proposed (Elfouhaily et al., 2000) that, to first-order, is given as:

$$\beta_{ta} = \lambda_{12} \Delta \quad (4.4)$$

where Δ is the ratio of the long-wave (or low frequency) slope variance (mss_l) to the total, $\Delta = \frac{mss_l}{mss_l + mss_s}$. This term is readily computed using the measurements in our field study where the denominator is the total mean square slope for the Ka-band radar, mss (see Vandemark et al., 2004c). The scale break between the long and short waves is 1-2 m. Therefore β_{ta} pertains to the electromagnetic bias seen under the assumptions of weakly nonlinear theory and geometric optics radar scattering down to filtered surface of roughly three times the radar wavelength, or about 25 mm.

The second modeling component that we make use of is to assume that long-wave short-wave interactions may also play a role in the radar EM bias observations. For example, hydrodynamic modulation can be imposed atop a nonlinear or linear gravity wave field such that a Ka-band radar relative sea state bias can be written as $\beta_{Ka} = \beta_{ta} + \beta_{hydro}$. Two efforts have invoked this process to address β_{hydro} for Ku- and C-band EM bias radar predictions (Rodriguez et al., 1992; Elfouhaily et al., 2001a). Another process discussed in this context is the potential role of wave breaking where an elevation dependence in the short wave roughness for intermediate scale waves of order 20-30 cm is predicted (e.g. Kudryavtsev et al., 1999; Chapron et al., 2001).

Combining these model-based factors and our observations we arrive to a residual bias term:

$$\beta_{res} = \beta_{Ka} - \beta_{ta} \quad (4.5)$$

where variables on the right hand side are derived from measurements discussed above. This term will be examined in the discussion section to explore the agreement between observations and predictions regarding long and short wave interactions and the EM bias.

Ancillary data used in this study come primarily from coincident aircraft measurements. These include neutral stability wind speed and friction velocity estimates as well as slope statistics such as the slope variance, skewness, and kurtosis (Vandemark et al., 2004c, 2001; Sun et al., 2001). The slope data at both long and short wavelengths are discussed in Vandemark et al. (2004c). In keeping with recent EM bias work that parameterizes the relative bias in terms of rms slope we derive a slope term, s , that accords with the root mean square of the slope variance for a wavelength cutoff of 10 m. This is obtained by scaling our 2 m slope variance, ms_{sl} , by a factor of 0.4 and then taking the square root. The scaling factor was obtained by calibration against wave buoys and wave model spectra (Gourrion et al., 2002a). This 10 m cutoff corresponds both to a typical wave buoy high frequency cutoff ($f_c \sim 0.4Hz$) and also to the recent EM bias work of Melville et al. (2004) (see their Fig. 4.). It should be noted that while the slope variance is known to have a nearly 1:1 correspondence with the wind speed, the rms of this value will necessarily differ somewhat. The effect of taking the square root is to alter the probability density function for the observed slopes from a Rayleigh distribution to that of a Gaussian. In essence both high and low slope (wind speed) values are compressed toward the distribution mean. One effect in this case is compression of the dynamic range of the regressor.

One limitation of the aircraft laser altimeter system is inability to cleanly resolve the long wave directional spectrum without a priori knowledge of wave propagation directions (Sun et al., 2003). This is mainly a limitation due to aircraft encounter speed with respect to the moving sea surface. One result is our inability to resolve the phase speed of the dominant wave, and hence the wave age or significant slope. Several directional wave measuring buoys were overflown during the course of the data collection and their spectral output can be used for this purpose in a limited sense.

4.3 Results

Calculated biases and selected ancillary data are shown for the whole experimental data set in Fig. 4-1. The data sample abscissa for the figure simply represents a discontinuous record of all the flight data over the 36 days. One can see the absolute bias for the radar and cross-skewness (tilt bias) track well with each other and with the wind speed, slope variance, and wave height. All variables appear highly correlated. The magnitude of the radar exceeds that derived from the laser slope in most cases, but often by only a small percentage. Clearly the tilt bias is substantial component on its own, suggesting that the longer wave bias is certainly of the order of magnitude of the radar-derived value.

4.3.1 Long wave range biases

The relative bias for cross-skewness and skewness terms (β_s and β_t) are shown in Figs. 4-2 and 4-3. The data have been averaged with the respective regressors. The rms slope is used in the following presentations to permit evaluations consistent with recent work in this field (Gommenginger et al., 2003; Melville et al., 2004; Millet et al., 2003).

It is apparent that the skewness bias is quite small and invariant with the wind. The average observed elevation skewness was 0.09 with a standard deviation of 0.14 and this translates through eq. 4.2 to the levels shown in Fig. 4-2. It is also apparent that β_t is linear with the wind speed for winds above 4 ms^{-1} , and is also linearly increasing with the rms slope. The sensitivity of the bias to the rms slope over the range of all data falls below that of the wind speed; one sees a maximum of 3.2 % for highest wind the maximum reached is 2.2 % for the highest slope. As stated before, these are the first measurements of this kind in the literature.

The linear fits given in Figs. 4-2 and 4-3 follow.

$$\beta_t (\%H_s) = 0.51 + 0.15 * U_{10N} \text{ [for } * U_{10N} > 4\text{ms}^{-1}] \quad (4.6)$$

and

$$\beta_t (\%H_s) = -0.40 + 26.0 * s \quad (4.7)$$

4.3.2 Ka-band EM bias

The relative bias, β_{Ka} , for the radar is shown in Figs. 4-4 and 4-5. Similar behavior versus the abscissa is seen for both the wind and slope figures. A bias near 1.0 % is seen for the lowest values, a linear rise up to a near maximum value and then a levelling off or slight decrease with increased wind or slope. This quadratic type of behavior has been seen in previous studies at Ku and C-band as well. In fact these data agree quite well with the Ku-band tower results (e.g. Arnold et al., 1995). The mean level is above 3 % for wind speeds exceeding 6 ms^{-1} . Data from Walsh et al. (1991) are supplied for comparison and one can see that the present results are of the order of 2 % greater than these previous measurements. A local maximum is observed in that data as well but with the limit of 5 data points a linear fit was certainly justified. As noted, the results when compared against the rms slope of Fig. 4-5 show a similar relationship, and sensitivity across the range of data, to that seen with the wind speed. The data do not tend to 0.0 in either figure. Quadratic fits are applied to both results with limited success as the data do not precisely conform to this assumption. A better description might be a piecewise linear model with a hinge point at the local maximum that resides at 8 ms^{-1} in wind speed or 0.08 in the rms slope.

These data were also regressed against the mss_i and friction velocity measurements and behavior very similar to that seen in Fig. 4-4 is observed. The local maximum for friction velocity was found to occur near 0.23 ms^{-1} .

The quadratic fits given in Figs. 4-4 and 4-5 follow.

$$\beta_t (\%H_s) = 0.84 + 0.37 * U_{10N} - 0.013 * U_{10N}^2 \quad (4.8)$$

and

$$\beta_t (\%H_s) = -0.93 + 73.5 * s - 321.0 * s^2 \quad (4.9)$$

The observed data scatter for a given wind speed indicates a standard deviation of the order of 2 %. Similar deviation magnitudes are seen versus the slope abscissa. The deviations observed here exceed the scatter seen in recently published tower data (Millet et al., 2003; Melville et al., 2004) from the 1990 and 1994 Gulf of Mexico and Bass Straits experiments. Those results represent platform data averaged over a one hour time period. Our 5 km spatial data segments, a length dictated by the observed spatial variability in

the wave and wind fields, will likely lead to more intrinsic noise in individual bias estimates as 5 km in space translates roughly to 10 minutes in a temporal estimate. Still, closer examination of the present data set does indicate that some of the observed variability at a fixed wind speed is geophysical.

4.3.3 An example of spatial complexity

To provide some indication of the variability within this data set we present one example case where the wind-wave conditions can be characterized as reasonably close to fetch-limited with constant wind speed. The aircraft measurements for a single flight leg along the fetch are given. The date was Nov. 15, 1998, the flight time for this leg ran from 1540 to 1635 UTC. Winds were from the west/southwest at about $8-10 \text{ ms}^{-1}$ for the past 12 hours and the speed was weakening at flight time. At the time of the flight the winds were from 290 degrees. Fig. 4-6 shows data as collected from the shore out to more than 200 km to the east on an aircraft heading of 75 degrees. NDBC buoy 44014 was flown over at about 1600 UTC 90 km from shore. At this time the buoy spectra showed a wind sea tail at 270 degrees, but a turning spectrum with the peak sea direction at 240 deg. and a frequency of 0.18 Hz. A weak swell from the NE was also present. Panel b and c show the wave height, slope variance and friction velocity, u_* . The wind speed, not shown, tracks with u_* and had values of 6.5 to 8 ms^{-1} . Panel b shows the wave height and slope increasing with fetch. To gauge how well this fit a fetch-limited situation the wave spectrum model of Elfouhaily et al. (1997) is used to estimate these parameters based on the measured wind speed and fetch. An offset of 0.3 m in H_s and 0.003 in mss , both to adjust for the known swell, were added for all fetches. Wind was adjusted by a factor of 1.1 for all fetches. The modeled results agree well with what is observed. We conclude that a fetch-limited characterization is reasonable. The model's inverse wave age for this case extends from a value of 1.9 nearest shore to about 1.15 at the farthest fetch.

The relative radar and tilt biases are shown in the top panel of Fig. 4-6. The larger levels are those for the Ka-band radar. Reference to the previous section shows the 5.5 % magnitude of the bias at a fetch of 50-80 km exceeds the nominal levels seen versus wind or slope values. Moreover, one sees a strong gradient in the radar sea state bias as one heads from shore out to sea. The radar and tilt biases are quite near each other at the shortest

fetch. Then the radar term increases rapidly in the first 20-30 km and then again to a peak at 70 km fetch. But a significant drop in β_{Ka} occurs after about 70 km and the levels fall to meet β_t at 110 km with a magnitude of 2.8 %, nearly half that only 40 km away. The levels then increase as one heads to a fetch of 180 km.

A different result is seen for β_t . This variable has a smaller magnitude and increases more or less linearly with fetch to around 120 km and then decays back to the level nearest shore. A total excursion of about 1.5 % is observed.

The ancillary data fields in our aircraft data set were explored for this flight leg to determine if other variables behaved in a similar manner. Panel d provides two parameters that may do so. The bias derived from the elevation skewness is the solid curve and it is apparent that the skewness did increase dramatically at short fetch and then continue on to a local maximum near to 50-60 km in fetch. Referring back to our earlier results on the skewness bias 4-2 one can see that the bias exceeds the mean value for a wind speed of $6-7 \text{ ms}^{-1}$. In fact a value of 0.3 in skewness was observed at 65 km fetch. As shown, the skewness then fell off to somewhat lower levels with extended fetch. The other trace on this panel d is the tilt bias associated with the cross-track slope (λ_{102}). This variable was quite low up until fetch of 90 km and then a localized increase is seen for the next 30 to 50 km, one that is inverse to the behavior seen in β_{Ka} in panel a but correlated with a slight increase in β_t in the same panel. Finally, we provide results from a diagnostic variable that is carried in the data set. The lowest panel provides the cross-correlation between the individual slope modulus (ζ_{2D}) and σ° . This average value of this term for the multi-year data set is -0.14 and the largest level is -0.36. Physically, this correlation is expected and would be -1.0 if there were only longer waves on the surface controlling all radar return power. What is seen in panel e is that this correlation increases significantly near a fetch of 100 km, perhaps in tandem with the cross-track tilt term in panel d. The local increase indicates increased reflection of the tilted facet field in the radar cross section data.

4.4 Discussion and conclusions

The most fundamental contribution of this paper is to directly measure the range bias associated with the longer waves. A linear model versus wind speed or the rms slope results.

Data versus wind speed combining skewness and cross-skewness β_{WNL} are shown in Fig. 4-7. We find that at all but light winds the observation falls significantly below numerous previous works (e.g. Jackson et al., 1992; Srokosz, 1986; Rodriguez et al., 1992; Glazman et al., 1996) involving weakly nonlinear theory. That conclusion is illustrated in Fig. 4-7 where the two dimensional WNL theory prediction is given along with the observation-based result. The theoretical long-wave result is for that portion of the wave spectrum down to 10 times the peak wavenumber. As shown in Gommenginger et al. (2003) and elsewhere, extension of this theory to include shorter waves does not substantially lower this prediction. It is seen that the magnitude of the model is a factor of 1.5-1.9 above the data. However, it is encouraging that the observations and model both show a linearly increase with wind speed. This is also found to be the case versus the long wave rms slope and slope variance (not shown).

Moreover, if one attenuates the WNL prediction in the manner described in eq. 4.4 and (Elfouhaily et al., 2000) then one finds that model and observation draw quite close in magnitude as well. In this instance, the wavelength separation scale for the slope variance ratio term Δ would be $10 k_p$ while the denominator, the total variance, would be our measured 2 m slope variance term mss_l . This ratio can be approximated by following Phillips (1977) to derive mss_{10k_p} for a fully-developed wind sea given the wind speed (see also Vandemark et al., 2004c). We find $\Delta(k_p)$ will extend from a value of 1.0 for winds up to 5 m s^{-1} and then quickly decay to a value near 0.5 for wind speeds above the low wind regime. While this is admittedly a first-order estimate lacking the true k_p , application of this Δ factor in Fig. 4-7 aligns the theory and observations to within 10-20 % for moderate to high wind speeds. We suggest that this is a fairly remarkable confirmation of the tilt bias predicted using WNL theory for wavelengths greater than 1-2 m.

So one now has some quantifiable validation of the most fundamental model for the electromagnetic bias associated with the longer waves, both in magnitude and its dependence on the wind speed. The present data should be considered as representing only a limited range of wave conditions (see Fig. 4-1), but a range that future simulations should be able to encompass.

Moreover, the results cement the knowledge that cross-skewness is, to first-order, linear in short wave roughness and/or wind speed, as well as in the longer wave slope variance.

This variable does not show the quadratic behavior, often attributed to long-wave short-wave modulations, that is seen in the radar EM bias data at C-, Ku- and now Ka-band. Elfouhaily et al. (1999) postulated that the intermediate scale waves, λ of $O(1-10\text{ m})$, may be subject to such nonlinear wave hydrodynamics. The present data on β_t suggest that if it is present, the effect certainly differs from that observed within the radar EM bias.

Turning to the radar observations, Figs. 4-4 and 4-8 suggest that the present Ka-band aircraft data agree more closely with tower observations at Ku-band than with the aircraft observations at Ka-band reported in Walsh et al. (1991). The EM bias field observation literature is limited to only a handful of measurement programs. The aircraft sensors, data collection, and analysis techniques of Walsh et al. (1991) differ substantially from those used in the LongEZ measurements collected for this study. That program also reported C- and Ku-band results (Hevizi et al., 1993) that fall substantially below tower measurement results at C- and Ku-band (Melville et al., 1991; Arnold et al., 1995; Melville et al., 2004). The present aircraft field data were collected at lower altitudes (10-25 m) and with equipment that is much more closely aligned to the tower measurement programs. The measurement discrepancy has been cited before and we do not have information to clarify the differences excepting one point. The work of the former (e.g. Walsh et al., 1991; Hevizi et al., 1993) reports the EM bias as the range difference between the computed centroid using the radar and elevation data and that using the elevation data alone. Thus their EM bias is referred to elevation median rather than the mean. This differs from the results computed here or in the tower experiments, both reporting the radar EM bias as eq. 4.3. As seen in our Fig. 4-2 this skewness factor would not be large enough to explain the reported differences but it does help lessen the gap.

Overall, the comparison of Ku- and Ka-band results shown in Fig. 4-8 suggests that the Ka value lies only slightly below the Ku-band up to winds near 8 ms^{-1} and then flattens off to a value that lies 1 to 1.5 % of β below the Ku-band level. The bin-averaged realization of the Ku-band model is built using the cubic equation 16 of Melville et al. (2004) and our field observations of the wind speed and wave height as input. Thus the joint wind and wave height conditions for the two experiments should be equalized somewhat in Fig. 4-8. Therefore, present data suggest that while Ka-band data do fall below the Ku-band results, they do so by less of a factor than previously reported (Walsh et al., 1991) and the frequency

difference is most apparent at the higher wind speeds. We note that the comparison when done in terms of the rms slope and equation 18 of Melville et al. (2004), though not shown, yields results similar to Fig. 4-8.

Figs. 4-9 and 4-10 provide results at Ka-band for β_{ta} and Δ and the subsequent residual EM bias derived using our observations and eqs. 4.4 and 4.5. As in Fig. 4-7 one sees an attenuation of the cross-skewness in Fig. 4-9. Δ is only a weak function of wind speed and varies little from its mean value near 0.4. Note that this term β_{ta} will increase with decreasing radar frequency such that Ku- and C-band sensors would carry increasingly larger tilt bias within their EM bias (Elfouhaily et al., 2000).

The error bars for β_{res} in Fig. 4-10 show significant scatter but the mean results suggest a strong rise with wind speed from near zero at low winds to a maximum value of 2.3 % near a wind speed of 8 m s^{-1} . The value then falls off to a value near 1.5 % as winds become moderate to strong. The relative EM bias contributions of the longer wave tilt bias and this residual are seen in these two figures. At light and strong winds both components are nearly of the same order while for moderate wind speeds the residual component exceeds the tilt term by as much a factor of three. The residual derivation was also carried out versus rms slope and we find similar results where removal of the tilt bias leaves a nonlinear residual behavior versus the abscissa and relative contributions vary versus the rms slope similarly to that with increasing wind.

The agreement between observed β_{res} and the first-order hydrodynamic theory prediction at Ku-band (Elfouhaily et al., 2001a) is quite remarkable. The results are also in qualitative agreement with the hydrodynamic model prediction seen in Fig. 9 of Rodriguez et al. (1992) where the deep phase (i.e. quasi-optical) approximation is suggested to be applicable for comparison to results from a Ka-band system. Both theory and observations suggest a local maximum in wind speed and subsequent fall-off as winds become strong. While this behavior has several possible interpretations, the close agreement with the well known hydrodynamic modulation theory suggests that this observational product β_{res} provides some validation of that approach. Most apparent, however, are the facts that this residual component is not negligible, is associated with wavelengths less than 2 m, and is not linearly related to wind speed or the longer wave slope variance. The last observation points to an observed difference between WNL and residual components.

Most of the discussion and data presentation here is focused upon mean relationships between bias terms and wind and wave statistics. The fetch-limited case of Fig. 4-6 is presented to provide some view of variability within the data. This case where wind speed is nearly constant is provided as evidence that the observed tilt and radar bias observations are: a) not simply related to either the wind speed or the longer wave slope variance, and b) that the standard deviations seen in the error bars of Figs. 4-2- 4-5 are associated at least in part with geophysical variability not encompassed by any univariate relationship. The conditions dictating the range bias for Fig. 4-6 appear to be somewhat complex. One hypothesis is that a turning and likely multi-modal wave spectrum after 80 km in fetch breaks down a large radar EM bias that is associated with strongly directional and growing long wind wave field. The initial rise with fetch coincides with a high elevation skewness, hence strong directionality and likelihood of a steepened sea. The observed large β_{Ka} at short fetch is then associated with some form of short-wave modulation with respect to the wave elevation, whereas the laser-derived tilt bias shows no such extreme behavior. That is, differences between the tilt bias and the radar suggest that no simple WNL theory explanation will suffice here. The decrease in the radar bias and slight increase in the tilt bias from 80-130 km appear to be associated with a change in the overall wave field directionality as suggested by panels d and e in Fig. 4-6. The slight increase in the friction velocity at this fetch may also support the notion of a change in the wave field. One fundamental discussion point for this case is that the radar data do not strongly correlate with wind speed or rms slope. However, both the tilt and radar bias terms do follow the slope variance better than they do the wind speed.

This study does not deal explicitly with EM bias parameterization, nor do the data indicate the clear difference between EM bias correlation with wind speed and with rms slope that has been reported elsewhere (Millet et al., 2003; Melville et al., 2004). In these efforts the same Ku-band tower data are used to show that use of H_s and s improves upon the traditional model formed using H_s and U_{10N} . The present study certainly affirms a linear relationship in s is fairly representative for both β_{ta} and β_{res} , our observed components making up the Ka-band EM bias. Moreover, the overall quadratic nature of the tower Ku-band results of Fig. 4-8 suggests that the β_{res} term derived at Ku-band would yield a result similar to that of Fig. 4-10. The point being that the Ku-band tower results appear to be

reasonably consistent with that shown in the present study in the overall sense of tilt and long-short wave bias contributions.

Regarding implications for improved satellite sea state bias corrections, this study provides some service in dictating which part of the the surface wave description and wave-wave interactions to address. Presented observations strongly support theoretical claims that both WNL and long-short wave interactions contribute to the EM bias. While WNL theory is well-established, theory for short wave dynamics in the EM bias is not due to complexity on numerous levels. The interplay between longer wave hydrodynamics, the local wind, and cm-to-m scale waves remains a difficult process to observe and model in the field. Nevertheless, one now has a better sense of the order of magnitude for each factor to provide guidance, for example, on how one brings WNL modeling to bear in global bias estimation using a wave model (e.g. Gommenginger et al., 2003). Additionally, within-wave data analysis (Chapron et al., 1996) is underway with the present data set in an attempt to isolate short wave roughness variance along the phase of the longer wave and thus gain further insight into the controls and variability for the β_{res} term.

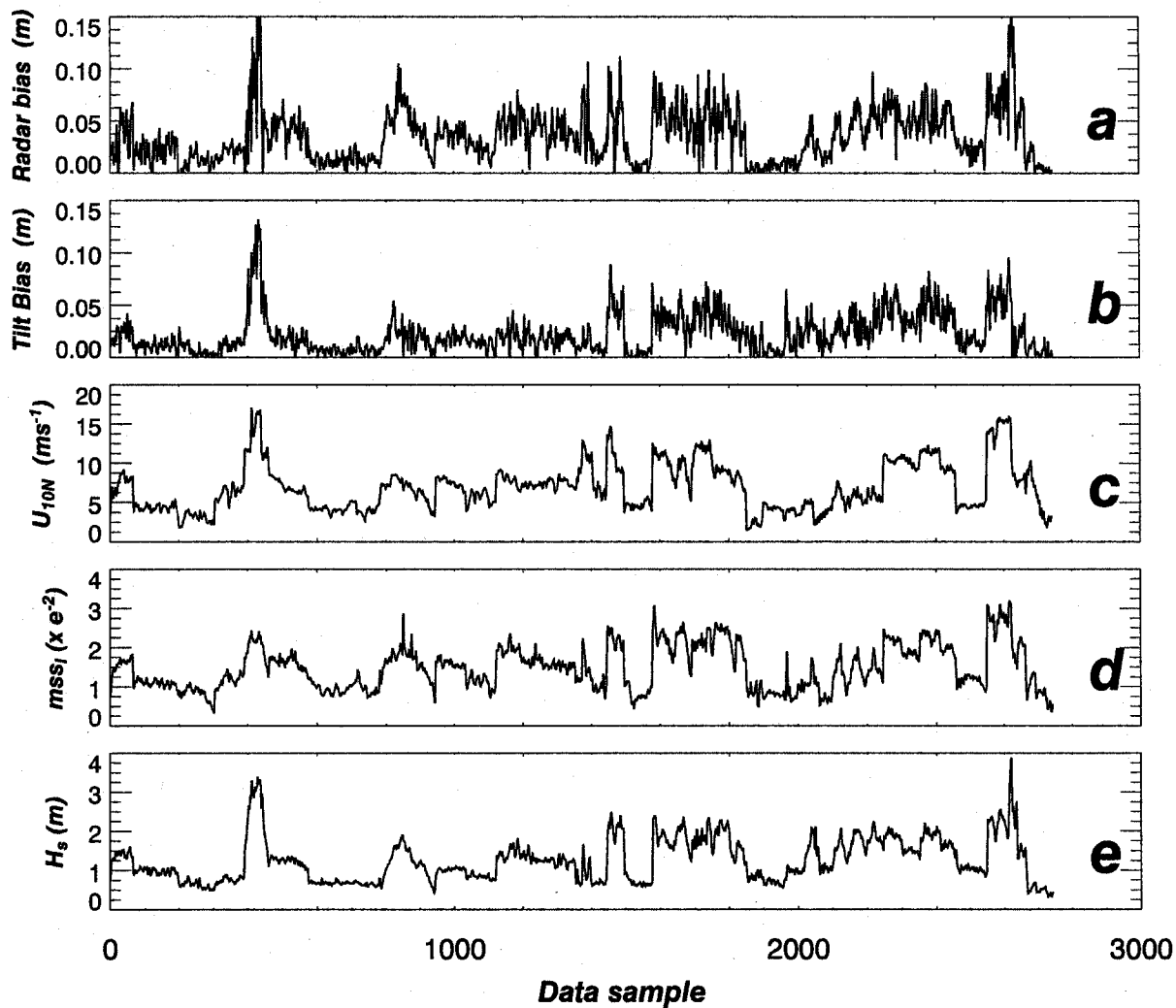


Figure 4-1: All 5 km flight leg averaged data samples for the experiment with (a) the radar-derived range bias, (b) the tilt bias, (c) the neutral stability wind speed, (d) the slope variance for waves greater than 2 m, mss_l , and (e) the significant wave height. A three point boxcar average was applied to each data series.

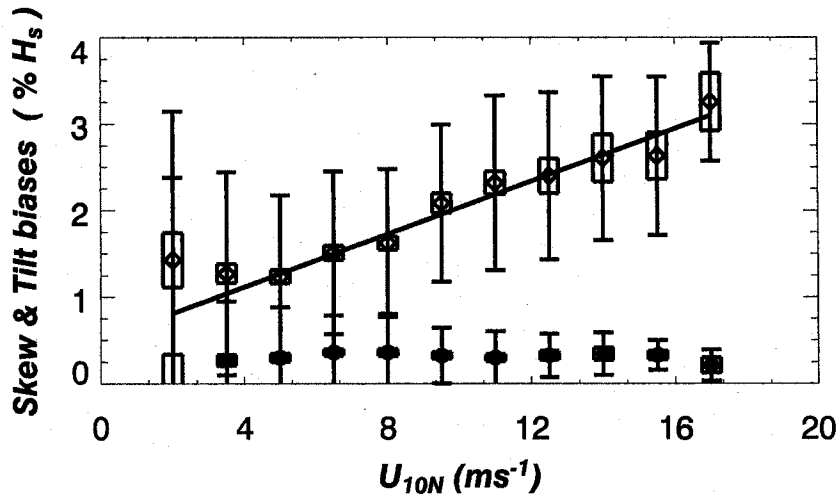


Figure 4-2: Relative bias measurements versus wind speed. The upper values are the observed relative tilt bias (β_t) for the intermediate scale slopes. The lower symbols represent the elevation skewness term (β_s). Points represent averages over $1.5 m s^{-1}$ wind speed bins and the whisker plot provides are 50 % and 95 % confidence intervals. The solid curve represents a linear fit through the tilt bias data for wind speeds above $4 m s^{-1}$.

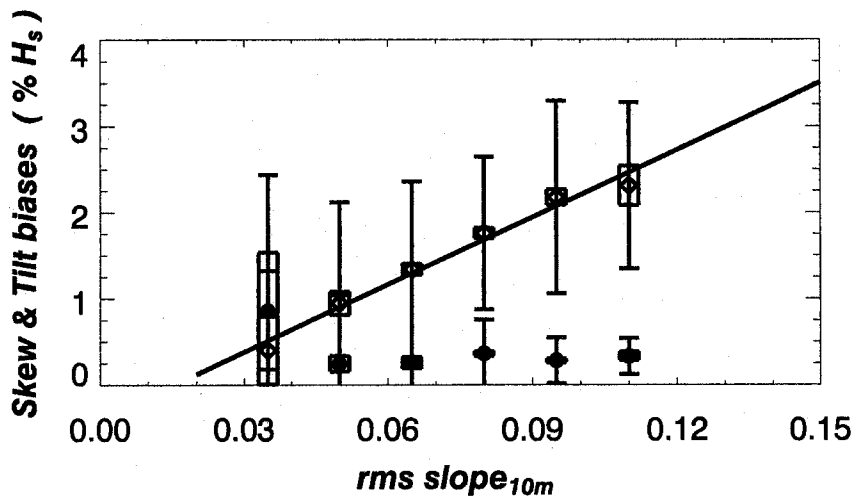


Figure 4-3: Same as Fig. 4-2 excepting the change of abscissa to the rms slope for waves greater than 10 m. The solid curve represents a linear fit through the tilt bias data.

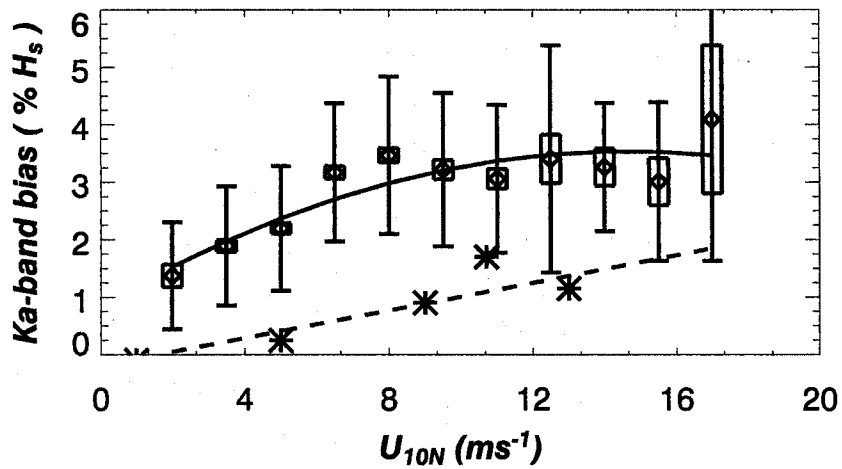


Figure 4-4: Relative radar bias measurements versus wind speed. The symbols are the observed relative electromagnetic bias (β_t) for a Ka-band radar. Points represent averages over 1.5 ms^{-1} wind speed bins and the whisker plot provides are 50 % and 95 % confidence intervals. The solid curve represents a quadratic fit through the data. The lower curve (dashed) represents a linear model obtained from the Ka-band data of Walsh et al. (1991).

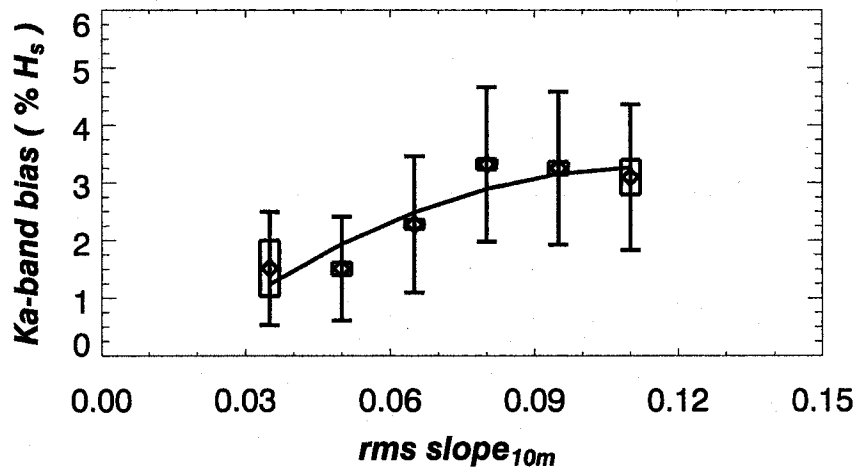


Figure 4-5: Same as Fig. 4-4 excepting the change of abscissa to the rms slope for waves greater than 10 m.

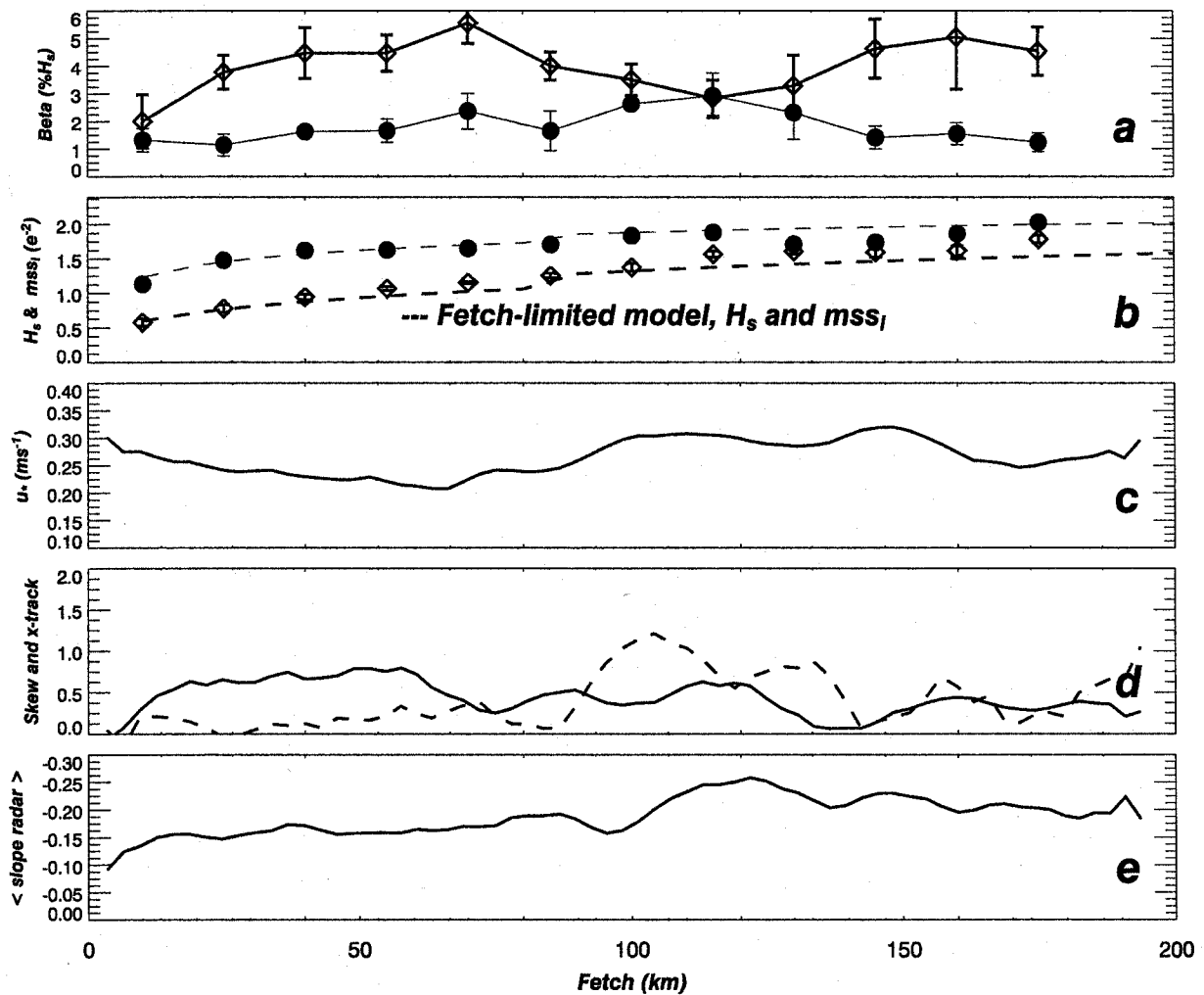


Figure 4-6: Aircraft measurements versus distance from shore on Nov. 15, 1998. (a) the radar- and laser-derived relative range biases, (b) observed wave height and mean square slope as well as fetch-limited predictions as discussed in text, (c) friction velocity, (d) elevation skewness bias (solid) and cross-track slope bias (dashed) as % H_s (e) cross correlation between the slope and radar cross section. In each case a 15 km boxcar average has been applied to the data.

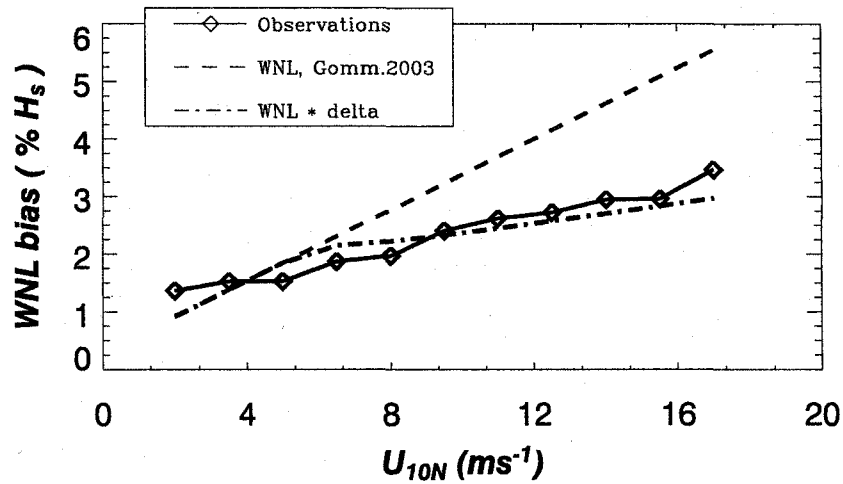


Figure 4-7: Upper curve is the tilt + skewness bias (β_{WNL}) prediction from a two dimensional realization of weakly nonlinear theory where the high frequency cutoff is taken to be $10 k_p$. The bottom trace is WNL theory for a 2 m wavelength cutoff using the factor Δ as discussed in the text. Observations are the bin-averaged result for the skewness and cross-skewness terms of eq. 4.2.

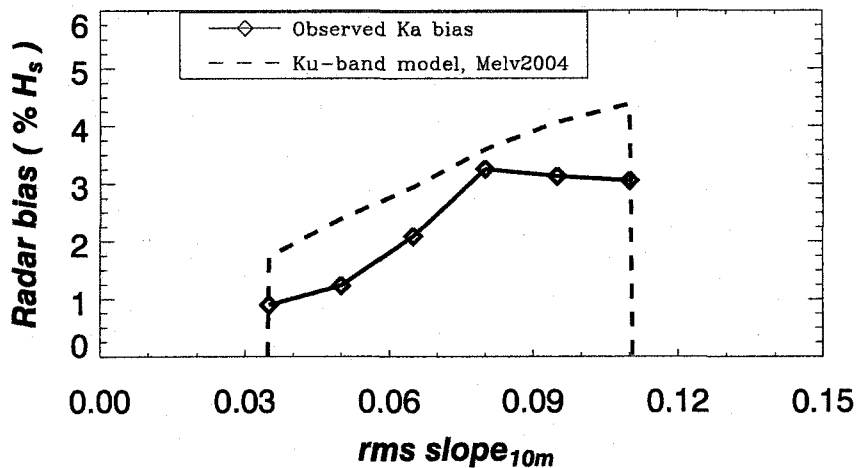


Figure 4-8: Ka-band bias results as seen in Fig. 4-4 and experiment-derived Ku-band model results using eq. 16 of Melville et al. (2004).

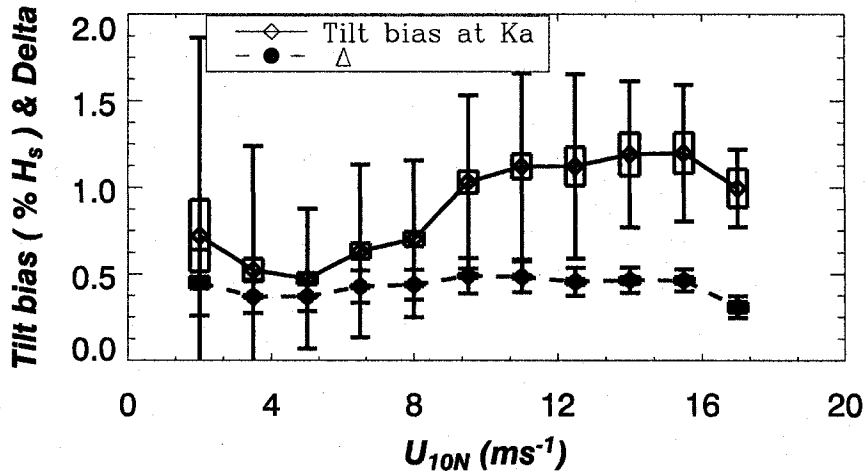


Figure 4-9: The cross-skewness bias expected for a Ka-band altimeter as derived from λ_1 and Δ observation using eq. 4.4. The separation scale for long and short waves in Δ is 2 m and the short wave slope variance is derived using the Ka-band backscatter as discussed in the text. Resulting attenuation can be compared to Fig. 4-2.

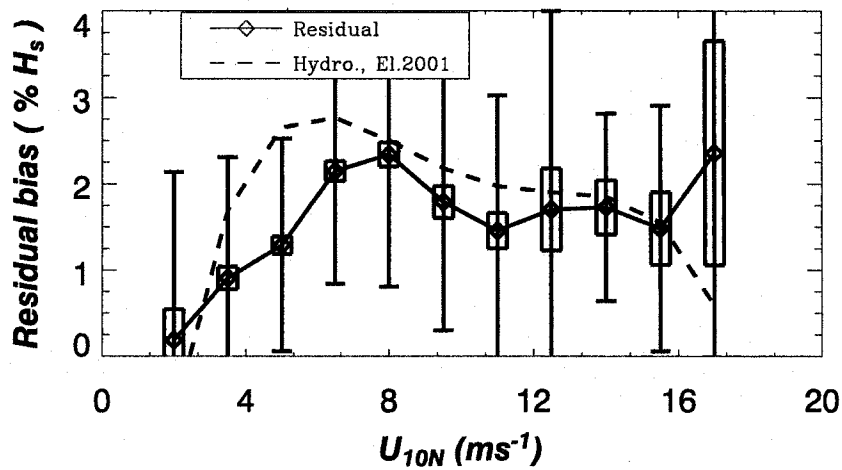


Figure 4-10: The residual EM bias at Ka-band as derived using eq. 4.5 and the laser and radar-derived range biases and slope variance data. Both the 50 and 95 % confidence intervals are shown for the bin-averaged result. The model curve is hydrodynamic theory EM bias for wind and wave aligned conditions at Ku-band band as seen in Elfouhaily et al. (2001a).

Chapter 5

Summary

Satellite altimetry represents one cornerstone in efforts to monitor climate change via ocean surface observations from space. Nearly continuous altimeter operation from the mid-1980s into the foreseeable future is providing records of sea level change, ocean topography dynamics associated with inter-annual events such as El Nino and the North Atlantic Oscillation, ocean circulation and mesoscale eddy observations for assimilation into coupled models, and surface wind and wave measurements with fine spatial resolution. This is being accomplished across a multitude of platforms (Geosat, Geosat follow-on, TOPEX/Poseidon, ERS-1, ERS-2, Envisat, Jason-1, OSTM) all sharing a fairly consistent use of radar altimeter technology at the Ku-band microwave frequency. This study is concerned with optimizing the use of these data. In particular, we focus on the impact that a constantly changing ocean surface gravity wave field plays in controlling radar signals reflected off the sea surface.

Ocean wind wave control of radar reflection has been studied for many years and from many perspectives. The altimeter represents a subset where the incident radiation is directed vertically downward and the electromagnetic scattering can generally be treated as quasi-optical or quasi-specular, e.g. using a ray-tracing approach (Barrick, 1968a). But the complexity that follows as one refines this measurement and its geophysical interpretation extends from the instrumental (sensor specifics such as antenna pointing, transmit and receive power calibration, multiple frequencies, and time series processing) to the physical where the real multi-scale time evolving sea surface is the target. This ocean surface target is the main concern here. The questions we set out to address include: How accurately does an altimeter infer near surface wind speed using reflection off wind waves? When does the swell, or the longer waves not so directly coupled to the wind, affect this reflection?

Can we use the altimeter reflection to gain information on variability in coupling between the surface waves and the wind stress that drives the ocean circulation? Waves are known to systematically alter the precision of a satellite's primary measurement, mean sea level. What improvement can be gained in understanding how this error term is constrained?

The present effort was undertaken to address these questions because of access to an exceptional set of field measurements. Chapter 1 provides detail on the questions above and on the measurements used. The observations were obtained with an aircraft platform combining low-altitude flight in the constant flux layer along with radar backscattering, wave elevation and slope, and wind turbulence measurements. These factors, combined with collection over a range of wind and wave conditions in space and time, provide data that are well suited to provide new insight in the chosen topics.

Chapters 1 and 2 set the stage for the thesis as a whole with respect to how the aircraft measurement geometry and a conceptual model splitting wind waves into two scales are tied together through most of this work (see eq. 1.2). The satellite altimeter has a 1-2 km diameter surface footprint meaning that the radiation impinges on many waves (dominant wave length scale is $\approx(100 \text{ m})$) simultaneously. Riding atop these long waves are wind-roughened shorter waves. These steeper cm-scale waves control radar reflection to first order. These scales are also considered the most tightly correlated with the local wind at the surface, but are also modulated by long wave hydrodynamics. So, inside the satellite footprint there are many realizations of long waves with their attendant short waves, all incoherently averaged to give one reflected signal. The aircraft data here present within-wave measurements made at spacing steps of 1 m in the horizontal as the aircraft proceeds along the flight track. Such fine within-wave resolution allows closer observation of the actual geometry that can only be inferred from space. What is most unique here is that we have both wave slope and wave elevation measurements for this 1 m facet scale coincident with down-looking radar scattering that has a 1 m diameter footprint. The radar thus measures the roughness for wave scales inside of 1 m, but this from a facet whose slope is constantly changing with the longer waves and measured using our laser array. The coincident combination is what turned out to be the most beneficial and new, providing support for several hypotheses that had yet to be fully vetted.

An illustration of this two scale capability can be seen in Chapter 2, Figs. 2-9 and 2-12.

Here we address that the hypotheses that the geometric tilt field is a significant component in the overall backscatter seen by a radar altimeter and that variability in the long wave tilt field will bear directly on any wind speed inversion drawn from the backscatter. The spatial coverage of the aircraft from inland to coastal to open ocean sites was used to provide dynamic range in the long wave tilt field. The result seen in Fig. 2-9 demonstrates the basic influence of the tilt variability on the mean radar cross section measurement for any given wind speed. Results indicate the tilt variance is typically about 40 % of the total radar-derived slope variance. This is reasonably invariant with wind speed and leads to another point. When one removes the slope variance of the longer waves one finds a reasonably clean rendering of short-wave roughness and its relationship as seen in Fig. 2-10. The radar analyses of Chapter 2 were developed assuming a quasi-optical theory for rough surface scattering (eq. 2.5) that is admittedly simplistic, but found to be sufficient to support the conclusions drawn in this study.

Additionally, Chapter 2 introduces gravity wave slope statistic measurements into the literature that are more extensive and precise than for any previous study. Our 1 m laser array was used to generate slope variance, skewness, and kurtosis estimates that are discussed in the context of the oft-cited work of Cox and Munk (1956) where these properties were inferred using a sparse data set collected off Hawaii under oil slick sea surface conditions. Moreover, the radar measurements at Ka-band are also used to clarify an outstanding discrepancy in what the value should be for the 'effective' Fresnel reflection coefficient at Ka-band (Masuko et al., 1986). The Ka-band results presented here are more consistent with other radar measurements and with theoretical and observation-based models for gravity-capillary wave height spectral density at the 0.8 to 2.5 cm wavelengths.

A somewhat unanticipated result in Chapter 2 is the variability of short scale roughness, mss_h , associated with the longer wave field. We found that as the long wave field steepens (as estimated using the slope variance mss_l) the short wave component weakens. This is seen in Fig. 2-11. The short wave slope variance is thus not strictly wind controlled. One hypothesis for the process at work is mechanical blockage of short wave air-sea coupling as seen in past wave tank studies. This issue is certainly second-order and was not pursued further within the scope of the paper, but fits well with time series analysis objectives that will be discussed below.

Chapter 3 represents an effort to incorporate aircraft friction velocity data to address coupling between the atmospheric boundary layer and surface waves. Prior to developing this chapter the overall data set was examined from numerous vantage points to look at variability in the drag coefficient $((u_*/U)^2)$ during the field studies. Several features were observed. First, the drag coefficient for our data set as a whole (Fig. 3-1) fell in line with recent field work in the North Sea (Oost et al., 2002). This model incorporates wave age and as noted in Chapter 1, a research goal here was to identify and quantify any drag variability associated with long and short-wave slope variances. Fig. 5-1 is also derived from our measurements and indicates apparent correlation with several wave parameters, but also with the atmospheric stability (middle panel Richardson's number). This moderate wind speed sampling suggested promise. Particularly interesting is the nearly linear trend observed in the first and last panels where mss_l comes separately from aircraft and buoy measurements. Moreover, one sees nearly flat drag variability for the short-wave slope term (mss_{short}) once these waves are established. Together, these results are suggestive of longer-wave form drag control upon ΔC_d . However, when this composite analysis was broken down to contain only cases with near-neutral stability the sample size and initial promise for this investigation diminished.

Instead, a decision was made to focus on several cases where a substantially depressed drag coefficient was observed under moderate wind speeds. Closer examination led to the determination that these cases were associated with recurring conditions in this region. The conditions generally involve wind flow from the east to the southwest, swell from the east to the south, and fairly stable atmospheric boundary conditions. Data for these specific conditions are used in Chapter 3 to explore the hypothesis that the reduced drag coefficient is due to the presence of swell traveling with the wind direction and its corresponding wind sea.

Similar results have been observed at a site in the Baltic (Smedman et al., 2003b) and that group proposes that one can address the depression in drag via wind-aligned swell. But this should include consideration of the energy ratio between the swell and sea - the more dominant the swell the lower the downward momentum flux. Each of these wave field descriptors are determined in our study using the directional wave spectral data derived from wave buoys in the SHOWEX experiment. Our observational support for the hypothesis

is seen in Fig. 3-3. The work was developed to this case study level with promising results and presented at two conferences and in their respective proceedings (Vandemark et al., 2004b,a). However, further analysis was needed to bring the research to a point where it constitutes a new contribution to the literature. This analysis primarily involves denying the null hypothesis and proof of statistical significance. Can the lowered drag be explained in other terms? In particular, can one eliminate the possibility that the result derives from strong atmospheric stability and/or observational issues related to measurement of the Reynold's stress at one altitude in a non-constant flux profile regime? Is there sufficient sampling of wind-aligned swell events at neutral stability? These questions were addressed by detailed review of the environmental conditions and buoy wave spectra, co- and cross-spectral analyses of the wind velocity components (e.g. $S(uu)$, $C(u'w')$, $C(v'w')$ (Smedman et al., 2003a)) and of wind and wave elevation data ($C(u'\zeta)$, $C(w'\zeta)$ (Rieder and Smith, 1998)), and examination of vertical soundings made by the aircraft up through the marine boundary layer. Primary conclusions drawn are that this data set is simply not large enough in its event sampling, that this region's typical coincidence of stable boundary layers and wind-aligned swell is not well-suited to eliciting these two possible drag controls, and that our near surface boundary layer turbulence sampling scheme limits the ability to shed new light on swell- ABL interactions.

As one aside for Chapter 3, this aircraft data set likely represents the largest field study compilation having both u_* and nadir-view σ^o . In fact, one primary objective at the project's start was to acquire this combination. The motivator is that the desired satellite derivative from any wind sensing satellite, including the altimeter, is usually the near surface wind stress ($\tau = \rho u_*^2$). The analyses within this dissertation did not lead to publication of the observed σ^o to u_* correlation. But for completeness, the measurements are included as Fig. 5-2. To first-order, this result follows that of Fig. 2-6 and this conclusion holds for most of the σ^o versus U_{10n} observations presented in this thesis including those seen in Chapter 4.

Chapter 4 again relies on the two scale nature of our measurements to introduce new observations to the literature. The electromagnetic bias in radar altimetry has been the subject of numerous investigations but the field data sets on the topic are limited to a handful of campaigns. The first field measurements of the cross-skewness sea state bias term, the

cross correlation between wave elevation and slope, are presented. The results are shown to be consistent with weakly nonlinear theory and provide a benchmark for modeling the magnitude and wind dependence of this fundamental geometric control of the range bias. Moreover, these results are combined with the Ka-band EM bias measurements to assess past field observations. But also to address the competing theory that the EM bias is associated with the straining of short cm scales along the profile of the longer wave and that the EM bias could thus exist even if the longer wave field was completely linear. The observations support the hypothesis that both processes are present under most conditions and the study goes on to detail their ratio under various wind and wave conditions. Competing theories remain as to how to conceptually and mathematically describe the long-wave short-wave interactions and this study does not resolve this dilemma. However, the data may well support further clarification through time series analysis of the laser and radar data. This is discussed briefly below.

5.1 Significance and future work

This work is foremost observational in nature and its significance is derived primarily from bringing new field data to bear on topics in satellite altimetry in particular and in air-sea interactions in general. As discussed, the key theme and contribution lies in coincident wave slope, wave elevation, and radar backscatter measurements. These data are used to inform several satellite altimeter modeling and data interpretation efforts.

Firstly, the role of long wave slope variance in the retrieval of a near surface wind speed or wind stress from radar backscatter at nadir-incidence is documented. This result has been anticipated but never before illustrated in the certain terms of Chapter 2. Results should have direct bearing on the improved interpretation of altimeter-derived wind speed data from the numerous past and present platforms. The observations should also serve to improve both theoretical and empirical investigations of ocean microwave scattering and emission from the sea surface (e.g. Liu et al., 1997; Tatarskii, 2003) because one missing constraint has been measured statistics on the wave slope at intermediate scales as presented herein.

The second contribution revolves around new observational evidence for the controls

on the altimeter electromagnetic range error, or sea state bias. This evidence provides sound support and guidance for the use of theory in this important topic where the goal is improved sea level estimates from space. A weakness that has existed in the literature is the lack of quantitative constraint for the competing roles that long wave geometry and long-wave short-wave interactions might play in the total observed range bias. The data of Chapter 4 provide new certainty in this constraint.

One area of immediate interest for future work in this topic is time series analyses of the surface wave elevation and radar data for given ground segments. Work in each chapter identified the average or bulk relationship between such variables as σ^o , wave slope, wave elevation, U_{10N} and the EM bias. These findings represent necessary steps in the topics addressed. But it is proposed that there is significant science still to be gained from the within-wave measurements of elevation, slope and radar backscatter. The most basic derivatives desired are direct determination of the short wave (i.e. backscatter) variability along the long wave phase, and the identification of wave breaking at any scale between 10 and 1000 cm. Obtaining such information would help to better define the model for ocean surface roughness and directly inform questions raised in the dissertation related to the hydrodynamic term in the EM bias and the mechanical blockage of short-wave roughness seen in Chapter 2. Each flight segment holds a spatial sampling at 1 m step over a propagating nonlinear wave field. Initial analyses using Fourier and wavelet transform techniques (Chapron et al., 1996; Vandemark et al., 2001) have suggested that a better tool for nonstationary and nonlinear signals is desired to de-convolve the relevant long wave signals from the raw elevation data series. Such a gravity-wave specific signal decomposition is under development and it is hoped that its application will lead to further significant findings using the data set in hand.

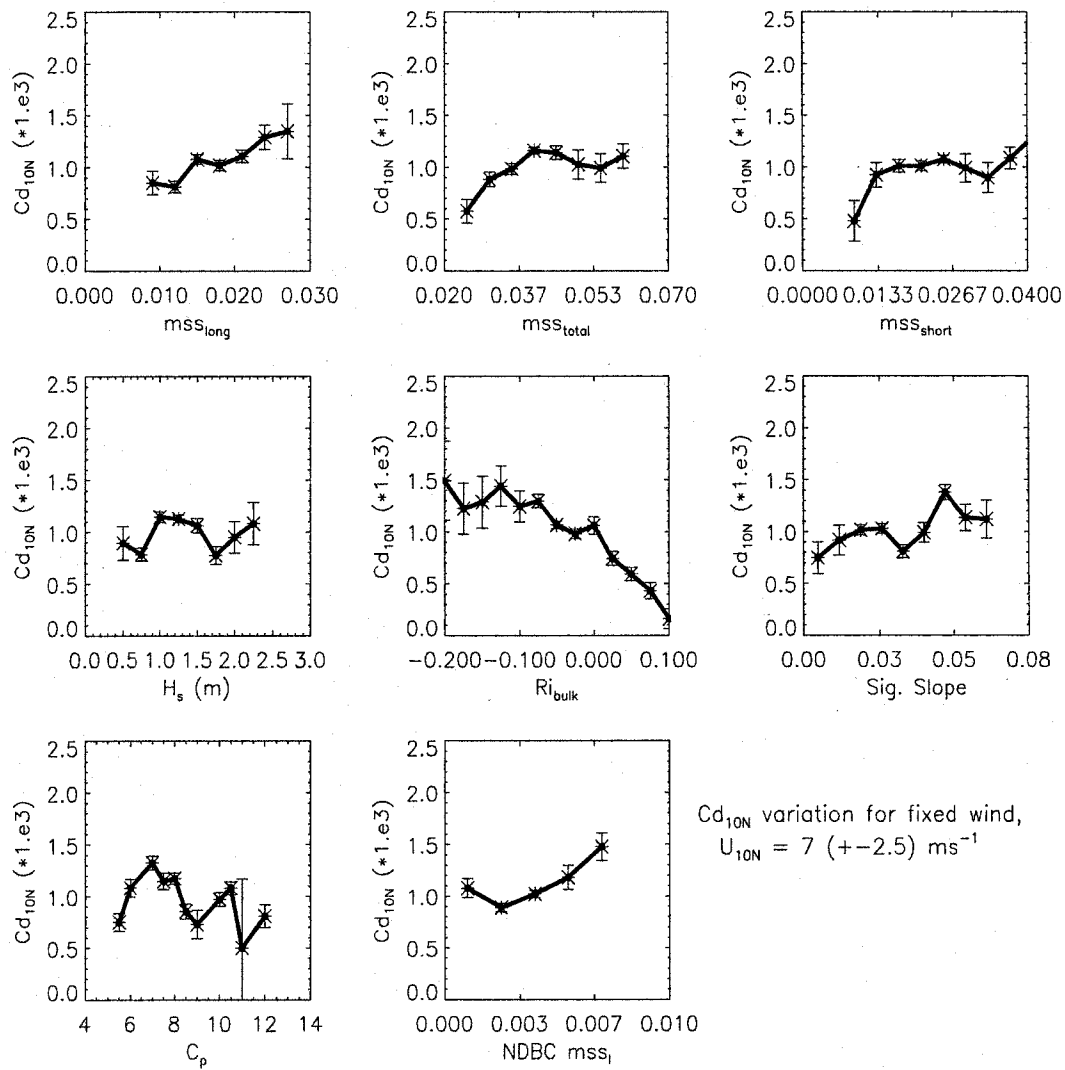


Figure 5-1: Drag coefficient variation for a fixed wind speed of 7 m/s versus the suite of wave measurements available in this study from either the aircraft or wave buoys.

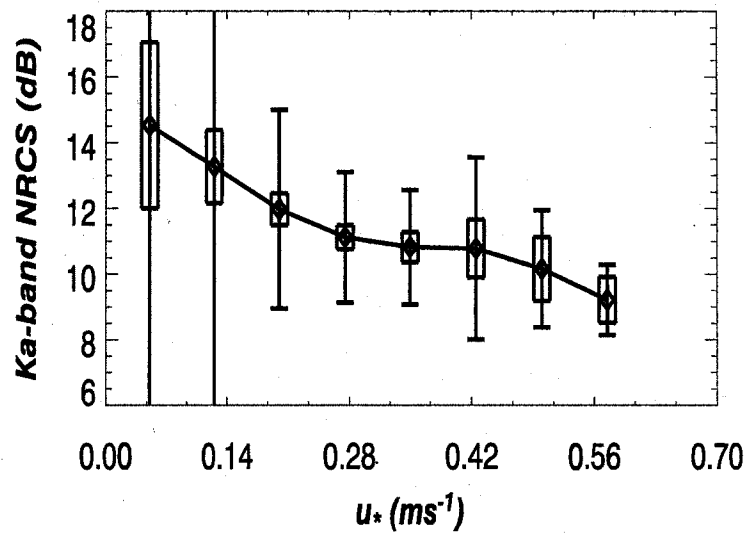


Figure 5-2: Bin-averaged Ka-band σ^o versus friction velocity derived from the overall LongEZ data set. Bars indicate the 50 and 95 % confidence levels without consideration of error in u_* . Results come from 15 km data segments and for the open-ocean sample locations as in Fig. 2-6.

Chapter 6

Appendix

6.1 Copyright permission for Chapter 2

To: Doug Vandemark <douglas.vandemark@nasa.gov>

From: Melissa Weston <mweston@ametsoc.org>

Subject: Re: Permission for author to use...

Dear Mr. Vandemark:

Through this e-mail, the American Meteorological Society grants you permission reprint the following Journal of Physical Oceanography article as requested below. Full acknowledgments to AMS as the copyright holder and bibliographical details of the publication should be cited.

Best regards,
Melissa

At 10:34 AM 1/27/2005 -0500, you wrote:

Melissa,

Per our discussion this is a request to include a copy of the paper - Vandemark et al., J. Phys. Oceanography, 34, 2825-2842,2004, as a chapter in my PhD Dissertation at the

University of New Hampshire to be completed spring 2005. Dissertation is entitled 'On the role of high frequency waves in ocean altimetry'.

Thanks for your help,

Doug

Doug Vandemark

douglas.vandemark@nasa.gov

(603) 862-0195; FAX (603) 862-0243

=====

Melissa Weston, Executive Officer

American Meteorological Society

45 Beacon Street

Boston, Massachusetts 02108-3693

TEL: (617) 227-2426, ext. 250

FAX: (617) 742-8718

=====

6.2 Listing of symbols and acronyms

Table 6.1: List of cited symbols and acronyms

z	distance above the sea surface
λ	wavelength
f	frequency
f_o	frequency of radar transmission
λ_o	wavelength of radar transmission
R^2	seawater surface Fresnel reflectivity coefficient
θ	incidence angle, $\theta_{nadir} = 0^\circ$ for the altimeter
σ^o	normalized radar cross section, nadir incidence angle assumed in text
ϕ	azimuthal angle
u, v, w	E/W, N/S horizontal and vertical wind velocity components
U	near-surface wind speed (ms^{-1})
U_{10N}	wind speed at $z=10$ m, normalized to neutral stratification
u_*	friction velocity = $(\langle u'w' \rangle^2 + \langle -v'w' \rangle^2)^{0.25}$ (ms^{-1})
τ	wind stress = ρu_*^2
C_{DN}	turbulent boundary layer drag coefficient, normalized to neutral stratification
R_i	Richardson's number for atmospheric stability, buoyancy:shear
SST	sea surface temperature
η or ζ	surface wave elevation
η_x or s_x	surface slope along x axis
H_s	significant wave height
c	deep water gravity wave phase speed, or celerity (ms^{-1})
c_p	surface wave phase speed at the spectral energy peak wavenumber
k	wavenumber ($radm^{-1}$)
k_p	surface wavenumber at the spectral energy peak wavenumber
Ω	inverse wave age = $(U \text{ OR } u^*)/c_p$
mss	mean square slope
mss_l	long wave mean square slope, $\lambda > 2m$
mss_h	short wave (or high wavenumber) mean square slope, $1 - 3cm < \lambda < 2m$
GPS	global positioning system
BAT	best atmospheric turbulence probe

Bibliography

- Anderson, C., Macklin, T., Gommenginger, C., and Srokosz, M. (2002). Towards a unified theoretical model of ocean backscatter for wind speed retrieval from SAR, scatterometer, and altimeter. *Can. J. Remote Sens.*, 28(3):354–366.
- Apel, J. R. (1994). An improved model of the ocean surface-wave vector spectrum and its effects on radar backscatter. *Journal of Geophysical Research-Oceans*, 99(C8):16269–16291.
- Arnold, D. V., Melville, W. K., Stewart, R. H., Kong, J. A., Keller, W. C., and Lamarre, E. (1995). Measurements of electromagnetic bias at Ku-bands and C-bands. *J. Geophys. Res.-Oceans*, 100(C1):969–980.
- Banner, M. L. (1990). Equilibrium spectra of wind-waves. *Journal of Physical Oceanography*, 20(7):966–984.
- Banner, M. L., Jones, I. S. F., and Trinder, J. C. (1989). Wavenumber spectra of short gravity-waves. *Journal of Fluid Mechanics*, 198:321–344.
- Barrick, D. (1968a). Rough surface scattering based on the specular point theory. *IEEE Trans. Antennas Propagation*, AP 16:449–454.
- Barrick, D. (1974). Wind dependence of quasi-specular microwave sea scatter. *IEEE Trans. Antennas Propagation*, AP 22:135–136.
- Barrick, J. (1968b). A new model for sea clutter. *IEEE Trans. Antennas Propagation*, AP 16:217–223.
- Bass, F., Fuks, M., Kalmykov, A., Ostrovsky, I., and Rosenberg, A. (1968). Very high frequency radiowave scattering by a disturbed sea surface, 2. scattering from an actual sea surface. *IEEE Trans. Antennas Propagation*, AP 16:560–568.

- Chapron, B., Kerbaol, V., Vandemark, D., and Elfouhaily, T. (2000). Importance of peakedness in sea surface slope measurements and applications. *J. Geophys. Res.-Oceans*, 105(C7):17195-17202.
- Chapron, B., Liu, A. K., Peng, C. Y., and Mollo-Christensen, E. (1996). Higher order spectral and scale analysis of surface wave height fluctuations. *Global Atmos. Ocean Syst.*, 3:151-173.
- Chapron, B., Vandemark, D., Elfouhaily, T., Thompson, D. R., Gaspar, P., and LaBroue, S. (2001). Altimeter sea state bias: A new look at global range error estimates. *Geophys. Res. Lett.*, 28(20):3947-3950.
- Chelton, D. B., Ries, J., Haines, B., Fu, L.-L., and Callahan, P. (2001). Satellite altimetry. In Fu, L.-L. and Cazenave, A., editors, *Satellite altimetry and earth sciences - a handbook of techniques and applications*, pages 1-132. Academic Press, San Diego.
- Chen, W., Banner, M. L., Walsh, E. J., Jensen, J. B., and Lee, S. H. (2001). The southern ocean waves experiment. part ii: Sea surface response to wind speed and wind stress variations. *Journal of Physical Oceanography*, 31(1):174-198.
- Chu, J. S., Long, S. R., and Phillips, O. M. (1992). Measurements of the interaction of wave groups with shorter wind-generated waves. *Journal of Fluid Mechanics*, 245:191-210.
- Cox, C. and Munk, W. (1956). Slopes of the sea surface deduced from photographs of sun glitter. *Bulletin of the Scripps Institution of Oceanography*, 6(9):401-488.
- Crescenti, G., Crawford, T., and Dumas, E. J. (1999). Data report: LongEZ (N3R) participation in the 1999 shoaling waves experiment (SHOWEX) pilot study. Data report OAR ARL-232, NOAA, Air Resources Lab.
- Donelan, M. A. (1974). Generalized profiles of wind speed, temperature and humidity. In *17th conference on Great Lakes Research*, pages 369-388. International Assoc. of Great Lakes Research.
- Donelan, M. A. (1987). The effect of swell on the growth of wind waves. *APL Tech. Dig.*, 8:18-23.

- Donelan, M. A. (1990). Air-sea interaction. In Le Mehaute, B. and Hanes, D. M., editors, *The sea - ocean engineering science*, volume 9A of *The sea, ideas and observations on progress in the study of the sea*, pages 239–292. John Wiley and Sons, Inc., New York.
- Drennan, W. M., Graber, H. C., and Donelan, M. A. (1999). Evidence for the effects of swell and unsteady winds on marine wind stress. *J. Phys. Oceanogr.*, 29(8):1853–1864.
- Dyer, A. (1974). A review of flux-profile relationships. *Boundary Layer Meteorology*, 7:363–372.
- Elfouhaily, T., Chapron, B., Katsaros, K., and Vandemark, D. (1997). A unified directional spectrum for long and short wind-driven waves. *J. Geophys. Res.-Oceans*, 102(C7):15781–15796.
- Elfouhaily, T., Thompson, D. R., Chapron, B., and Vandemark, D. (2000). Improved electromagnetic bias theory. *J. Geophys. Res.-Oceans*, 105(C1):1299–1310.
- Elfouhaily, T., Thompson, D. R., Chapron, B., and Vandemark, D. (2001a). Improved electromagnetic bias theory: Inclusion of hydrodynamic modulations. *J. Geophys. Res.-Oceans*, 106(C3):4655–4664.
- Elfouhaily, T., Thompson, D. R., Freund, D. E., Vandemark, D., and Chapron, B. (2001b). A new bistatic model for electromagnetic scattering from perfectly conducting random surfaces: Numerical evaluation and comparison with spm. *Waves Random Media*, 11(1):33–43.
- Elfouhaily, T., Vandemark, D., Gourrion, J., and Capron, B. (1998). Estimation of wind stress using dual-frequency TOPEX data. *J. Geophys. Res.-Oceans*, 103(C11):25101–25108.
- Fairall, C. W., Bradley, E. F., Rogers, D. P., Edson, J. B., and Young, G. S. (1996). Bulk parameterization of air-sea fluxes for Tropical Ocean Global Atmosphere Coupled Ocean Atmosphere Response Experiment. *Journal of Geophysical Research-Oceans*, 101(C2):3747–3764.
- French, J., Crescenti, G., Crawford, T., and Dumas, E. J. (2000). LongEZ (N3R) participation in the 1999 shoaling waves experiment (SHOWEX). Data report OAR ARL-20, NOAA, Air Resources Lab.

- Fu, L.-L. and Cazenave, A., editors (2001). *Satellite altimetry and earth sciences - a handbook of techniques and applications*, volume 69 of *International geophysics series*. Academic Press, San Diego.
- Glazman, R., Fabrikant, A., and Srokosz, M. A. (1996). Numerical analysis of the sea state bias for satellite altimetry. *Journal of Geophysical Research*, 101(C2):3789–3799.
- Glazman, R. E. and Greysukh, A. (1993). Satellite altimeter measurements of surface wind. *J. Geophys. Res.-Oceans*, 98(C2):2475–2483.
- Gommenginger, C. P., Srokosz, M. A., Challenor, P. G., and Cotton, P. D. (2002). Development and validation of altimeter wind speed algorithms using an extended collocated buoy/Topex dataset. *IEEE Transactions on Geoscience and Remote Sensing*, 40(2):251–260.
- Gommenginger, C. P., Srokosz, M. A., Wolf, J., and Janssen, P. (2003). An investigation of altimeter sea state bias theories. *J. Geophys. Res.-Oceans*, 108(C1):art. no.–3011.
- Gotwols, B. L. and Thompson, D. R. (1994). Ocean microwave backscatter distributions. *Journal of Geophysical Research-Oceans*, 99:9741–9750.
- Gourrion, J., Vandemark, D., Bailey, S., and Chapron, B. (2002a). Investigation of C-band altimeter cross section dependence on wind speed and sea state. *Can. J. Remote Sens.*, 28(3):484–489.
- Gourrion, J., Vandemark, D., Bailey, S., Chapron, B., Gommenginger, G. P., Challenor, P. G., and Srokosz, M. A. (2002b). A two-parameter wind speed algorithm for Ku-band altimeters. *J. Atmos. Ocean. Technol.*, 19(12):2030–2048.
- Graber, H. C., Terray, E. A., Donelan, M. A., Drennan, W. M., and Van Leer, J. C. (2000). Asis - a new air-sea interaction spar buoy: Design and performance at sea. *Journal of Atmospheric and Oceanic Technology*, 17(5):708–720.
- Hall, E., Vandemark, D., Long, S., and Tran, N. (2000). Laboratory tests of Riegler infrared laser distance sensors: Range stability and water reflection characteristics. Data report, NASA Wallops Flight Facility.

- Hara, T., Bock, E. J., Edson, J. B., and McGillis, W. R. (1998). Observation of short wind waves in coastal waters. *J. Phys. Oceanogr.*, 28(7):1425–1438.
- Hesany, V., Plant, W. J., and Keller, W. C. (2000). The normalized radar cross section of the sea at 10 degrees incidence. *IEEE Transactions on Geoscience and Remote Sensing*, 38(1):64–72.
- Hevizi, L. G., Walsh, E. J., McIntosh, R. E., Vandemark, D., Hines, D. E., Swift, R. N., and Scott, J. F. (1993). Electromagnetic bias in sea-surface range measurements at frequencies of the Topex/Poseidon satellite. *IEEE Trans. Geosci. Remote Sensing*, 31(2):376–388.
- Hwang, P. A., Atakturk, S., Sletten, M. A., and Trizna, D. B. (1996). A study of the wavenumber spectra of short water waves in the ocean. *J. Phys. Oceanogr.*, 26(7):1266–1285.
- Hwang, P. A. and Shemdin, O. H. (1988). The dependence of sea-surface slope on atmospheric stability and swell conditions. *Journal of Geophysical Research-Oceans*, 93(C11):13903–13912.
- Hwang, P. A., Teague, W. J., Jacobs, G. A., and Wang, D. W. (1998). A statistical comparison of wind speed, wave height, and wave period derived from satellite altimeters and ocean buoys in the Gulf of Mexico region. *J. Geophys. Res.-Oceans*, 103(C5):10451–10468.
- Hwang, P. A., Wang, D. W., Teague, W. J., Jacobs, G. A., Wesson, J., Burrage, D., and Miller, J. (2002). Anatomy of the ocean surface roughness. Formal NRL/FR/7330-02-10036, Naval Research Laboratory.
- Jackson, F. (1979). The reflection of impulses from a nonlinear random sea. *Journal of Geophysical Research*, 84:4939–4943.
- Jackson, F. C., Walton, W. T., Hines, D. E., Walter, B. A., and Peng, C. Y. (1992). Sea-surface mean-square slope from Ku-band backscatter data. *J. Geophys. Res.-Oceans*, 97(C7):11411–11427.
- Kudryavtsev, V. N. and Makin, V. K. (2004). Impact of swell on the marine atmospheric boundary layer. *Journal of Physical Oceanography*, 34(4):934–949.

- Kudryavtsev, V. N., Makin, V. K., and Chapron, B. (1999). Coupled sea surface-atmosphere model - 2. spectrum of short wind waves. *J. Geophys. Res.-Oceans*, 104(C4):7625–7639.
- Kumar, R., Stammer, D., Melville, W. K., and Janssen, P. (2003). Electromagnetic bias estimates based on topex, buoy and wave model data. *J. Geophys. Res.-Oceans*, 108(C11):art no.-3351.
- Larsen, X. G., Makin, V., and Smedman, A. S. (2004). Impact of waves on the sea drag: measurements in the baltic sea and a model interpretation. *The Global Atmosphere and Ocean System*, 9(3):97–120.
- Liu, Y., Yan, X. H., Liu, W. T., and Hwang, P. A. (1997). The probability density function of ocean surface slopes and its effects on radar backscatter. *J. Phys. Oceanogr.*, 27(5):782–797.
- Longuet-Higgins, M. S. (1963). The effect of non-linearities on statistical distributions in the theory of sea waves. *J. Fluid Mech.*, 17(3):459–480.
- Longuet-Higgins, M. S. (1982). On the skewness of sea-surface slopes. *J. Phys. Oceanogr.*, 12(11):1283–1291.
- Longuet-Higgins, M. S. and Stewart, R. (1960). Changes in the form of short gravity waves on long waves in tidal currents. *J. Fluid Mech.*, 8:565–583.
- Mahrt, L., Vickers, D., Sun, J. L., Crawford, T. L., Crescenti, G., and Frederickson, P. (2001). Surface stress in offshore flow and quasi-frictional decoupling. *J. Geophys. Res.-Atmos.*, 106(D18):20629–20639.
- Marchand, R. T. and Brown, G. S. (1998). Inferring rough surface parameters from average scattering data using approximate scattering models 2. Pierson-Moskowitz spectrum. *Radio Sci.*, 33(4):835–843.
- Masuko, H., Okamoto, K. I., Shimada, M., and Niwa, S. (1986). Measurement of microwave backscattering signatures of the ocean surface using X-band and Ka-band airborne scatterometers. *J. Geophys. Res.-Oceans*, 91(C11):3065–3083.
- Melville, W. K., Felizardo, F. C., and Matusov, P. (2004). Wave slope and wave age effects in measurements of electromagnetic bias. *J. Geophys. Res.-Oceans*, 109(C07):art no.-018.

- Melville, W. K. and Matusov, P. (2002). Distribution of breaking waves at the ocean surface. *Nature*, 417(6884):58–63.
- Melville, W. K., Stewart, R. H., Keller, W. C., Kong, J. A., Arnold, D. V., Jessup, A. T., Loewen, M. R., and Slinn, A. M. (1991). Measurements of electromagnetic bias in radar altimetry. *J. Geophys. Res.-Oceans*, 96(C3):4915–4924.
- Millet, F. W., Arnold, D. V., Warnick, K. F., and Smith, J. (2003). Electromagnetic bias estimation using in situ and satellite data: 1. rms wave slope. *J. Geophys. Res.-Oceans*, 108(C2):art. no.–3040.
- Oost, W. A., Komen, G. J., Jacobs, C. M. J., and Van Oort, C. (2002). New evidence for a relation between wind stress and wave age from measurements during asgamage. *Boundary-Layer Meteorology*, 103(3):409–438.
- Paulson, C. A. (1970). The mathematical representation of wind speed and temperature profiles in the unstable atmospheric surface layer. *Journal of Applied Meteorology*, 9:857–861.
- Phillips, O. M. (1977). *The dynamics of the upper ocean*. Cambridge monographs on mechanics and applied mathematics. Cambridge University Press, Cambridge, 2nd edition.
- Plant, W. J. (2002). A stochastic, multiscale model of microwave backscatter from the ocean. *J. Geophys. Res.-Oceans*, 107(C9):art. no.–3120.
- Rieder, K. F. and Smith, J. A. (1998). Removing wave effects from the wind stress vector. *J. Geophys. Res.-Oceans*, 103(C1):1363–1374.
- Rodriguez, E., Kim, Y. J., and Martin, J. M. (1992). The effect of small-wave modulation on the electromagnetic bias. *J. Geophys. Res.-Oceans*, 97(C2):2379–2389.
- Rutgersson, A., Smedman, A. S., and Hogstrom, U. (2001). Use of conventional stability parameters during swell. *Journal of Geophysical Research-Oceans*, 106(C11):27117–27134.
- Shaw, J. A. and Churnside, J. H. (1997). Scanning-laser glint measurements of sea-surface slope statistics. *Applied Optics*, 36(18):4202–4213.

- Smedman, A. S., Hogstrom, U., Bergstrom, H., Rutgersson, A., Kahma, K. K., and Pettersson, H. (2003a). A case study of air-sea interaction during swell conditions. *Journal of Geophysical Research-Oceans*, 104(C11):25833–25851.
- Smedman, A. S., Larsen, X. G., Hogstrom, U., Kahma, K. K., and Pettersson, H. (2003b). Effect of sea state on the momentum exchange over the sea during neutral conditions. *Journal of Geophysical Research-Oceans*, 108(C11):art. no 3367.
- Srokosz, M. A. (1986). On the joint distribution of surface elevation and slopes for a nonlinear random sea, with an application to radar altimetry. *J. Geophys. Res.-Oceans*, 91(C1):995–1006.
- Stogryn, A. (1997). Equations for the permittivity of sea water. Technical report, Gencorp Aerojet.
- Sun, J. L., Burns, S. P., Vandemark, D., Donelan, M. A., Mahrt, L., Crescenti, G., French, J., and Herbers, T. (2003). Measurement of directional wave spectra using aircraft laser altimeters. *J. Atmos. Ocean. Technol.*, page submitted.
- Sun, J. L., Vandemark, D., Mahrt, L., Vickers, D., Crawford, T., and Vogel, C. (2001). Momentum transfer over the coastal zone. *J. Geophys. Res.-Atmos.*, 106(D12):12437–12448.
- Sverdup, H. and Munk, W. (1947). Wind, sea, and swell: Theory of relations for forecasting. Technical Report 1, U.S. Hydrographic Office.
- Tatarskii, V. I. (2003). Multi-gaussian representation for the cox-munk distribution of slopes for wind-driven waves. *Journal of Atmospheric and Oceanic Technology*, 20(11):1697–1705.
- Valenzuela, G. R. (1978). Theories for the interaction of electromagnetic and oceanic waves: A review. *Boundary Layer Meteorology*, 13:61–85.
- Vandemark, D., Crawford, T., Dobosy, R., Elfouhaily, T., and Chapron, B. (1999). Sea surface slope statistics from a low-altitude aircraft. In *International Geoscience and Remote Sensing Symposium*, volume 2, pages 381–383, Hamburg. IEEE.

- Vandemark, D., Drennan, W. M., Sun, J., French, J. R., and C., G. H. (2004a). Examining wind stress and wind waves in the presence of swell. In *International Geoscience and Remote Sensing Symposium*, volume 2, pages 853–856, Anchorage. IEEE.
- Vandemark, D., Drennan, W. M., Sun, J., French, J. R., and C., G. H. (2004b). Wind stress and wind wave observations in the presence of swell. In *16th Symposium on Boundary Layers and Turbulence*, Portland. Amer. Met. Soc.
- Vandemark, D., Edson, J. B., and Chapron, B. (1997). Altimeter estimation of sea surface wind stress for light to moderate winds. *J. Atmos. Ocean. Technol.*, 14(3):716–722.
- Vandemark, D., Mourad, P. D., Bailey, S. A., Crawford, T. L., Vogel, C. A., Sun, J., and Chapron, B. (2001). Measured changes in ocean surface roughness due to atmospheric boundary layer rolls. *J. Geophys. Res.-Oceans*, 106(C3):4639–4654.
- Vandemark, D., Sun, J., Crescenti, G. H., Chapron, B., and C., G. H. (2004c). Ocean wave slope observations using radar backscatter and laser altimeters. *J. Phys. Ocean.*, 34:2825–2842.
- Vickers, D., Mahrt, L., Sun, J. L., and Crawford, T. (2001). Structure of offshore flow. *Mon. Weather Rev.*, 129(5):1251–1258.
- Walsh, E. J., Hancock, D. W., Hines, D. E., and Kenney, J. E. (1984). Electromagnetic bias of 36-GHz radar altimeter measurements of MSL. *Marine Geodesy*, 8(1-4):265–296.
- Walsh, E. J., Jackson, F. C., Hines, D. E., Piazza, C., Hevizi, L. G., McGlaughlin, D. J., McIntosh, R. E., Swift, R. N., Scott, J. F., Yungel, J. K., and Frederick, E. B. (1991). Frequency dependence of electromagnetic bias in radar altimeter sea surface range measurements. *J. Geophys. Res.-Oceans*, 96(C11):20571–20583.
- Walsh, E. J., Vandemark, D. C., Friehe, C. A., Burns, S. P., Khelif, D., Swift, R. N., and Scott, J. F. (1998). Measuring sea surface mean square slope with a 36-GHz scanning radar altimeter. *J. Geophys. Res.-Oceans*, 103(C6):12587–12601.
- Witter, D. L. and Chelton, D. B. (1991). A Geosat altimeter wind-speed algorithm and a method for altimeter wind-speed algorithm development. *J. Geophys. Res.-Oceans*, 96(C5):8853–8860.

Yaplee, B., Shapiro, A., Hammond, D., and Uliana, E. (1971). Nanosecond radar observations of the ocean surface from a stable platform. *IEEE Transactions on Geoscience and Engineering*, 9:170-174.